Nanoporous Polymers for Membrane Applications

Li, Li

Publication date:
2012

Document Version
Publisher's PDF, also known as Version of record

Nanoporous Polymers for Membrane Applications

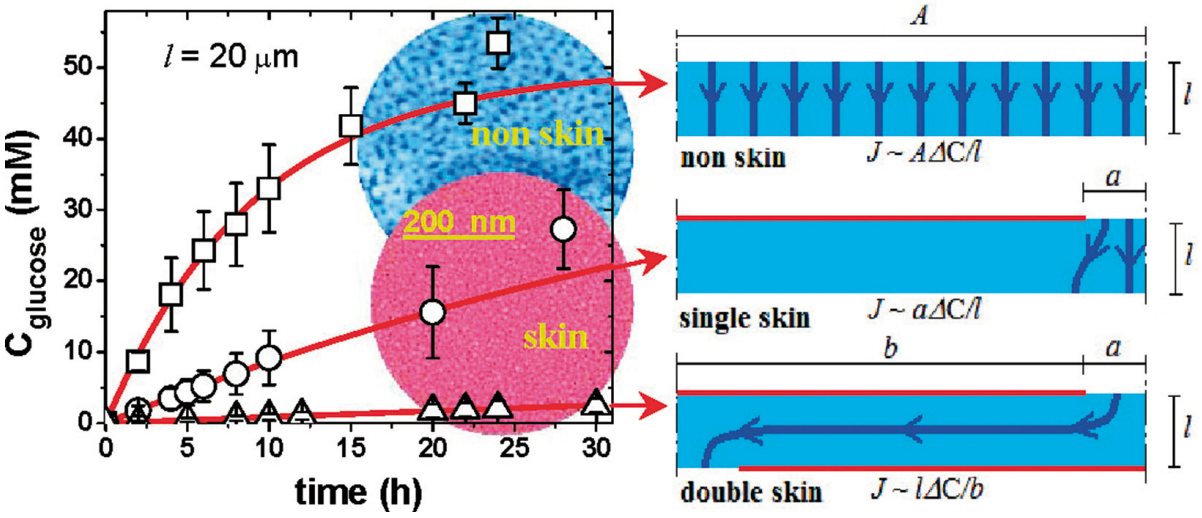

Li Li
Ph.D. Thesis
January 2012

DTU Chemical Engineering
Department of Chemical and Biochemical Engineering

Nanoporous Polymers for Membrane Applications

Li Li

Ph.D. Thesis

Jan 2012

DTU Chemical Engineering
Department of Chemical and Biochemical Engineering

Address: The Danish Polymer Centre
Department of Chemical and Biochemical Engineering
Technical University of Denmark
Sølvtofts Plads
DK-2800 Kgs. Lyngby
Denmark
Phone: +45 4525 2800
Web: www.dpc.kt.dtu.dk

Print: J&R Frydenberg A/S
København
January 2012

ISBN: 978-87-92481-61-0

Acknowledgements

This thesis is the result of my Ph.D. project carried out at the Danish Polymer Center (DPC) in Department of Chemical and Biochemical Engineering at the Technical University of Denmark (DTU) from 2009 to 2011. The overall project was co-financed by DTU, Radiometer Medical ApS, and Danish government. The work conducted at Radiometer Medical ApS in 2008 is not included in this thesis due to confidential agreement.

First, I thank to my supervisors, Senior Scientist Sokol Ndoni, Associate Professor Gunnar E. Jonsson and Professor Martin E. Vigild from DTU, along with Lydia D. Clausen and Kristian M. Hansen from Radiometer Medical Aps. I thank Martin for giving me an opportunity to work on this interesting project. I thank Gunnar for taking over the position as my main supervisor from 2009 to 2011. Thank for your guidance and suggestions to my research. I thank Lydia and Kristian for your great help and support on my study. Most importantly, I appreciate Sokol for your endless patience and massive encouragement and help to me all the way. Thanks for your guidance and suggestions to my work, your availability for discussing results and answering my questions, and your help with manuscripts preparation.

I thank Lars Schulte who synthesized all the polymers used to fabricate the membranes in this thesis work. Lars also gave me help in SEM measurements. I thank Thomas W. Hansen for TEM measurements at the Center for Electron Nanoscopy (CEN) at DTU, Lene Hubert for XPS measurements at Risø, Lotte Nielsen for SEC measurements at Risø and the KT-workshop at DTU for building up the stainless steel filtration cell and the pneumatic-drive compressing set-up. I thank Liang Yang from Department of Systems Biology at DTU for a happy collaboration in anti-biofilm research at the end of my Ph.D. project.

I thank Piotr P. Szewczykowski, Fengxiao Guo, Kaushal S. Sagar, Anton Berthold and other former and current members of the Nanoporous Group for your helpful discussions and advices in the project and bringing me a lot of fun in group social activities. I particularly thank to Kaushal and Anton for your encouragement as things did not always go in the direction as expected.

I also thank DPC which provides me a nice lab platform. Thanks to Professor Ole Hassager for accepting me at DPC as a master student 5 years ago. Thanks to Associate Professor for your concern and help in my study and daily life. Thanks to the lab coordinator Kim C. Szabo for your help in lab work. Thanks to the administrative coordinator Vibeke H. Christiansen for your help in daily work. Thanks to my officemate Yanwei Wang for inspiring discussions and useful suggestions. Thanks to other colleagues at DPC for many good experiences in the past 3 years, like cake club, pizza seminar, beer club, Christmas lunch, summer dinner, and annual polymer day. Anca, I will miss your lovely smile and constant enthusiasm. Mads and Sarah Maria, I enjoyed a lot talking with you.

I sincerely thank my family and friends who gave me your hands whenever I needed. Without your assistance, it would not be possible for me to achieve what I have today.

Lastly, I would like to thank everybody who has ever impressed, inspired, taught, influenced and helped me along the way. I feel sorry that I could not mention all the names within the limit space, but I will remember you in my life.

Kgs. Lyngby, 23th April 2011
Li Li

Abstract

Membrane technology has been realized as a useful tool in a variety of applications, such as health sector, food industry, sustainable water treatment and energy conversion and storage. However, the widespread use of this technology has been impeded by many issues including cost, performance, durability and etc. These limitations can be directly related to the membrane used. In particular, advances in the design and fabrication of nanoporous materials are expected to open up new opportunities for the development of membrane technology. Nanoporous polymer membranes derived from self-assembling block copolymers are the focus of the thesis work.

Block copolymers consist of macromolecules composed of two or more chemically different blocks. Block copolymers can self-organize into different morphologies with characteristic sizes in the nanometer scale. Self-assembled block copolymer is evolving as a powerful yet affordable tool to fabricate nanoporous materials with well defined morphology, pore size and distribution, porosity, and surface chemistry. This type of nanoporous materials is therefore attractive for the regulation and detection of transport at the molecular level. We have used 1,2-polybutadiene-*b*-polydimethylsiloxane (1,2-PB-*b*-PDMS) block copolymer for the production of nanoporous membranes.

Nanoporous 1,2-PB membrane with bulk gyroid morphology was obtained via selective and quantitative removal of PDMS block in 1,2-PB-*b*-PDMS. The gyroid structure shows isotropic percolation without the need for structure pre-alignment. The structure of the membrane outer surface can be controlled from being closed (compact) to open (porous) by adjusting the interface energy between polymer and different substrates used in membrane formation process. Surface chemistry of nanopores can be changed using photochemistry for a specific need. The work presented in this thesis focuses on exploration of three relevant aspects.

- We studied the effect of surface morphology, membrane thickness and active porosity on permeation of glucose in a *pure diffusion mode*. The glucose permeability could be tuned over an extending range with different structural/physical-chemical properties of the membranes. Membrane selectivity was assessed by comparing the effective diffusion

coefficients for a range of antibiotics, proteins and other biomolecules. Efficient selectivity is facilitated by a high degree of control on pore size. A desired selectivity could be achieved by involving other interactions of solute-solute or solute-membrane. The nanoporous membranes were finally tested as the outer membranes for amperometric glucose sensors.

- We have also tested the nanoporous 1,2-PB membranes in *convection mode* (ultrafiltration). A number of polyethylene glycol (PEG) molecules with different molecular weights dissolved in water or in ethanol-water were used to explore the effect of membrane fouling on flux and selectivity for the nanoporous membranes. The flux decline could be significantly diminished by changing the solvent property (i.e. the presence of ethanol) or surface property (i.e. hydrophilization). The experimental PEG rejection profiles were measured for the different systems and compared with Bungay-Brenner model based on molecule-pore size ratios. The nanoporous membranes showed distinct rejection properties based on different separation mechanisms, due to the adjustment of solvent property and surface property.
- Finally, we examined the *loading and release* of SDS detergent (sodium dodecyl sulfate) in nanoporous 1,2-PB membranes. We show that the SDS adsorption isotherm is well described by Langmuir model, and is consistent with the formation of a monolayer at the pore interface. We investigated the release process of the SDS out of nanopores in water and in methanol. Initial tests of the SDS-loaded nanoporous 1,2-PB membranes as anti-biofilm surfaces, showed promising results.

Dansk resumé

Membranteknologi er et vigtigt redskab i en lang række anvendelser inden for sundhedssektoren, fødevareindustrien, bæredygtig vandbehandling, energi konvertering og lagring mm. På trods af den udbredte brug af teknologien, er der behov for øget forståelse og forbedringer på en række centrale områder angående ydeevne, holdbarhed, omkostning mv. Specifikke begrænsninger for en given membrantype kan direkte relateres til de anvendte materialer og fremstillingsmetoder. Fremskridt i design og fremstilling af nanoporøse materialer, og i særdeleshed af nanoporøse polymerer, forventes at åbne nye udviklingsmuligheder indenfor membranteknologi. Nanoporøse polymermembraner fremstillet af selvorganiserende blok copolymerer er i centrum for det arbejde, vi præsenterer i denne afhandling.

Blok copolymerer består af makromolekyler sammensat af to eller flere kemisk forskellige blokke. Blok copolymererne kan selvorganisere i forskellige morfologier med karakteristiske størrelser i nanometer skalaen. Blok copolymerers selvorganisering er en kraftfuld og overkommelig princip til fabrikationen af nanoporøse materialer med veldefineret morfologi, porestørrelse og porestørrelses fordeling, porøsitet, og overflade kemi. Denne type af nanoporøse materialer er derfor attraktiv for regulering og detektering af stoftransport på molekylært niveau. Vi har brugt 1,2-polybutadien-*b*-polydimethylsiloxan (1,2-PB-*b*-PDMS) som blok copolymer til fremstilling af nanoporøse membraner.

Nanoporøse 1,2-PB membraner med gyroid bulk morfologi blev fremstillet via selektiv og kvantitativ ætsning af PDMS blokken i 1,2-PB-*b*-PDMS. Den gyroide struktur viser isotropisk perkolation uden behov for struktur pre-alignment. Strukturen på membranens ydre overflade kan styres fra at være lukket (kompakt) til åbnet (porøs) ved tilpasning af grænsefladeenergien mellem polymer og forskellige anvendte substrater i membrandannelsesprocessen. Overflade kemien i nanoporerne kan ændres vha. fotokemi til et specifikt behov. Det præsenterede arbejde i afhandlingen fokuserer på udforskning af tre relevante aspekter.

- Vi undersøgte effekten af overflademorfologi, membrantykkelse og aktiv porøsitet på gennemsivning af glukose i en ren *diffusions mode*. Membranens selektivitet vurderes ved

at sammenligne de effektive diffusionskoefficienter for en række antibiotika, proteiner og andre biomolekyler. De nanoporøse membraner blev til sidst testet som ydre membraner til amperometriske glukose sensorer.

- Vi har også testet de nanoporøse 1,2-PB membraner i *konvektions mode (ultrafiltrering)*. En række af PEG molekyler med forskellige molekylvægte opløst i vand eller i ethanol-vand, blev brugt til at udforske effekten af fouling på membranens fluks og selektivitet. Den eksperimentelle PEG størrelsesselektivitet målt for de forskellige systemer blev sammen-lignet med Bungay-Brenner modellen baseret på molekyle-pore størrelses forholdene.
- Endelig har vi undersøgt *load-release* af SDS sæbe (natriumdodecylsulfat) opløsninger i nanoporøse 1,2-PB membraner. Vi viser at SDS adsorption isotermen er godt beskrevet af Langmuir modellen, og stemmer overens med dannelsen af en monolag på pore grænsefladen. Vi undersøgte frigivelsesprocessen af SDS ud af nanoporerne i vand og i methanol. Indledende tests af SDS-loaded nanoporøse 1,2-PB membraner som anti-biofilm overflader, viste lovende resultater.

Table of Contents

Chapter 1 Scope and Outline

The aim of this thesis has been to explore the potential of block copolymer templated nanoporous polymers in membrane applications. A large amount of fundamental research from literature has been undertaken to study block polymers in the aspects of production, characterization, modification and property enhancement. Block copolymers have proven particularly advantageous for templating porous membranes. With nanoscale pores, high porosity, narrow pore size distributions, and tunable chemical and mechanical properties, the block copolymer derived nanoporous polymers hold tremendous potential as robust, efficient, and highly selective separation membranes. We have been thus motivated to systematically investigate membrane property and performance of these materials for different applications.

In this project, 1,2-polybutadiene-*b*-polydimethylsiloxane (1,2-PB-*b*-PDMS) has been selected to fabricate nanoporous 1,2-PB membranes since 1,2-PB-*b*-PDMS copolymer and its derived nanostructure have been well-developed and comprehensively characterized in the previous work by our group (Self-organized Nanoporous Materials group, DTU-Nanotech). The proposed membranes have been designed to hold the gyroid structure with bicontinuous nanoporosity across the entire membrane thickness without need of pre-alignment. Along with precise control over the bulk structure, the surface morphology and chemistry were intended to show diverse to match specific demands in different membrane applications. Membrane behaviors of the nanoporous 1,2-PB membranes have been investigated by evaluating permeability and selectivity in both diffusive mode and convective mode. The purpose is to understand the correlation of structural/ physical-chemical properties and functional properties of the membranes. Interests have been focused on the potential use as a permselective dialysis membrane for amperometric glucose biosensors and as an efficient ultrafilter. In addition, the nanoporous 1,2-PB membrane has been pursued as a sustained release membrane, thus research in adsorption isotherm, loading and release equilibrium and kinetics have been studied. A demonstration of anti-biofilm surface has been presented.

The thesis gives a general background in *Chapter 2*. It contains a short introduction to nanoporous polymers and membrane process and brief descriptions of membrane applications in biosensors, ultrafiltration, and control-release. *Chapter 3* presents a detailed description of the

preparation of nanoporous 1,2-PB membranes and the surface modifications used in this study. Structural characteristics, particularly surface morphology of the prepared membranes have been in detail clarified in *Chapter 4*. Hydraulic permeability and gas permeation as basic characteristics in membrane property are first presented in *Chapter 5*. *Chapter 6* focuses on the diffusive transport property of nanoporous 1,2-PB as a dialysis membrane. Following a series of fundamental characterizations of transport properties, the nanoporous membrane was taken as an outer membrane and tested in amperometric glucose sensors. In *Chapter 7*, a series of PEG molecules with varying molecular weights were used to explore the effects of membrane fouling on flux and rejection profiles for the nanoporous 1,2-PB membranes. *Chapter 8* describes the loading and release of SDS into/from the nanoporous 1,2-PB membranes. The SDS-loaded nanoporous 1,2-PB membranes were preliminarily tested as anti-biofilm surface to show the potential as a drug-release carrier. Finally, *Chapter 9* summarizes the thesis work and gives some suggestions for future work. The *Appendices* covers four topics, i.e. fabrication methods, etching process, DSC results and PEG diffusion tests.

The overall thesis is based on the publications and the submitted manuscripts listed below:

1) Li, L.; Wang, Y.W.; Vigild, M. E. Ndoni, S. Physisorption of SDS in a Hydrocarbon Nanoporous Polymer. *Langmuir* **2010**, *26* (16), 13457–13465.

2) Li, L.; Schulte, L.; Clausen, L. D.; Hansen, K. M.; Jonsson, G. E.; Ndoni, S. Gyroid Nanoporous Membranes with Tunable Permeability. *ACS Nano* **2011**, *5* (10), 7754 – 7766.

3) Li, L.; Szewczykowski, P.; Clausen, L. D.; Hansen, K. M.; Jonsson, G. E.; Ndoni, S. Ultrafiltration by Gyroid Nanoporous Polymer Membranes. *Journal of Membrane Science* **2011**, *384*, 126-135.

4) Li, L.; Yang, L.; Molin, S.; Ndoni, S. Sodium Dodecyl Sulfate (SDS)-Loaded Nanoporous Polymer as Anti-Biofilm Surface Coating Material. *Biofouling* **2011** (Has been submitted and reviewed).

Chapter 2 Introduction

An outline of the 'Introduction' chapter is illustrated in Figure 2.1. The key role in the overall thesis is block copolymer templated nanoporous 1,2-polybutadiene (1,2-PB); all the research has been developed in relation to this nanoporous polymer. Accordingly, we begin with a brief introduction to nanoporous materials, with a focus on nanoporous polymers. Specific attention is given to self-assembled block copolymer which is a structure-templating precursor for the production of nanoporous 1,2-PB membranes in this thesis. The aim of the thesis is to develop the potential of the nanoporous 1,2-PB in membrane applications. A brief introduction to membrane process is thus necessarily presented. The basic concepts and definitions are described to understand the membrane transport in relation to the membrane structure and chemistry, consequently the membrane performance in relation to the requirements in various applications. Three different membrane applications have been our interests in the thesis, i.e. biosensor membranes (chapter 6), ultrafiltration membranes (chapter 7) and sustainable release membranes (chapter 8). In chapters 2.3–2.5, we therefore present a general background for each application highlighting on the function and the importance of nanoporous polymers, but also pointing out relevant issues and concerns.

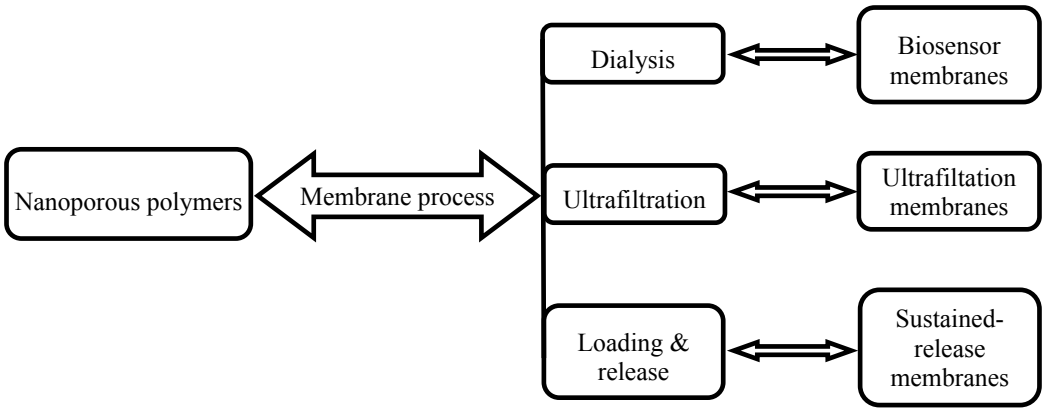

Figure 2.1 An outline of 'Introduction' chapter.

2.1. Nanoporous polymers

In the past few decades, nanomaterials have received substantial attention and efforts from academic and industrial world, due to the distinct properties at the nano-scale. Nanoporous materials as a subset of nanomaterials possess a set of unique properties: large specific surface-volume ratio, high interior surface area, exclusive size sieving and shape selectivity, nano-scale space confinement, and specific gas/fluid permeability. Moreover, pore-filled nanoporous materials can offer synergistic properties that can never be reached by pure compounds. As a result, nanoporous materials are of scientific and technological importance and also considerable interest in a broad range of applications that include templating, sorting, sensing, isolating and releasing.

Nanoporous materials can be classified by pore geometry (size, shape, and order) or distinguished by type of bulk materials. According to IUPAC, nanoporous materials can be subdivided to microporous materials (< 2 nm), mesoporous materials (2–50 nm) and macroporous (50–1000 nm).[1, 2] In the literature, nanoporous materials are mainly referred to as porous materials typically having pore diameter between 1 nm and 100 nm.[3, 4] Nanoporous materials are considered uniform if the pore size distribution is relatively narrow and the pore shape is relatively homogenous. The pores can be cylindrical, conical, slit-like, or irregular in shape. They can be well ordered with an alignment as opposed to a random network of tortuous pores. Nanoporous materials cover a wide variety of materials, which can be generally divided into inorganic, organic and composite materials. The majority of investigated nanoporous materials have been inorganic, including oxides, carbon, silicon, silicate, and metal.[3-5] On the other side, polymers have been identified as materials that offer low cost, less toxicity, easy fabrication process, diverse chemical functionality, and extensive mechanical properties. Naturally, the success of inorganic materials to form nanoporous materials has promoted the development of analogous polymers. More importantly, advances in polymer synthesis and novel processing techniques have led to various nanoporous polymers.

Table 2.1 reported in Ref 6 summarizes existing preparation approaches towards nanoporous polymers along with their characteristic pore size and density, film thickness, and structural uniformity.

Table 2.1 Summary of various fabrication approaches for the formation of nanoporous polymeric materials.[6]

Approach	Polymer used	Pore diameter /nm	Pore density/cm^{-2}	Film thickness	Film uniformity
Lithography					
Optical lithography	Various photoresists	~ 100	—[b]	—[b]	High[e(u)]
Electro-beam lithography	PMMA	10[b]	—[b]	—[b]	High[e(u)]
Aperture-array lithography	PMMA	200–350[b]	2.4 x 10^7– 4 x 10^8	160 nm	High[e(u)]
Colloidal lithography	PES	230	10^{9c}	0.5 μm	High[e(h)]
	PIP	55	5 x 10^9	0.5 μm	High[e(h)]
Pattern transfer					
Nanowire templated	PCL	20–30	5 x 10^9	0.5 μm	High
Molding/Imprint	PMMA	25	7 x 10^9	100 nm	High[e(u)]
	PS	25–30	5 x 10^{10c}	—[f]	High[e(h)]
Track etch	PC, PE	15	<10^9	5–20 μm	High
Solvent-based techniques					
Immersion precipitation	PVDF, PSF	20–120	—[f]	200 μm	Moderate
Phase separation	PCL	5–200	2 x 10^{8c}	50 μm	Low
CO_2 foaming	PIM, PSF	20–50	~ 10^{10c}	—[f]	Moderate-high
	PPQ	8–24	—[f]	20–50 μm	Moderate
Light-induced polymerization	Complex monomer mixture	20–40	—[f]	—[f]	—[f]
Block copolymer					
	PS-*b*-PMMA	15	5 x 10^{10c}	80 nm	Moderate-high
	PS-*b*-PL	16	10^{11c}	300 μm	High[e(h)]
	PS-*b*-PIP	20–30	~ 2 x 10^{10}	100–300 μm	High[e(g)]
Reactive pore formation	PS-*b*-PMMA	3–8	10^{11c}	30–300 nm	High[e(h)]
Substrate aligned pores	PS-*b*-PMMA	~ 25	~ 10^{11}	<0.1 μm	High[e(h)]
Electric-field aligned pores	PS-*b*-PMMA	14–50	10^{10}–10^{11c}	~ 1 mm	Moderate–high
Triblock copolymer	PL-*b*-PDMA-*b*-PS	19	10^{11c}	—[f]	High[e(h)]
Graft copolymer	PVDF-*graft*-POEM	~ 2	>10^{11c}	~ 3.5 μm[g]	Moderate–high
Asymmetric membranes	PS-*b*-PDMAEMA	20–80	—[f]	50 nm–1 μm[d], 85 μm total[g]	Moderate
	PS-*b*-P4VP	40	2.4 x 10^{10}	200–300 nm[d], 100 mm total[g]	High[e(h)]
Polyelectrolyte multilayers					
	PAA/PAH	50–200	—[f]	50–80 nm	High
	PAA/PAH/P4VP	10–50	—[f]	~ 25nm	Moderate
	PAA/PAH	30–40	~ 10^{10}	0.2–0.7 mm	Moderate–high
Spin assisted deposition	PAH/PSS	~ 40	~5 x 10^{10c}	15–30 nm	Moderate–high
Nanoparticle templated pores	PAA/PAH/silica nanoparticles	20–30	~2 x 10^{10}	<100 nm[c]	Moderate
Spatially patterned films	PAArVBA/PAH/PSS	~ 10	—[f]	~ 150 nm	—[f]
Asymmetric membranes	PEI/PAA	~100	—[f]	~ 10 μm	Low–moderate
Biologically derived materials					
Cellulose-based	Cellulose esters	<$10^{[h]}$	~ 10^{11}	>100 μm	Moderate
Cellular layers (S-layers)	Bacterium-based	4–5	>10^{11}	10's of nm[i]	High[e(p)]
Peptide-based multilayers	Polypeptides	50–150	—[f]	—[f]	—[f]
Engineered polypeptides	P(GPV)	_70	~5 x10^{9c}	8 nm[i]	Moderate–high

[a] Abbreviated polymers are as follows: PC—poly(carbonate), PE—poly(ester),PS—poly(styrene), PMMA—poly(methyl methacrylate), PL—poly(lactide), PIP—poly(isoprene), PAA—poly(acrylicacid), PAH—poly(allylamine hydrochloride), PCL—poly(caprolactone), PSS—poly(sodium-4-styrene sulfonate), POEM—poly(oxyethylene methacrylate), PVDF—poly(vinylidene fluoride),PDMA—poly(N,N-dimethylacrylamide), PDMAEMA—poly(N,N-dimethylaminoethyl methacrylate), P4VP—poly(4-vinylpyridine), PAArVBA—poly(acrylic acid-ran-vinylbenzylacrylate), PEI—poly(ethylene imine), PES—poly(ether sulfone), PSF—polysulfone, PIM—polyimide, P(GPV)—peptide polymer with glycine, L-proline, and L-valine monomer base units, PPQ—poly(phenylquinoxaline). [b] Highly dependent particular processing parameters. [c] Not reported, estimated from best available data. [d] Thickness of nanoporous layer; mounted/attached to a thick membrane. [e] Indicator for symmetry of layer: (h) hexagonal symmetry, (g) double gyroid network, (p) 2, 3, 4, or 6-fold symmetry, (u) user-defined patterns. [f] Results presented make it difficult to make reasonable estimates of these parameters. [g] Nanoporous region is a fraction of this reported thickness. [h] 1 kDa dialysis membranes indicate sub-10 nm pores are readily obtainable. [i] Crystalline cell layers are typically supported on polymer membranes. [j] Pore depth as measured with AFM. Likely an underestimate of total pore depth.

The techniques listed in Table 2.1 include lithography, pattern-transfer, track etching, solvent-based formation, layer-by-layer growth, block copolymer self-assembly, and various biologically derived materials. These techniques can be generally divided into two approaches: 'bottom-up' approach and 'top-down' approach. [7, 8]

'Top-down' approaches

Lithographic and *pattern-transfer* approaches[9, 10] utilize pre-defined patterns that are transferred into a polymer film, e.g. photoresist coating or template structure. The primary advantage of lithographic techniques is the ability to produce user-defined patterns. Optical lithography is the most widely used lithographic technique. Direct use of lithographic techniques requires a photo-cross-linkable or photodegradable polymer, which restricts potential materials selection.

Track etch technique can produce nanoporous membranes by irradiating polymers with high energy particles.[11] Porous structures can be generated by etching the linear paths of travel associated with incident particles within the polymer film. Since each pore is the result of a spatially random incident particle, agglomeration of pores limits maximum pore density in order to maintain a low dispersion in pore size. It is a useful approach for some commercial membranes.

'Bottom-up' approaches

Various *solvent-based* procedures take advantage of natural formation of nanostructured polymers via precipitation.[12, 13] The most prevalent are solvent-based precipitation techniques, which exploit solubility variations of a target polymer, depending on concentration, solvent, or process conditions. When initially dissolved in a good solvent, nanostructures can be induced from a polymer solution by solvent evaporation, cooling, or exposure to non-solvents (often water). Control of pore size and distribution is a challenge with this technique, but the ease and simplicity of this approach make it an attractive option.

Layer-by-layer (LbL) assembly forms layered structures of polyelectrolytes by the sequential deposition of cationic and anionic polymers, which take advantage of attractive and repulsive electrostatic forces.[14, 15] The primary limitation of this approach is available materials, which require a combination of polyelectrolytes. One drawback cited for LbL films is the lack of biocompatible materials.

Self-assembly of block copolymers employ a combination of polymer design and processing to allow formation of nanostructures (often highly ordered).[16, 17] Block copolymer (BCP) techniques make use of phase separation in polymers with two or more distinct chemical blocks. A wide range of structures have been demonstrated depending highly on the chemical functionality and block lengths. A common route to generate porous structures is through cross-linking and subsequent solvent removal of a degradable block. (We will draw specific attention to this technique, which has been a core fabrication method used in the thesis work.)

Finally, a range of biologically derived structures can form nanostructures, including widely available biomaterials such as cellulose, naturally forming structures like bacterial-derived crystalline cellular layers (S-layers), or synthetically engineered polypeptides.[18,19] Derivative forms of cellulose, such celluslose nitrate and cellulose acetate allow the use of solvent casting as a preparation technique.[20] The sysnthetic polypeptides have been deposited with LbL technique to form nanostructure. [21]

Block copolymers (BCPs)

This thesis focuses on nanoporous polymers derived from BCPs. The basic concepts will be given to understand the context of BCPs. Various approaches to create nanoporous materials from BCPs will be briefly described.

Block copolymers consist of two or more chemically distinct polymer chains connected at their ends via covalent bonds, which exhibit compositional heterogeneities on the nanometer scale. [22] Many modern synthetic techniques have contributed to an expanding number of BCP architectures classified by number of monomer types (e.g. ABA, ABC) and topology (linear versus branched sequencing).

The unique properties, and thus the applications, of BCPs rely on their mesoscopic (between 5 nm and 50 nm) self-assembly in the molten and solid states. For small molecules unfavorable enthalpy is often counter-balanced by entropy gain of mixing. Therefore $\Delta G_{mix} < 0$ is quite often and miscibility is quite common. For polymers the configurational entropy is significantly reduced therefore enthalpy is the determining factor for miscibility. Miscibility of polymers is seldom. If the respective blocks are sufficiently long, and unfavorable enthalpic interactions exist between them, they will then phase separate below the order-to-disorder transition (ODT) temperature. A minimum free energy configuration would form under a delicate balance of

interfacial energy, constraint of incompressibility as well as the entropic penalty of extended chain configurations.[22, 23] Block copolymers, therefore, form highly ordered supramolecular structures at the length of 5–50 nm. These phenomena have been studied by a large amount of theoretic and experimental work. We will restrict our attention to the simplest case of a linear AB diblock, consisting of two distinct segments.

A wealth of self-assembled structures can be determined by three experimental parameters, the overall degree of polymerization N, the composition f_A (i.e. the volume fraction of block A in the copolymer) and the Flory-Huggins interaction parameter χ.[22, 23] The first two parameters can influence the entropy factor; the interaction parameter χ represents the degree of incompatibility between the two blocks, which is inversely proportional to temperature.

Figure 2.2[24] illustrates a schematic microphase diagram of a linear diblock copolymer (block A represented by blue and block B by green), showing the dependence of morphology on both temperature, T and volume fraction of block A, f_A. As χN exceeds a critical value, a disorder-to-order transition (ODT) will occur. Below ODT, the AB diblock copolymer experiences transition through a body centered cubic spherical phase (BCC), a hexagonally packed cylindrical phase (HEX), a bicontinuous gyroid phase (GYR), and a lamellar phase (LAM).

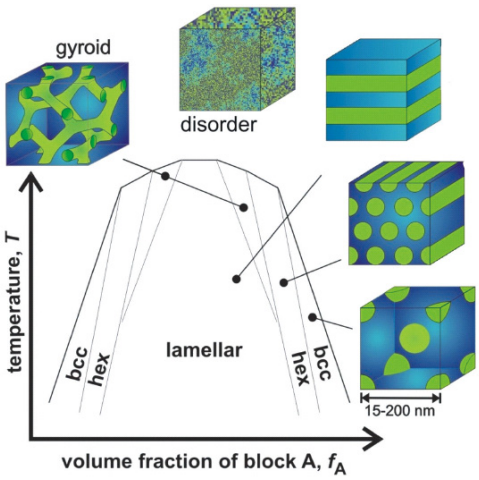

Figure 2.2 Schematic microphase diagram of linear AB block copolymers and representations of commonly observed morphologies.[24]

Nanoporous polymers can be generated by selective removal of one block from a self-assembled block copolymer with ozone, UV, oxygen plasma, base, acid, or fluorine compounds.

The first nanoporous polymer prepared from an ordered block copolymer poly(4-vinylphenyl-dimethyl-2-propoxysilane)-*b*-polyisoprene-*b*-poly(4-vinylphenyl-dimethyl-2-propoxysilane) (PPS-*b*-PI-*b*-PPS) was demonstrated by Lee et al. in 1988. [25] PI component was removed via ozonolysis-based degradation. Layered-like (lamellar) porous structure was obtained similar to that of segregated microphase of the precursor. In 1993, Hedrick et al.[26] published work on the preparation of nanoporous poly (phenylquinoxaline) (PPQ) with spherical morphology. The thermally labile blocks such as poly (propylene oxide) or poly (methyl methacrylate) were successfully removed by heating up above their decomposition temperatures. Later, the same group demonstrated formation of a series of nanoporous polyimides originally with different thermally degradable blocks in precursors. Liu et al.[27] demonstrated a new method to prepare cylindrical nanoporous poly(2-cinnamoylethyl methacrylate) (PCEMA) from PCEMA-*b*-poly(*tert*-butyl acrylate) (PCEMA-*b*-P*t*BA). The PCEMA block was first cross-linked by exposure to UV irradiation. PCEMA-*b*-P*t*BA was then treated in CH_2Cl_2 solution of trimethylsilyl iodide to hydrolyze *tert*-butyl groups. Poly (acrylic acid) was formed after the hydrolysis, generating the pores due to the leave of *tert*-butyl groups. Thurn-Albrecht et al.[28] created ordered hexagonally packed cylindrical porosity in polystyrene (PS) matrix by electric field aligning poly (methyl methacrylate) (PMMA) block in the precursor and removing it by UV irradiation. Xu et al.[29] reported a generation of nanoporous PS matrix via exposure of PS-PMMA to acetic acid/water mixtures without any prior UV treatment. Asakawa et al.[30] also achieved to selectively remove the PMMA phase from PS-PMMA by oxygen plasma reactive ion etching (O_2-RIE). Zalusky et al.[31] published a paper on the formation of nanoporous PS monoliths from the selective hydrolytic degradation of a PS-PLA diblock copolymer. In our group, Ndoni et al. successfully generated a series of nanoporous PI and PS by selectively and quantitatively etching PDMS with anhydrous hydrogen fluoride[32] or tetrabutyl ammonium fluoride[33].

An in-depth review of preparation of nanoporous materials from block copolymers is beyond the scope of this thesis and can be found in reviews by Hillmyer. [34]

Unique features like controllable morphology, tunable pore size and orientation, high porosity, narrow pore size distribution, and easy surface functionalization make the block copolymer derived nanoporous materials very attractive for many membrane applications.[34] A large amount of theoretical and experimental research from literature and our previous work gives a strong foundation for our attempts to develop nanoporous membranes from block copolymers and

explore great potential in membrane applications. The proposed membranes in this work will be designed to hold the gyroid structure with bicontinuous domains across the entire membrane thickness without need of pre-alignment. Along with control of the microstructure, the surface morphology and chemistry can be varied to match particular demands in different membrane applications. In order to understand the function and importance of membrane technology in relevant applications and optimize the membrane performance, it is necessary to give a short introduction to membrane process before further introducing specific membrane applications.

2.2. Introduction to membrane process

Every membrane separation process is characterized by the use of a membrane to accomplish a particular separation. The goal is to allow one or more components of a mixture to permeate the membrane readily while eliminating one or other components thereby producing a purified product. Membrane is at the heart of a membrane process and can be considered as a permselective barrier between two phases.[35] The ability to selectively transport components is attributed to differences in physical or chemical properties between the membrane and the permeating components. Passive transport through membranes takes place when a driving force is applied, i.e. a chemical potential gradient across the membrane in, e.g. concentration, pressure, electrical potential or temperature.[35]

The performance or efficiency of a given membrane is determined by two parameters: flux and selectivity. The flux of species through the membrane is proportional to the driving force as described by the equation 2-1,

$$J_i = -L_p \frac{\Delta F_i}{l} \qquad (2\text{-}1)$$

The driving force ΔF_i can be expressed as the gradient of a pressure or concentration difference across the membrane, as summarized in Table 2.2[35]. The proportionality coefficient that relates the flux to the driving force is called the membrane permeance, L_p / l. The permeance is the quotient of the permeability of species L_p, an intrinsic material property and the effective membrane thickness *l*.

Selectivity, a measure of a membrane's ability to separate the components of a mixture, can be expressed by the retention (*Ret*) or the separation factor (α). For a dilute solution, the retention R towards the solute can be defined as

$$\mathrm{Ret} = \frac{c_f - c_p}{c_f} = 1 - \frac{c_p}{c_f} \qquad (2\text{-}2)$$

where c_f is the solute concentration in the feed and c_p is the solute concentration in the permeate.

Table 2.2 Phenomenological equations. [35]

Mass flux	J_m	$= -D\,\Delta c/l$	Fick	Diffusion coefficient
Volume flux	J_v	$= -L_p\,\Delta P/l$	Darcy	Permeability coefficient
Heat flux	J_h	$= -\lambda\,\Delta T/l$	Fourier	Thermal diffusivity
Momentum flux	J_n	$= -\upsilon\,\Delta v/l$	Newton	Kinematic viscosity
Electrical flux	J_i	$= -1/R\,\Delta E/l$	Ohm	Electrical conductivity

For a mixture consisting of components *i* and *j* the separation factor is expressed by

$$\alpha_{i/j} = \frac{c_{pi} / c_{pj}}{c_{fi} / c_{fj}} \qquad (2\text{-}3)$$

where c_{pi} and c_{pj} are the concentrations of the components in the permeate and c_{fi} and c_{fj} are the concentrations of the components in the feed. The separation factor α is defined in such a way that its value is greater than unity, e.g. if component *i* permeates preferentially then the separation factor is given by $\alpha_{i/j}$.

Membrane with high flux and selectivity are desired for economic process design. A high selectivity depends on the selection of membrane material. Once the material is selected, the permeability of the different components is fixed. In order to achieve the high permeance (e.g. low membrane resistance) desired, the effective membrane thickness should be as thin as possible.

The barrier structure of membranes can be classified according to their porous character (Table 2.3[36]). Accordingly, various membrane processes can be accomplished based on the barrier structure by use of different driving forces. For nonporous membranes, e.g. reverse osmosis, pervaporation, and gas separation membranes, transport occurs by molecular diffusion and is described by the solution-diffusion model[37]. In this case, permeants dissolve in the membrane material and then diffuse through the membrane down a concentration gradient. The free-

volumes in the membrane are tiny spaces between polymer chains caused by thermal mothion of the polymer molecules; they appear and disappear on about the same timescale as the motions of the permeants traversing the membrane. The membrane permeability is determined by solubility of the permeants in the membrane and diffusion coefficient of the permeants through the membrane.

Table 2.3[36] Classification of membrane processes according to the membrane structure and driving forces.

Membrane structure	Pore size (d_p)	Driving force		
		Concentration	Pressure	Electric field
Nonporous		Pervaporation	Gas separation	Electrodialysis
			Reverse Osmosis	
Microporous	≤ 2 nm	Dialysis (D)	Nanofiltration	
Mesoporous	2–50 nm	Dialysis	Ultrafiltration (UF)	Electrodialysis
Macroporous	50–500 nm		Microfiltration	

For porous membranes, transport occurs by convective flow with some form of sieving mechanism, e.g. size/shape sieving or adsorption.[37] Interactions of solutes with the pore surface may significantly affect the membrane performance. For instance, the surface diffusion and Knudsen diffusion are involved in the use of microporous membranes for gas permeation.[37] The rejection of charged substances in aqueous solutions by microporous nanofiltration membranes may occur due to their Donnan potential.[35] Furthermore, with meso-membranes, selective adsorption can be used for an alternative separation mechanism, for example affinity membrane absorbers in hemodialysis applicaitons.[38] It is worth mentioning that both concentration polarization (due to the enhancement of the concentration of rejected species on the membrane surface as function of transmembrane flow) and membrane fouling (due to undesired adsorption or deposition of matter on/in the membrane) can severely reduce the membrane performance which would be expected based on intrinsic membrane properties.[39]

Nowadays, membrane separation technologies have been commercially established in large scale, i.e. dialysis for blood detoxification and plasma separation; reverse osmosis for the production of ultrapure water; ultrafiltration for many concentration, fractionation or purification processes. A more detailed overview on industrial separations using the main membrane technologies can be found in Refs[35, 40].

Some general rules have to be considered as we design or select new membranes for specific applications. Figure 2.3[5] summarizes the critical membrane characteristics that determine performance of membranes required in various applications. First, the ability to fabricate membranes with a desired pore size and a narrow pore size distribution will enable a precise control over molecular transport. Second, in many applications a low flow resistance to enable high flux is desired, indicating high porosity and low membrane thickness. Third, an adequate mechanical strength with respect to transmembrane pressure and sufficient thermal and chemical stability under a wide range of environment are essential for long-term usage. Finally, proper selection of material or surface functionalization of existing membrane will be beneficial to the membrane performance by minimizing the probability of concentration polarization and membrane fouling.

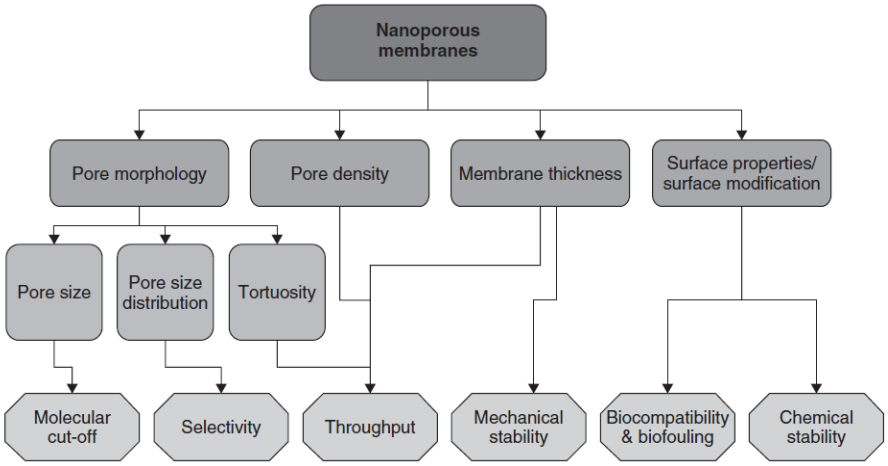

Figure 2.3 A schematic diagram of key membrane characteristics that affect the performance. [5]

In the thesis work, nanoporous polymers are derived from self-assembled BCPs having characteristic size at the range of 5–50 nm, thus they can refer to mesoporous membranes as defined in Table 2.3. Mesoporous membranes are very often used in dialysis or ultrafiltration for a wide range of applications. In addition, narrow pore size distribution and large surface-to-volume ratio inspired that this nanoporous polymer may have good capability in controlled release. We have been thus motivated to extensively investigate membrane property of this type

of nanoporous polymers in pure diffusive mode for dialysis (chapter 6) and in convective mode for ultrafiltration (chapter 7). The loading and release of the nanoporous polymers has been also studied (chapter 8). Therefore, in the following three subchapters we give a background to the relevant applications for which we aim to explore the nanoporous polymer as an appropriate membrane (i.e. dialysis membrane, ultrafiltration membrane, and sustained release membrane). The topics will focus on functions required in each membrane application and in turn the membrane transport properties needed, as well as some common concerned issues.

2.3. Membranes for biosensors

Impressive publications and patents, doubtlessly, suggest a continuing bright future for R&D activities in biosensor technology, particularly in blood glucose sensing because of its abundant market potential. However, commercial adoption has significantly lagged behind the research output. This could be attributed to cost considerations and some key technical barriers such as stability, detection sensitivity, and reliability. [41-43] Membrane technology has been realized as a useful and cost-effective tool to overcome the technical difficulties in many established sensor systems. The membrane structure may be rather diverse but they should fulfill at least one of the following main functions:[36]

- barrier between the sensor system and its environment, allowing selective permeation of analytes to the receptor while hindering interferences from the environment;
- matrix for the immobilization of the receptor or tool for bringing it into proximity to the detector.

Effective polymers are designed or selected on the basis of knowledge of the way in which polymer structure governs those properties of relevance to a particular biosensor application. Three groups of membrane properties must be considered in selecting polymer membranes for biosensor applications.[44] The first relates to the transport behavior of the polymer and encompasses permeability, permselectivity and transmembrane potential. These are important to different extents in different types of sensors e.g. potentiometric, amperometric, fiber optic, etc. The second group of properties relates to the role of the membrane as an immobilization matrix. Often the sensed species is so large (as in antibody/antigen interactions) that the polymer is

configured so as to enable unmodulated diffusion to specific sites.[45] The third group of properties relates to surface and interface behavior. These properties are in many ways the most difficult to control without compromising other functions of the polymer, e.g. permeability. Even so, surface and interfacial phenomena are extremely important in the overall performance of a given biosensor, both because of their contribution to transport phenomena and their role in controlling biocompatibility.

A real progress in membrane technology has been noticed in recent years with an obvious benefit in the design of biosensors. Glucose oxidase immobilized in porous nanocrystalline TiO_2 film is shown to be capable of sensing blood glucose.[46] Recently a glucose sensing system based on nanoporous platinum electrode embedded in a microfluidic chip comprising a microfluidic transport channel network and a miniaturized electrochemical cell has been demonstrated.[47] Bohn et al.[48] have proposed exploiting an array of electrically switchable nanocapillary membranes to perform sequential sensing and analytic operations in μTAS devices.

Here we limit our primary concern with amperometric glucose biosensors. When it comes to glucose biosensors, we should first date back to the first historic experiment (Leland C. Clark) that served as the origin of glucose biosensors.[49] Their first device relied on a thin layer of glucose oxidase enzyme (GOx) entrapped over an oxygen electrode (via a semipermeable dialysis membrane), and monitoring the oxygen consumed by the enzyme-catalyzed reaction:

$$\text{glucose}+O_2 \xrightarrow{\text{GOx}} \text{gluconic acid}+H_2O_2 \qquad (2\text{-}4)$$

On the other hand, lower glucose content results in more hydrogen peroxide. Guilbault and Lubrano[50] described in 1973 an enzyme electrode for the determination of blood glucose based on amperometric (anodic) monitoring of the liberated hydrogen peroxide:

$$H_2O_2 \rightarrow O_2+2H^++2e^- \qquad (2\text{-}5)$$

Hence, either the consumption of oxygen or the production of hydrogen peroxide can be detected with electrodes measuring glucose concentration. First-generation devices have relied on the use of the natural oxygen, and the production and detection of hydrogen peroxide (equations 1 and 2) as shown in Figure 2.4[51]. It consists of polycarbonate membrane (outer membrane), immobilized enzyme (enzyme layer), cellulose acetate membrane (inner membrane) and platinum electrode. Today, commercial glucose sensors in market are mainly based on this classic model, including: Yellowsprings instruments (YSI), Nova's StatStrip™, Abbott Laboratories, Bayer AG, Roche Diagnosti, etc.[51] These biosensors have been made available in

the market in various shapes and forms such as glucose pens and glucose displays. Innovation is increasingly driven by automation, miniaturization and system integration with high throughput for multiple tasks.[52]

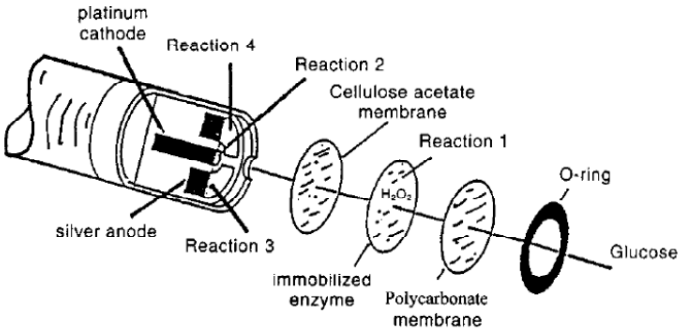

Figure 2.4 Schematic drawing of a 'first-generation' glucose biosensor (based on a probe manufactured by YSI Inc.).[51]

A clinically useful sensor for the continuous monitoring of glucose must satisfy the following characteristics: [53]

- Fast response — change in glucose concentration must be detected within 1–5 minutes, depending on the specific application;
- Accuracy — glucose level must be measured within minimum errors due to the presence of interfering species or changes in physiological parameters;
- Sensitivity — the signal to noise ratio must be large and a detectable signal must result from small e.g. 0.1 mM changes in glucose concentration;
- Range — all glucose concentrations in the physiological (normoglycernia) and pathophysiological range (hypo- and hyperglycernia) from 1 to 30 mM must be measurable;
- Stability — depending on the specific application, the signal due to glucose must not deviate more than ±5% of its average value during the operational time of the measuring instrument;
- Biocompatibility — have proved to be the major barriers to the development of reliable implantable devices.

These characteristics require significant improvements of the biosensor performance in terms of selectivity, detection sensitivity, and biocompatibility. One of the strategies is the use of a suitable outer membrane to facilitate a prolonged and reliable operation in whole blood. The outer membrane is expected to mechanically protect the sensor, prevent against protein adsorption or interferent's fouling, and filter out interfering substances. Most importantly, it can regulate glucose diffusion well below the saturation threshold of enzyme layer and the level of dissolved oxygen to the enzyme layer, thus allowing a linear response in the biosensor. Changes in diffusion coefficients of outer membrane make it possible to regulate the sensor operational range, response time and sensitivity. For the use as an outer membrane, various materials have been reported such as polyvinyl chloride, polyethylene, polymethacrylate, polyurethane, a series of polycarbonate, silicone rubber, porous silicon membrane and amphiphilic polymers.[54]

The outer membrane used in a glucose biosensor in principle functions as a semi-permeable dialysis membrane. The transport mechanism can be described by Fick's law and, the solute diffusion in a porous membrane and its free diffusion in water can be correlated by equation 2-7.

$$J_i = \frac{D_{eff}}{l}\Delta c_i \qquad (2\text{-}6)$$

$$D_{eff} = \frac{\varepsilon\delta(r)D_\infty}{\tau} \qquad (2\text{-}7)$$

Theoretically, if considering the need for restricting glucose diffusion alone, we can increase the membrane thickness l and tortuosity τ, and/or decrease the porosity ε. Constricivity $\delta(r)$ can be also adjusted to diminish the glucose permeation by increasing the size exclusion and hydrodynamic hindrance in the pores. On the other side, a fast response is desired in sensor performance. This is characterized by a short diffusion time of glucose across the membrane. At this point, we need to decrease the membrane thickness and tortuosity, and increase pore radius r to achieve a higher effective diffusion coefficient D_{eff}. At the same time, we should take other considerations into account. For instance, high oxygen permeability of the membrane is required to allow enough oxygen available in the enzyme layer; the membrane should also have proper pore size to precisely filter out the undesired proteins and interferences. By making a compromise to all the demands above, we may theoretically conclude that a thin membrane with relatively low porosity and proper pore size is desired for an outer membrane in amperometric glucose sensors. In addition, flexibility and biocompatibility in relation to mechanical property and surface chemistry of the outer membranes are also critically important.

We attempt to develop nanoporous 1,2-PB polymers as outer membranes in amperometric glucose biosensors. In this thesis work, we begin with our effort to evaluate the 1,2-PB nanoporous membranes by a series of fundamental work. Various relevant characters, such as skin structure, intrinsic porosity /active porosity, thickness and surface modification are considered to optimize the membrane performance in amperometric enzyme-based sensors. Details will be presented and discussed in chapters 3, 4 and 6. If the nanoporous 1,2-PB membranes are assessed not to be a good candidate as the outer membrane, this fundamental work can still provide an useful information to understand transport properties of this membrane used in dialysis and may open up other new applications, e.g. hemodialysis. In addition to dialysis, developing the nanoporous membranes as an efficient ultrafiltor for different applications is also one of our interests. Therefore we present a short introduction to ultrafiltration membranes in the succeeding subchapter.

2.4. Membranes for ultrafiltration

Ultrafiltration (UF) is typically used to separate macromolecules and colloids from a solution, e.g. water or microsolutes. The average pore size of the membranes used is in the 1–100 nm range. [3,4] Nowadays, ultrafiltration has been used in a wide field of applications such as food and dairy industry, pharmaceutical and biotechnology industry, textile industry, chemical industry and so on. The first large successful application was the recovery of electrocoat paint in automobile plants.[37] Later, various applications developed in the food and diary industries, first in the production of cheese, then in the production of juices and, more recently, in the production of alcoholic beverages. Industrial wastewater and process water treatment is a growing application, but high costs limit growth.

UF membranes have an asymmetric structure traditionally made by the Loeb-Sourirajan process,[55, 56] having a much denser toplayer (smaller pore size and lower surface porosity) on a much open micro-size substrate. The finely porous toplayer serves the separation with a much higher hydrodynamic resistance; the microporous support provides mechanical strength. An ultrafiltration membrane normally functions through size/shape sieving mechanism. The cut-off

of ultrafiltration is usually characterized by solute molecular weight. However, the shape of the molecule can give an import impact on the rejection.[37] Flexible, linear macromolecules usually have rejection much lower than the rejection measured for rigid, globular proteins of the same molecular weight. It is considered that linear polymers can be able to snake through the membrane pores under perturbed states as triggered by external forces; while protein molecules exist in solution as tightly wound globular coils hold together by hydrogen bonds. These globular molecules can not deform to pass through the membrane pores and are therefore rejected. In addition, the solution environment e.g. pH, ionic strength, can also affect permeation through ultrafiltration membrane, particularly with polyelectrolytes.

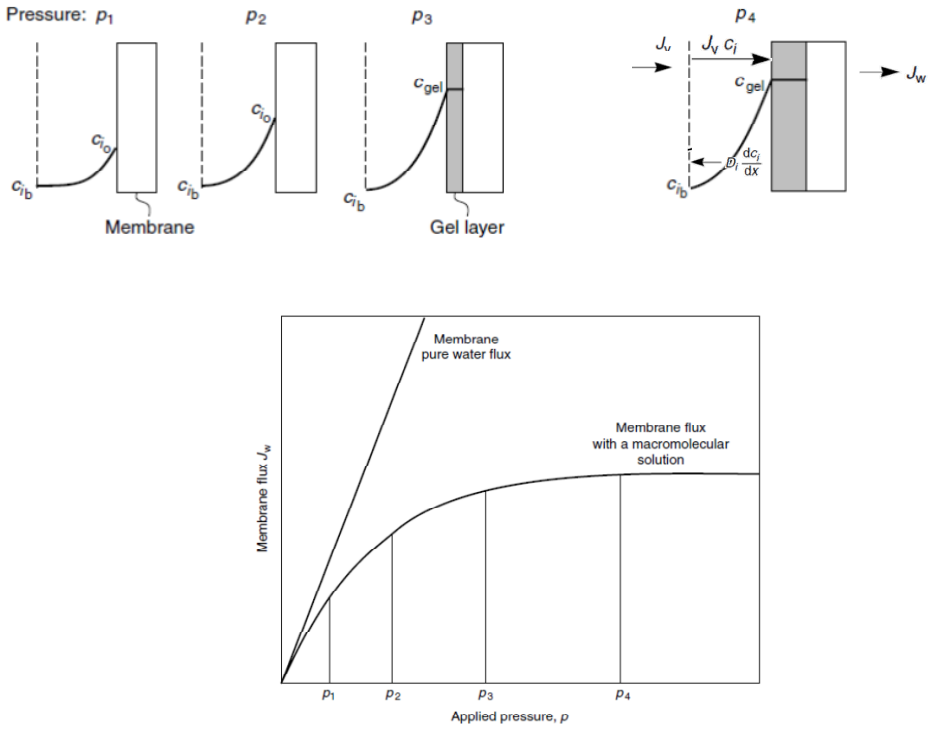

Figure 2.5 The effect of pressure on ultrafiltration membrane flux and the formation of a secondary gel layer. Ultrafiltration membranes are best operated at pressures between p_2 and p_3 at which the gel layer is thin. Operation at high pressures such as p_4 leads to formation of thick gel layers, which can consolidate over time, resulting in permanent fouling of the membrane2.6.[37]

Concentration polarization and membrane fouling are inherent features of ultrafiltration. The process performance in ultrafiltration is, therefore, not equal to the intrinsic membrane properties in actual separations. The retained macromolecular solutes accumulate at the membrane surface resulting in a concentration build-up. At steady state, the convection flow of the solute to the membrane equals to the diffusional back-flow from the membrane to the bulk solution. As the applied pressure further increases, a limiting flux will be attained due to an increase in the resistance of the boundary layer as seen from Figure 2.5[37]. The concentration of the accumulated solutes may become so high that a gel layer can be formed as called membrane fouling—deposition of retained colloidal and macromolecules on the membrane surface. Concentration polarization and membrane fouling can result in severe flux decline, undesired rejection behavior and shorten membrane lifetime. Thus, except the intrinsic properties that determine the flux and selectivity of membrane in ultrafiltration, the ability to reduce fouling is one of the critical considerations. Surface functionalization of established membranes is a key route in membrane development; the major aim is to improve the performance of the existing material by either minimizing undesired interactions to improve the selectivity or by introducing additional (tailored) interactions to create an entirely novel separation function.

Most of today's ultrafiltration membranes are made by variations of the Loeb–Sourirajan process.[37] A limited number of materials are used, primarily polyacrylonitrile, poly(vinyl chloride)–polyacrylonitrile copolymers, polysulfone, poly(ether sulfone), poly(vinylidene fluoride), some aromatic polyamides, and cellulose acetate. In general, the more hydrophilic membranes are more fouling resistant than the completely hydrophobic materials. For this reason water-soluble polymers such as poly(vinyl pyrrolidone), poly(ethylene glycol) or poly(vinyl methyl ether) are often added to the membrane casting solutions used for hydrophobic polymers such as polysulfone or poly(vinylidene fluoride). Because the pore size and thickness of these membranes can be altered by changing the process conditions, the flux can be adjusted without much difficulty. At present, phase inversion is one of dominating techniques to prepare UF membranes in industry due to its ease and simplicity. One of the main issues is insufficient membrane selectivity. The wide distribution of pore sizes (Figure 2.6a) causes a broad molecular weight cut off, which limits their applicability to many applications.[57] Composite membranes have been developed with a robust, inexpensive membrane with micrometer-size pores as a mechanical support and a thin highly selective layer deposited onto the support.

Advances in polymer processing and polymer synthesis are being made to optimize the membrane performance in UF. Track-etched polycarbonate (PC) membranes are shown in Figure 2.6b.[58] The pore size distributions are narrow for these membranes, thus having a much sharper molecular weight cut-off. However the low pore density results in this type of membranes showing a very low flux. Figure 2.6c shows anodized aluminum oxide (AAO) membranes with a uniform pore size and relatively higher porosity2.6.[59] The mechanical property of this kind of materials is usually week so that they can not withstand a high pressure in convection flow mode. Figure 2.6d shows a hexagonally packed cylindrical 1,2-PB nanoporous membranes obtained from a block copolymer 1,2-PB-*b*-PDMS.[33] The contrast between this panel and the other samples is impressive. It shows a membrane with a void fraction comparable to a conventional ultrafiltration membrane but with pore geometry similar to track etched membranes. These membranes also possess adjustable mechanical properties relative the AAO membranes. Therefore block copolymer-based nanoporous polymers have high potential to improve ultrafiltration membranes. In addition, membranes showing selectivity that can be switched by an external stimulus or can adapt to the environment/process conditions is a recent development in the field.[60]

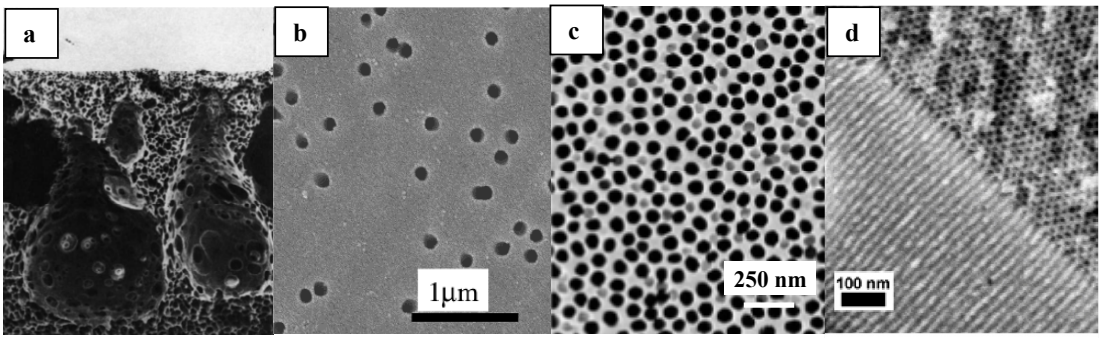

Figure 2.6 SEM images of different types of ultrafiltration membranes: **a.** Cross-section of an asymmetric polysulfone membrane made by dry/wet phase inversion using convective evaporation, magnification 500X;[57] **b**. Top view of a polycarbonate track etched membrane; [58] **c**. Top view of an anodic aluminum oxide membrane; [59] **d**. two (fracture) surfaces of hexagonally packed cylindrical nanoporous membrane from block copolymer 1,2-PB-*b*-PDMS, the upper right-hand part of the picture displays an "end view" of the cavities, and the lower left-hand a "side view" of the structure. [33]

Here, we limit our attention to block copolymer derived nanoporous membranes. Using block copolymers as a template to fabricate nanoprous membranes shows high potential in developing membranes with a narrow and adjustable pore size distribution, high porosity, and easy surface

functionalization. Several recent studies have examined the performance of block copolymer derived nanoporous membranes as UF membranes. Russell et al.[61] developed an asymmetric membrane showing ultrahigh selectivity and flux for the filtration of viruses where a thin nanoporous layer from PS-*b*-PMMA functioned as a dense top-layer. Later, good dimensional stability under high pressures and excellent solvent resistance was also reported for the same type of nanoporous block copolymers for the virus filtration.[62] Block copolymer templated nanoporous membranes are also highly considered as next-generation membranes for waste water treatments.[63] Hillmyer et al. [64] has studied gas and water liquid transport through nanoporous membranes based on block copolymers for water treatment. Later, they reported ultrafiltration across nanoporous polydicyclopentadiene-based membranes, showing a significant sharper molecular cutoff curves than commercial membranes.[65]

One of the main objectives in the thesis work is to explore in detail the transport properties of the nanoprous 1,2-PB membranes in ultrafiltration and challenge its capability as an ultrafilter. Double bonds in 1,2-PB allow the nanoporous matrix with an intrinsic active surface. An extensive of modification methods have been investigated and developed by the Ph.D. students in our groups[66-68]. In this thesis work, surfactant physisorbtion method[69]2.6, UV photooxidation[68] and thiolene chemistry[67] are considered because of low-cost, simple and efficient attributes. Details of our work in UF will be reported and discussed in chapters 3, 4, 5 and 7.

As reported in a perspective article by Hillmyer et al.,[70] in addition to ultrafitlration application in sustainable water treatment, block copolymer derived nanoporous polymers are also very attractive to controlled drug delivery. The third aim of the thesis work is to develop the nanoporous 1,2-PB polymers as sustained-release films for drug delivery, by use of both the large surface-to-volume ratio for immobilizing sufficient drug within a small volume and the unique nano-structure for regulating the permeation rate of a drug. In the following subchapter, we give a short introduction to membrane technology in controlled delivery application.

2.5. Membranes for controlled release

Controlled delivery systems are designed to release definite amounts of therapeutic agents to a specific site over prolonged duration time and with a definite kinetics.[37, 38, 71] The advantages of

controlled release include greater drug effectiveness, better balanced drug concentrations in the body, and more convenience to the patient. The local delivery eliminates the risks of side effects associated with oral or parenteral therapies such as systemic toxicity. It also improves the efficacy of the treatment by achieving higher drug concentrations at target site than those reachable with systemic administration. [37, 38, 71]

Membrane-based controlled release delivery systems have been widely used in a variety of (bio-) medical applications, such as treatment of ophthalmologic disorders, heart disease, contraception, bone infection prophylaxis and existing osteomyelitis.[72-74] In controlled drug delivery systems a membrane is used to moderate the rate of delivery of drug to the body. In some devices the membrane controls permeation of the drug from a reservoir to achieve the drug delivery rate required. Other devices use the osmotic pressure produced by diffusion of water across a membrane to power miniature pumps. In yet other devices the drug is impregnated into the membrane material, which then slowly dissolves or degrades in the body. Drug delivery is then controlled by a combination of diffusion and bioderadation. By tailoring the properties of the membrane at the molecular level, one can effectively design materials that possess specific release kinetics. The kinetics can be designed so as to provide a sustained release of drug delivery in the desired application of the membrane. Rose and Nelson[38] were responsible for the first introduction of membranes for controlling drug release using osmotic pumps. ALZA[38] in 1973 originally introduced the OROS oral drug delivery technology to the market as a gastrointestinal transport system. In the past decades, membrane-based controlled release drug delivery systems have been an important field in both academic and industrial worlds.

Nanoporous membranes with large surface-volume ratio, well-controlled pore size, porosity, and membrane thickness offer an attractive route for making capsules that may be used for providing controlled release of pharmacologic agents. [75] For example, nanoporous materials are researched for use in drug eluting stents to treat coronary artery disease.[76] Recently, nanoporous inorganic membranes have been tested for sustained release of ophthalmic drugs to treat conditions related to the eye. [77] When coupled to biosensors, smart drug delivery systems that respond to physiological conditions could be developed. Especially, a novel development in stimuli responsive nanoporous membranes triggers a new perspective for controlled release delivery systems.[60] The deposition of “intelligent polymers” onto the surfaces of membrane pores can create permeation switches or gates. For example, incorporation of a drug within a

biodegradable, biocompatible polymer nanostructure is a promising approach. The combination of the environmentally-sensitive hydro gels within micro/nano porous polymer matrices is presently researched for developing a novel intelligent drug delivery system. [78] These polymer gels undergo reversible swelling changes in response to small changes in pH, temperature, intensity of light as well as magnetic and/or electric fields, causing the release of an active agent at predetermined intervals. Precise control over the release of drug from the micro-reservoirs may be enabled by integrating the system with temperature, pH, magnetic and electric fields. The volume swelling hydro gel in the system releases active compounds at a precisely predefined rate, thus delivering them to the right place in right amounts.

The existing types of membrane-based controlled drug delivery systems include diffusion-controlled, osmotically controlled, swelling-controlled, and chemically controlled systems.[38] Specific attention will be given to diffusion-controlled systems which find broad commercial application. In diffusion controlled membrane systems, the drug release is controlled by transport of the drug across a membrane. The transport depends on the drug diffusivity through the membrane and the thickness of the membrane, according to Fick's law[37]. The membrane can be porous or non-porous and biodegradable or not. These systems find broad application in pills, implants and patches.

Exploring the potential of block copolymer-derived nanoporous matrices as a controlled release system is of our great interest. A variety of fast responses and flexible drug delivery systems can be attempted following three aspects: 1) a porous matrix for directly incorporating drugs. Particularly, for nanoporous 1,2-PB membranes, their mechanical property can be extended over a large range mainly depending on cross-linking degree.[79,80] Therefore, it is also possible to make it to be a hydrogel. Membrane pores can be open/ blocked as swelling is stimulated. 2) A porous substrate for supporting "intelligent polymers", e.g. UV cure stimuli-sensitive hydro gels with entrapped enzymes and/or drugs. 3) Rate-controlling layers covering reservoirs of therapeutic agents.

Standing at the start line, we take amphiphilic molecule SDS as a model molecule. Both equilibrium and kinetics in loading and release are investigated for highly cross-linked nanoporous 1,2-PB matrix. The second purpose of this work is to develop a simple and fast surface modification approach via physisorption of SDS.[69] Details will be presented and discussed in chapters 3, 4 and 8.

2.6. References

[1] Polarz, S.; Smarsly, B. Nanoporous Materials. *Journal of Nanoscience and Nanotechnology* **2002**, *2*, 581– 612.

[2] Rouqerol, J; Avnir, D.; Fairbridge, C. W.; Everett, D. H.; Haynes, J. H.; Pernicone, J. D.; Ramsay, J. D.; Sing, S. W.; and Unger, K. K. *Pure Appl. Chem.* **1994**, *66*, 1739.

[3] Lu, G. Q.; Zhao, X. S. Nanoporous Materials: Science and Engineering. Imperial College Press: London, **2003**.

[4] Nanoporous Materials. Holister, P.; Roman, C; Harper, T. Cientifica, **2003**.

[5] Adiga, S. P.; Jin, C.; Curtiss, L. A.; Monterio-Riviere, N. A. and Narayan, R. J. Nanoporous Membranes for Medical and Biological Applications.

[6] Bernards, D and Desai, T. A. Nanoscale Porosity in Polymer Films: Fabrication and Therapeutic Applications. *Soft Matter* **2010**, *6*, 1621–1631.

[7] Mijatovic, D.; Eijkel, J. C. T.; van den Berg, A. Technologies for Nanofluidic Systems: Top-Down vs. Bottom-up—A review. *Lab Chip*, **2005**, *5*, 492–500.

[8]Cheng, J. Y.; Ross ,C. A.; Smith, H. I.; Thomas, E. L. Templated Self-Assembly of Block Copolymers: Top-Down Helps Bottom-Up. *Advanced Materials* **2006**,18, 2505–2521.

[9] Madou, M. J. Fundamentals of Microfabrication. CRC, Boca Raton, 2nd edn, **2002**.

[10] Martin, C. R. *Science* **1994**, *266*, 1961–1966.

[11] Fleischer, R. L. Tracks to Innovation: Nuclear Tracks in Science and Technology. Springer, New York, **1998**.

[12] Akthakul, A.; McDonald, W. F. and Mayes, A. M. *J. Membr. Sci.* **2002**, *208*, 147–155.

[13] Krause, B.; Diekmann, K.; van der Vegt, N. F. A. and Wessling, M. *Macromolecules* **2007**, *40*, 2070–2078.

[14] Decher, G. *Science* **1997**, *277*, 1232–1237.

[15] Zhang, X.; Chen, H. and Zhang, H. Y. *Chem Commun.* **2007**, 1395–1405.

[16] Park, C.; Yoon, J. and Thomas, E. L. *Polymer* **2003**, *44*, 6725 – 6760.

[17] Hashimoto, T.; Tsutsumi, K.; Funaki, Y. *Langmuir* **1997**, *12*, 6869 – 6872.

[18] Sara, M.; Sleytr, U. B. *J. Bacteriol*. **2000**, *182*, 859 – 868.

[19] Sleytr, U. B.; Sara, M. *Trends Biotechnol.* **1997**, *15*, 20–26.

[20] Kamide, K. Cellulose and Cellulose Derivatives, Elsevier Science, Amsterdam, **2005**.

[21] Zhong, Y.; Whittington, C. F.; Zhang, L. and Haynie, D. T. *Nanomed. Nanotechnol. Bol. Med.* **2007**, *3*, 154–160.

[22] Bates, F. S.; Fredrickson, G. H. *Annu. Rev. Phys. Chem.* **1990**, *41*, 527.

[23] Bates, F. S. *Science* **1991**, *251*, 898.

[24] Vigild, M. E.; Ndoni, S.; Mortensen, K. *Dansk Kemi* **2004**, *11*, 32.

[25] Lee, J.-S.; Hirao, A.; Nakahama, S. *Macromolecules* **1988**, *21*, 274.

[26] Hedrick , J. L.; Labadie, J.; Russell, T.; Hofer, D.; Wakharker ,V. *Polymer* **1993**, *34*, 4717.

[27] Liu, G.; Ding, J.; Guo, A.; Herfort, M.; Bazett-Jones, D. *Macromolecules* **1997**, *30*, 1851.

[28]Thurn-Albrecht, T.; Schotter, J.; Kastle, G. A.; Emley, N.; Shibauchi, T.; Krusin-Elbaum, L.; Guarini, K.; Black, C. T.; Tuominen, M. T.; Russell, T. P. *Science* **2000**, *290*, 2126.

[29] Xu, T.; Stevens, J.; Villa, J. A.; Goldbach, J. T.; Guarini, K. W.; Black, C. T.; Hawker, C. J. Russell, T. P. Adv. Funct. Mater. **2003**, *13*, 698.

[30] Asakawa, K.; Hiraoka, T. *Jpn. J. Appl. Phys.* **2002**, *41*, 6112.

[31] Zalusky, A. S.; Olayo-Valles, R.; Taylor C. J.; Hillmyer, M. A. *J. Am. Chem. Soc.* **2001**, *123*, 1519.

[32] Ndoni, S.; Vigild, M. E.; Berg, R. H. Nanoporous Materials with Spherical and Gyroid Cavities Created by Quantitative Etching of Polydimethylsiloxane in Polystyrene−Polydimethylsiloxane Block Copolymers. *J. Am. Chem. Soc.* **2003**, *125* (44), 13366–13367.

[33] Schulte, L.; Grydgaard, A.; Jakobsen, M. R.; Szewczykowski, P. P.; Guo, F.; Vigild, M. E.; Berg, R. H.; Ndoni, S. Nanoporous Materials from Stable and Metastable Structures of 1,2-PB-*b*-PDMS Block Copolymers. *Polymer* **2011,** *52*, 422.

[34] Hillmyer, M. A. *Adv. Polym. Sci.* **2005**, *190*, 137.

[35] Mulder, M. Basic Principles of Membrane Technology, 2ed ed., Kluwer Academic, Netherlands **1996**.

[36] Ulbricht, M. Advanced Functional Polymer Membranes. *Polymer* **2006**, *47*, 2217–2262.

[37] Baker, R. W. Membrane Technology and Applications, 2nd ed., John Wiley& Sons, Ltd., Chichester, **2004**.

[38] Peinemann, K. V.; Nunes, S. P. Membrane Technology, Volume 1: Membranes for Life Sciences. Wiley-Vch, Weinheim, **2008**.

[39] Belfort,G.; Davis, R. H.; Zydney, A. L. The Behavior of Suspensions and Macromolecular Solutions in Crossflow Microfiltration, *J. Membr. Sci.* **1996**, *96*, 1–58.

[40] Nunes S, Peinemann KV, editors. Membrane Technology in the Chemical Industry. Weinheim: Wiley–VCH; 2001.

[41] Malhotra, B. D.; Singhal, R.; Chaubey, A.; Sharma, S. K.; Kumar, A. Recent Trends in Biosensors. *Current Applied Physics* **2005**, *5*, 92–97.

[42] Smah, A. J. and Anthony P. F. T. Recent Advances in Amperometric Glucose Biosensors for *in vivo* Monitoring. *Physial. Meas.* **1995**, *16,* 1–15.

[43] Wang, J. Electrochemical Glucose Biosensors *Chem. Rev.* **2008**, *108*, 814–825.

[44] Davies, M. L.; Hamilton, C. J.; Murphy, S. M. and Tighe, B. J. Polymer Membranes in Clinical Sensor Applications– An Overview of Membrane Function. *Biomaterials* **1992**, *13*, 14.

[45] Teles, F. R. R.; Fonseca, L. P. Applications of Polymers for Biomolecule Immobilization in Electrochemical Biosensors. *Materials Science and Engineering* **2008**, *28*, 1530–1543.

[46] Li, Q.; Luo, G.; Feng, J.; Zhou, Q.; Zhang, L. Amperometric Detection of Glucose with Glucose Oxidase Absorbed on Porous Nanocystalline TiO_2 film. *Electroanalysis* **2001**, *12*, 413–416.

[47] Joo, S.; Park, S.; Chung, T. D.; Kim, H. C. Integration of a Nanoporous Platinum Thin Film into a Microfluidic System for Non-Enzymatic Electrochemical Glucose Sensing. *Anal Sci* **2007**, *23*, 277–281.

[48] Gatimu, E. N.; Sweedler, J. V.; Bohn, P. W. Nanofluidics and the Role of Nanocapillary Array Membranes in Mass-Limited Chemical Analysis. *Analyst* **2006**, *131*, 705–709.

[49] Clark Jr., L.; Lyons, C. *Ann. NY Acad. Sci.* **1962**, *102*, 29.

[50] Guilbault, G. ; Lubrano, G. *Anal. Chim. Acta* **1973**, *64*, 439.

[51] Wang, J. Glucose Biosensors: 40 Years of Advances and Challenges. *Electroanalysis* **2001**, *13*, 983–988.

[52] Luong, J. H. T.; Male, K. B.; Glennon, J. D. Biosensor Technology: Technology Push versus Market Pull. *Biotechnology Advances* **2008**, *26*, 492–500.

[53] Wilson, G. S.; Gifford, R. *Biosens. Bioelectron.* **2005**, *20*, 2388.

[54] Hana, J. H.; Taylor, J. D.; Kima, D. S.; Kim, Y. S.; Kim, Y. T.; Cha, G. S.; Nama, H. Glucose Biosensor with a Hydrophilic Polyurethane (HPU) Blended with Polyvinyl Alcohol/vinyl Butyral Copolymer (PVAB) Outer Membrane. *Sensors and Actuators* **2007**, *123*, 384–390.

[55] Loeb, S.; Sourirajan, S. Patent Application Country: Application: US; Patent Country: US; Priority Application Country: US Patent 3133132, 1964.

[56] Loeb, S.; Sourirajan, S.; Weaver, D. E. Patent Application Country: Application: US; Patent Country: US; Priority Application Country: US Patent 3133137, 1964.

[57] Pinnau, I. and Koros, W. J. Structures and Gas Separation Properties of Asymmetric Polysulfone Membranes Made by Dry, Wet, and Dry/ Wet Phase Inversion. *J. App. Pol. Sci.* **1991**, *43*, 1491–1502.

[58] Smuleac, V.; Butterfield, D. A. and Bhattacharyya, D. Permeability and Separation Characteristics of Polypeptide-Functionalized Polycarbonate Track-Etched Membranes. *Chem. Mater.* **2004,** *16,* 2762-2771.

[59] Thormann, A.; Teuscher, N.; Pfannmçller, M.; Rothe, U. and Heilmann, A. Nanoporous Aluminum Oxide Membranes for Filtration and Biofunctionalization. Small **2007**, *3*, 1032 – 1040.

[60] Adiga, S. P.; Curtiss, L. A.; Elam, J. W. Nanoporous Materials for Biomedical Devices. *JOM* **2008**, 26–32.

[61] Yang, S. Y.; Ryu, I.; Kim, H. Y.; Kim, J. K.; Jang, S. K.; Russell, T. P. Nanoporous membranes with ultrahigh selectivity and flux for the filtration of viruses. *Adv. Mater.* **2006**, *18*, 709–712.

[62] Yang, S. Y.; Park, J.; Yoon, J.; Ree, M.; Jang, S. K. and Kim, J. K. Virus filtration membranes prepared from nanoporous block copolymers with good dimensional stability under high pressures and excellent solvent resistance. *Adv. Func. Mater.* **2008**, *18*, 1371–1377.

[63] Shannon, M. A.; Bohn, P. W.; Elimelech, M.; Georgiadis, J. G.; Marinas, B. J.; Mayes, A. M. Science and technology for water purification in the coming decades. *Nature* **2008**, *452*, 301.

[64] Phillip, W. A.; Rzayev, J.; Hillmyer, M. A.; Cussler, E. L. Gas and water liquid transport through nanoporous block copolymer membranes. *J. Membr. Sci.* **2006**, *286*, 144–152.

[65] Phillip, W. A.; O'Neill, B.; Rodwogin, M.; Hillmyer, M. A.; Cussler, E. L. Self-assembled block copolymer thin films as water filtration membranes. *Applied Materials & Interfaces* **2010**, *2*, 847–853.

[66] Guo, F.; Jankova, K.; Schulte, L.; Vigild, M. E.; Ndoni, S. One-Step Routes from Di- and Triblock Copolymer Precursors to Hydrophilic Nanoporous Poly(acrylic acid)-b-polystyrene. *Macromolecules* **2008**, *41*, 1486-1493.

[67] Berthold, A.; Sagar, K.; Ndoni, S. Manuscript in preparation.

[68]Sagar, K.; Christiansen, M. B.; Ndoni, S. Type and Distribution of Chemical Groups from Controlled Photo-Oxidation of Nanoporous 1, 2-Polybutadiene. *Polymer Chemistry* **2011.**

[69] Li, L.; Wang, Y.W.; Vigild, M. E. Ndoni, S. Physisorption of SDS in a Hydrocarbon Nanoporous Polymer. *Langmuir* **2010**, *26* (16), 13457–13465.

[70] Jackson, E. A. and Hillmyer, M. A. Nanoporous Membranes Derived from Block Copolymers: From Drug Delivery to Water Filtration. *ACS NANO* **2010**, *4* , 3548–3553.

[71] Stamatialis, D. F.; Papenburg, B. J.; Girones, M.; Saiful, S, Bettahalli, S.N.M.; Schmitmeier, S.; Wessling, M. Medical Applications of Membranes: Drug Delivery, Artificial Organs and Tissue Engineering. *J. Mem. Sci.* **2008**, *3*, 1–34.

[72] Siepmann, F.; Siepmann, J.; Walther, M.; MacRae, R. J.; Bodmeier, R. Polymer Blends for Controlled Release Coatings, *J. Controlled Release* **2008**, *125*, 1–15.

[73] Aminabhavi, T. M.; Kulkarini, R. V.; Kulkarini, A. R. Polymers in Drug Delivery. *Polymer News* **2004**, *29*, 214–218.

[74] Adiga, S. P.; Jin, C.; Curtiss, L. A.; Monteiro-Riviere, N. A. and Narayan, R. J. Nanoporous Membranes for Medical and Biological Applications. *Nanomed Nanobiotechnol* **2009**, *1*, 568–581.

[75] Desai, T. A.; Sharma, S.; Walczak, R. J.; Boiarski, A.; Cohen, M.; Shapiro, J.; West, T.; Melnik, K.; Cosentino, C.; Sinha, P.M.; Ferrari, M. Nanoporous Implants for Controlled Drug Delivery. In: Desai TA, Bhatia S eds. *BioMEMS and Biomedical Nanotechnology Volume III Therapeutic Micro/Nanotechnology*. New York: Springer, **2007**.

[76] Desai, T. A.; Chu, W. H.; Tu, J. K; Beattie, G. M.; Hayek, A. Microfabricated Immunoisolating Biocapsules. *Biotechnol Bioeng* **1998**, *57*, 118–120.

[77] Orosz, K. E.; Gupta, S.; Hassink, M.; Abdel-Rahman, M.; Moldovan, L. Delivery of Antiangiogenic and Antioxidant Drugs of Ophthalmic Interest through a Nanoporous Inorganic Filter. *Mol Vis* **2004**, *10*, 555–565.

[78] He, C. L.; Kim. S. W. ; Lee, D. Su. In Situ Gelling Stimuli-Sensitive Block Copolymer Hydrogels for Drug Delivery. *Journal of Controlled Release* **2008**, *127*, 189–207.

[79]Szewczykowski, P. Nano-porous Materials from Diblock Copolymers and Its Membrane Application, Ph.D. thesis, Technical University of Denmark, **2009**.

[80] Guo, F. Functional Nanoporous Polymers from Block Copolymer Precursors. Ph.D. thesis, Technical University of Denmark, **2010**.

Chapter 3 Preparation of Nanoporous 1,2-PB Membranes

During the overall Ph.D. project, all the membranes were prepared with the same material, e.g. 1,2-polybutadiene-*b*-polydimetylsiloxane (1,2-PB-*b*-PDMS). This chapter will detail how nanoporous 1,2-PB membranes were prepared from the 1,2-PB-*b*-PDMS precursors in the thesis work. The extensive characterization results and discussion will be saved for the next chapter. These nanoporous membranes will be in detail explored for different membrane applications as reported in chapter 6, 7 and 8.

Figure 3.1 illustrates the preparation procedures in general terms without focusing on specific formulations. The general procedure is the same for all the membrane samples used in this work. It consists of four main steps:

- Design and synthesis of block copolymer precursors — a specific nanostructure (e.g. LAM, HEX, GYR, etc.) is determined at this step.[1]
- Thermally cross-linking the precursor — the mechanical properties of the resultant nanoporous material are mainly controlled at this step;[2] surface morphology can also be defined at this step.[3]
- Selectively etching the cross-linked precursor to remove one block — a nanoporous matrix is created at this step; different intrinsic bulk porosity can be derived depending on the etching conditions.
- Surface functionalization of nanoporous matrices — different surface modification techniques can be used to produce proper surface properties for a particular application. [0]

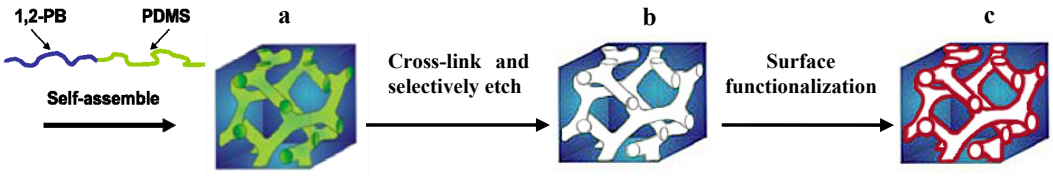

Figure 3.1 Schematic illustration of the fabrication of cross-linked nanoporous 1,2-PB polymer from 1,2-PB-*b*-PDMS block copolymer. The precursor 1,2-PB-*b*-PDMS self-assembles into gyroid morphology at the cross-linking temperature (a). PDMS is selectively cleaved from the sample and a nanoporous

polymer matrix is obtained (b). According to a specific demand from some application, the nanoporous polymer matrix can be further modified via various surface functionalization approaches (c).

3.1. Block copolymers

Different batches of 1,2-PB-*b*-PDMS copolymers were used as templates for fabricating the nanoporous membranes studied in the thesis work. All the 1,2-PB-*b*-PDMS copolymer samples were produced by Lars Schulte using living anionic polymerization as reported by Ndoni et al.[8] The detail description of synthesis is out of scope of this thesis and can be found in refs 1 and 8. The overall molecular weight (number-average molecular weight $<M_n>$), mass fraction w_{PDMS}, and polydispersity index PDI were determined by a combination of ^{1}H-NMR and size exclusion chromatography, as summarized in Table 3.1. [1] Small angle X-ray scattering (SAXS) was used to confirm the formation of gyroid morphology in all the samples (not presented in the thesis). [1,8] Gyroid is a bicontinuous cubic structure with $Ia\bar{3}d$ symmetry.[9] The space of the minority component in gyroid structure is divided into two interpenetrating equally sized volumes. The tripods are connected by twisting the planes with respect to each other by an angle of 70.53° (Fig. 3.1).[9] Gyroid morphology was designed from synthesis stage and used through the entire project, because it requires no need for structure alignment for any membrane applications.

Table 3.1 Basic properties of block copolymer samples having gyroid morphology[a], w_{PDMS} = 0.41[b] and f_{PDMS} = 0.39[c].

Sample	$<M_n>_{PB}$ (g/mol)[d]	$<M_n>_{total}$ (g/mol)[e]	PDI[f]	Usage
BD14	8400	14200	1.04	Chapter 8
BD36	7228	12250	1.16	Chapter 5,6, 7

[a.] morphology determined by SAXS.

[b.] mass fraction of PDMS determined by ^{1}H-NMR.

[c.] volume fraction of PDMS at 20°C; density values: $\rho_{1,2\text{-PB}}$ = 0.902 g/cm^3 and ρ_{PDMS} = 0.966 g/cm^3. [10,11]

[d.] Number average molecular weight of the 1,2-PB block as obtained by SEC.

[e.] Number average molecular weight obtained by SEC and ^{1}H-NMR.

[f.] Polydispersity index PDI = $<M_w>/<M_n>$ ($<M_w>$ is the weight average molecular weight) obtained by SEC.

3.2. Membrane preparation and fabrication

Cross-linking of 1,2-PB Dicumyl peroxide (bis(*α,α*-dimethylbenzyl) peroxide) (DCP, Merck) was used as received for cross-linking 1,2-PB in the precursor 1,2-PB-*b*-PDMS. 1 % mole DCP relative to the molar amount of double bonds in 1,2-PB was dissolved in tetrahydrofuran (THF, Sigma-Aldrich) solutions of 1,2-PB-*b*-PDMS prior to solution casting. Two casting methods were used to respectively fabricate thick samples (~ 500 μm) and thin samples (< 150 μm), as schematically illustrated in Figure 3.2. For fabricating a thick membrane, the sample solution was cast onto a glass petri-dish, and dried under nitrogen flow at room temperature. After overnight drying, the optically transparent films experienced cross-linking in a preheated thermostated oven at 140 °C for 2 hours under nitrogen atmosphere. The cross-linking reaction happened thus with one side of the film exposed to the atmosphere and the other in contact with glass. For comparison, one 1,2-PB-*b*-PDMS sample was cross-linked sandwiched between two glass petri-dishes, thereby eliminating the free surface. Spacers (500 μm in thickness) were placed at the edge of the petri-dish in order to control the thickness of the polymer film.

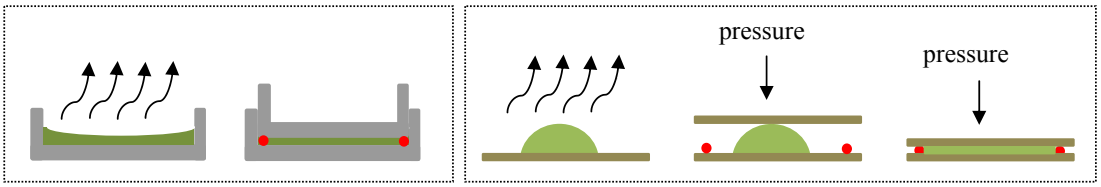

Figure 3.2 Schematic illustration of solvent casting of the precursor solutions (green) onto a petri-dish (grey) for preparation of thick membranes (left) and onto a flat plate (glass or FTDS-coated glass, dark yellow) for preparation of thin membranes (right). Spacers (red) with a desired thickness were used for membrane thickness control.

Various approaches were tried to form a thin film at the start of the thesis work. Here we only present the successful method i.e. sandwich method; the others that are to some extent failure will be reported in Appendix A. For the sandwich method, two sets of substrates were used for casting the precursor film. One is a glass plate; the other is a FDTS-coated glass plate via molecular vapor deposition.[12] FDTS stands for $Cl_3Si(CH_2)_2(CF_2)_7CF_3$. The sample solution was cast onto a clean substrate (glass or FDTS coated glass), followed by evaporating under nitrogen flow first and then drying in a vacuum at room temperature. The dried sample was covered with a second plate (glass or FDTS-coated glass). The two plates were squeezed together under 4 bars

at room temperature with a homemade pneumatic-drive compressing set-up under vacuum for 2 hrs. The thickness of the sample was controlled with a few pieces of 0.5 cm wide aluminum spacers with a desired thickness. The sandwiched block copolymer samples were cross-linked at 140 °C for 2 hours under nitrogen atmosphere. We expect the membrane prepared between two glass plates would show 'open' porous outer surface while the membrane prepared between two FDTS-coated plates would show a 'closed' skin layer near the surface (To be explained in chapter 4.2.2). For the sake of convenience, membranes prepared between two glasses are referred to in this thesis as non-skin (*ns*) membranes to denote a porous surface, while membranes prepared between fluorinated glasses are referred to as double-skin (*ds*) membranes to denote a dense top layer on the membranes prepared.

Etching of PDMS As described elsewhere[1], the general procedure for etching 500–1000 μm thick samples is as follows. Tetrabutylamonium fluoride (TBAF) (Aldrich) was used as etching reagent to selectively remove PDMS. Cross-linked samples were reacted for 36 h with 1 M TBAF in THF at 2 molar excess amounts relative to the concentration of repeating unit $-\overset{|}{\underset{|}{\text{Si}}}-\text{O}-$ in PDMS[1]. After etching, each sample was taken out of the solution and rinsed in mixtures with varying ratio (v/v) of THF/Methanol. Solvent evaporation followed under a Nitrogen flow. Besides the thick samples, we also made effort to prepare thin nanoporous membranes e.g. 20 μm by optimizing the etching formulations, e.g. TBAF concentration $[TBAF]_0$, molar ratio of TBAF and $-\overset{|}{\underset{|}{\text{Si}}}-\text{O}-$ (m_{TBAF} / m_{Si-O}), and etching time t (See the detailed results and discussion in Appendix B). Finally, we used a formulation of $[TBAF]_0$ =0.005 M, m_{TBAF} / m_{Si-O} = 1 (mol/mol) and the excess time 5h for etching the thin membranes with thickness below 100 μm. In the entire thesis work, a complete etching was performed to obtain samples with the maximum porosity, i.e. 0.39. For a particular interest, a batch of samples with different porosities were prepared for investigating the effect of intrinsic porosity on diffusive transport in membranes as presented in Appendix B.

3.3. Surface modification

Nanoporous 1,2-PB membranes are naturally hydrophobic. Aqueous solution can not spontaneously infiltrate the membranes by capillary force. Extensive work in relation to surface functionalization of nanoporous 1,2-PB membranes has been reported by pre-Ph.D. student Fengxiao Guo in our group.[13] Three different methods were used in the thesis work to render the membrane surface hydrophilic to some extent.

SDS physisorbtion It is a simple and low-cost physical modification[14]. Sodium dodecyl sulfate (purity 98.5%, Sigma-Aldrich) was used as received. We prepared SDS solutions in deionized (DI) water and stirred on a shaker at room temperature for at least 15 h before use. Molar concentrations in the range 0.5 – 50 mM were used for the SDS loading experiments. In the SDS loading experiment, each piece of nanoporous 1,2-PB film (20 ± 1 mg) was placed in 15 mL of SDS aqueous solution and kept under shaking at planned time intervals. The solution loading rates for different SDS concentrations were followed by gravimetry. Each sample was taken out of the solution, gently wiped with a tissue, immediately weighed in a balance with precision 0.1 mg, and placed back to the solution for the next time interval. At the end of the loading experiment, the outer surface of the sample was wiped with a tissue and dried under nitrogen flow without further treatment. The mass of the SDS-loaded film was notified after complete drying. See details in chapter 8.

UV photooxidation We first reported the initial findings of UV photooxidation of nanoporous 1,2-PB matrices[15] and an extensive work on photooxidation mechanism was investigated by Ph.D. student Kaushal Sagar in our group.[6] For comparison in diffusion properties (See chapter 6), a batch of original nanoporous 1,2-PB membranes were functionalized via UV photooxidation. 20 μm NP films were photooxidized in air at 37 ºC up to 12 h by UV generated from Philips Cleo 25W RS UV lamps. The radiation wavelength range was 310 – 420 nm, peaking at 350 nm; the UV intensity is in the range of 14 – 16 mW/cm^2. The UV irradiation 'hits' the samples from the top side. Simple masks were made on paper sheets and used for controlling the exposure area to UV.

UV-induced thiolene chemistry Pre-Ph.D. student Anton Berthold[7] in our group first developed this technique for surface functionalization of nanoporous 1,2-PB membranes, and an expanding investigations were further conducted by Kaushal Sagar[16]. For comparison of the ultrafiltration

properties (See chapter 7), a batch of original nanoporous 1,2-PB membranes were functionalized via UV-initiated thoil-ene chemistry. The surface hydrophilization was performed with 500 mM MESNA (sodium 2-sulfanylethanesulfonate, Sigmaaldrich) solutions in ultrapure water mixed with equal volume of 10 mM photoinitiator DMPA (2,2-Dimethoxy-2-phenylacetophenone, Sigma-Aldrich) solution in DMF (N,N-dimethylmethanamide, Sigma-Aldrich).

A 9 cm long UVA-lamp (SolData, Denmark) with a main peak at 365 nm and emission range 315 nm –400 nm was used for the photo-grafting. The membranes were immersed in the grafting solution in a 20 ml Al-wrapped glass bottle for 1 hour preloading. Subsequently, the samples were taken out and placed between two glass plates. The samples were irradiated for 10 min at a constant intensity of 8 mW/cm^2 measured with an UVA power meter from SolData.

After the pore surface modification, the samples were cleaned in large excess of ethanol and water followed by drying under N_2 flow. The pore surface was expected to be grafted with sulfonated groups of average surface density 1.6 groups/ nm^2. The relevant characterizations, e.g. gravimety, FTIR and water uptake were performed to evaluate the extent of the hydrophilization, as reported in detail elsewhere[7].

3.4. Summary

Table 3.2 A list of membrane samples used in the thesis work.

Membrane	Thickness (μm)	Surface morphology		Surface modification	Application	Chapter
		Non-skin[a]	Skin[a]			
1	20 ~ 150	Yes	Yes	UV photooxidation	Dialysis	6
2	20 ~ 30	Yes	No	Thiolene chemisty	Ultrafiltration	7
3	500	Yes	Yes	SDS physisorbtion	Release	8

[a.] 'Non-skin' denotes a porous surface without a top dense layer on the membranes prepared; 'Skin' denotes a dense top layer so called skin layer on the membranes prepared. See the details in Chapter 4.

The goal of this thesis is to explore the potential of nanoporous 1,2-PB in membrane applications involving dialysis, ultrafiltration, and sustained release. We prepared a series of nanoporous 1,2-PB membranes with different membrane characteristics, hence different

membrane properties and performance would be expected. Table 3.2 summarizes some basic characteristics of the membrane samples used in the work presented in the following chapters.

3.5. References

[1] Schulte, L.; Grydgaard, A.; Jakobsen, M. R.; Szewczykowski, P. P.; Guo, F.; Vigild, M. E.; Berg, R. H.; Ndoni, S. Nanoporous Materials from Stable and Metastable Structures of 1,2-PB-*b*-PDMS Block Copolymers. *Polymer* **2011,** *52*, 422.

[2] Guo, F.; Andreasen, J. W.; Vigild, M. E.; Ndoni, S. Influence of 1,2-PB matrix cross-linking on structure and properties of selectively etched 1,2-PB-b-PDMS block copolymers. *Macromolecules* **2007**, *40*(10), 3669-3675.

[3] Li, L.; Schulte, L.; Clausen, L. D.; Hansen, K. M.; Jonsson, G. E.; Ndoni, S. Gyroid Nanoporous Membranes with Tunable Permeability. *ACS Nano* **2011**, *5* (10), 7754 – 7766.

[4] Guo, F.; Jankova, A. K.; Schulte, L.; Vigild, M. E.; Ndoni, S. Surface Modification of Nanoporous 1,2-Polybutadiene by Atom Transfer Radical Polymerization or Click Chemistry. *Langmuir* **2010**, *26*, 2008-2013.

[5]Guo, F.; Jankova, A. K.; Vigild, M. E.; Ndoni, S. Hydrophilic Nanoporous 1,2-Polybutadiene via Surface-Initiated Atom Transfer Radical Polymerisation. *Polymer Preprints* **2008**, *49*, 540-541,

[6] Sagar, K.; Christiansen, M. B.; Ndoni, S. Type and Distribution of Chemical Groups from Controlled Photo-Oxidation of Nanoporous 1, 2-Polybutadiene. *Polymer Chemistry* **2011.**

[7] Berthold, A.; Sagar, K.; Ndoni, S. Manuscript in preparation.

[8] Ndoni, S.; Vigild, M. E.; Berg, R. H. Nanoporous Materials with Spherical and Gyroid Cavities Created by Quantitative Etching of Polydimethylsiloxane in Polystyrene−Polydimethylsiloxane Block Copolymers. *J. Am. Chem. Soc.* **2003**, *125* (44), 13366–13367.

[9] Vigild., M. E.; Almdal, K.; Mortensen, K. *Macromolecules* **1998**, *31*, 5702-5716.

[10] Mark, J. E. editor, Polymer Data Handbook, Oxford University Press, 1999.

[11] Brandrup, J.; Immergut, E. H. Polymer Handbook, 3rd ed., John Wiley & Sons: New York, 1989.

[12] Szewczykowski, P. Nano-porous Materials from Diblock Copolymers and Its Membrane Application, Ph.D. thesis, Technical University of Denmark, **2009**.

[13] Guo, F. Functional Nanoporous Polymers from Block Copolymer Precursors. Ph.D. thesis, Technical University of Denmark, **2010**.

[14] Li, L.; Wang, Y.W.; Vigild, M. E. Ndoni, S. Physisorption of SDS in a Hydrocarbon Nanoporous Polymer. *Langmuir* **2010**, *26* (16), 13457–13465

[15] Ndoni, S.; Li L.; Schulte, L.; Szewczykowski, P. P.; Hansen, T. W.; Guo, F. X.; Berg, R. H.; Vigild, M. E. Controlled Photooxidation of Nanoporous Polymers *Macromolecules*, **2009**, *42*, 3877–3880.

Chapter 4 Structural Characteristics of Nanoporous 1,2-PB Membranes

Structural parameters such as morphology, pore size and distribution, porosity, thickness, and etc. are crucially important in determining intrinsic properties of a given membrane and are associated with final membrane performance. It is necessary to comprehensively characterize a newly developed membrane prior to any other actions. For the nanoporous 1,2-PB membranes derived from 1,2-PB-*b*-PDMS copolymers, a well-defined recipe has been developed in previously work and followed as it is in the thesis work. Fourier transformed infrared (FTIR) spectroscopic data confirmed cross-linking degree and etching efficiency[1]. In most cases, highly cross-linked nanoporous 1,2-PB matrices with complete removal of PDMS components were prepared; if not the case, a particular emphasis will be given. The porosity of the resultant membranes is checked by gravimetry and water uptake (max. 0.79 cm^3 per gram), which can directly reflect the PDMS etching efficiency. Small angle x-ray scattering (SAXS) demonstrates gyroid morphology in both precursors and nanoporous films with 15 nm in pore diameter.[2, 3] N_2 adsorption data revealed a continuous porous structure with a narrow pore distribution, interior surface area of 278 ± 40 m^2/g and pore diameter of 15 nm.[2, 3] This chapter will present Scanning electron microscopy (SEM), Transmission electron microscopy (TEM) and Atomic force microscopy (AFM) images to show structural characteristics of the nanoporous membranes used in the thesis work. A detailed discussion will be given to the formation of surface morphology caused by different substrates. The complementary X-ray photoelectron spectroscopy (XPS) and Contact angle measurements (CA) data provide supporting information for the proposed structure concluded from electron microscopy.

4.1. Experimental

Scanning electron microscopy (SEM) was done on a HELIOS instrument or a Quantum FEGSEM instrument from FEI using an acceleration voltage of 5 kV. The samples were sputter-coated with 2 nm thick Pt/Pd prior to SEM imaging. Top surface and fracture surface were

examined by SEM. If needed, the fracture surface could be trimmed flat and further microtomed on a Leica ultramicrotome with a cryo 35º diamond knife (DIATOME) at room temperature.

Atomic force microscopy (AFM) was performed at ambient conditions using NanoMan AFM in tapping mode, with NANOSENSORS™ SSS-NCH AFM probe. The scan area was 1 μm x 1 μm, and 512 x 512 pixels. The fracture surface was trimmed flat and further microtomed on a Leica ultramicrotome with a cryo 35º diamond knife (DIATOME) at room temperature. The sample was glued on a silicon plate and the microtomed surface faced up for tip scanning.

Transmission electron microscopy (TEM) was performed on a FEI TECNAI T20 at acceleration voltage of 200 kV. Nanoporous films were sectioned into 90 nm slices on a Leica ultramicrotome with a cryo 35º diamond knife (DIATOME) at room temperature. The slices were deposited onto a holey carbon copper grid for TEM measurements.

Contact angle measurements (CA) and ***surface tension measurements*** were conducted on a Contact Angle System OCA 20. Contact angles of water, ethylene glycol, and diiodomethane on a glass plate or a FDTS-coated glass plate (See chapter 3.2) were measured at room temperature with the sessile drop method.[4] The contact angles of two polymer melts on these two substrates were measured at 140 ºC. We used drop-pendant method[4] to estimate the surface tension of homopolymer melts at 140 ºC.

X-ray photoelectron spectroscopy (XPS) was recorded on a Surface Science Instruments Sage-100 with a monochromated Al Kα X-ray at take-off angle of 90 degree. Elements present on the surface were identified from a survey spectrum over the energy range 0 – 1400 eV with pass energy of 100 eV and resolution of 0.5 eV. The spectrum was analyzed with the software Avantage provided by the manufacturer.

4.2. Results and discussion

4.2.1. Bulk morphology

Figure 4.1 shows typical nanoporous 1,2-PB membranes prepared in this study, having thickness of 500 μm and 20 μm, respectively. The membranes are colorless and transparent regardless of thickness. The thin membrane shows higher flexibility relative to the thick sample

which is stiff and brittle. The bulk morphology of membranes was visualized by SEM, AFM and TEM as shown in Figures 4.2[5,6] and 4.3. [7]

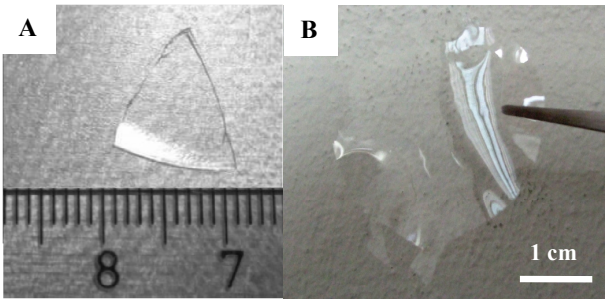

Figure 4.1 Photographs of cut pieces of nanoporous films with thickness of 500 μm (A) and 20 μm (B).

Figure 4.2 gives the representative SEM image (Fig. 4.2 A) and AFM image (Fig. 4.2 B), showing gyroid morphology of the nanoporosity in the bulk of the 1,2-PB membranes. We observed a typical projection, knitting view in both images. The micrographs reveal a characteristic topological feature of the regularly spaced nanochannels with diameter of ~10 nm, related to the PDMS microdomain size. The diameter of a knitting thread is ~15 nm, corresponding to the 1,2-PB microdomain dimension. A narrow distribution in pore sizes visible in the image of the fracture surface is due to the bicontinous nature of the material. If we cut across a pore at an angle other than perpendicular then the pore will appear to be larger than it acutrally is. Both SEM and AFM micrographs of the fracture cross section demonstrate that the pore structure is homogeneous along the length of the membrane. It is worth mentioning that SEM and AFM both are the common techniques that provide information of the surface features of samples. However, they have respective advantages and disadvantages. For example, SEM may provide pore size less than the real size due to enrichment of the sputter coating atoms at the entry of pores[8] while AFM may show the artifacts gained in the measurement due to quality of the tip used, flatness and stability of the sample measured, etc.[9] Therefore we used both techniques to characterize the membranes. Similar results were obtained in this case. Most importantly, we also took unique advantage of AFM measurement, allowing the reuse of the samples. In chapter 6, all the membranes were first characterized by AFM and then evaluated in diffusion tests; therefore we can directly correlate the surface morphology with diffusive permeability.

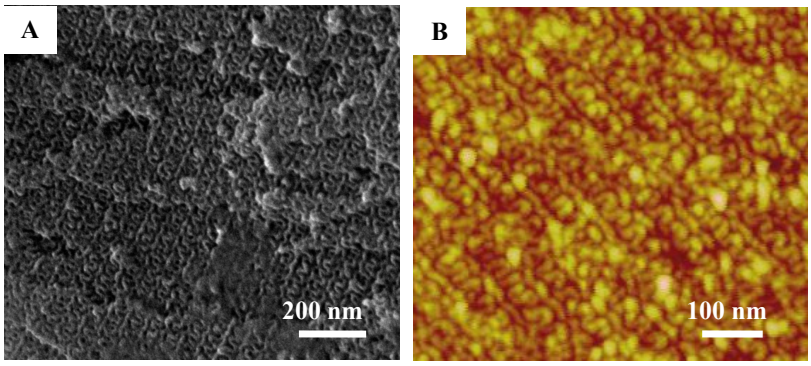

Figure 4.2 A cross-section of nanoporous 1,2-PB membrane showing the 'knitting' projection (211) of gyroid morphology; **A**: SEM image;[5] **B:** AFM image.[6]

Figure 4.3 displays TEM images of three typical projections of gyroid morphology in the bulk of the membrane, wagon wheel projection [111] (Fig 4.3 A), wishbone projection [311] (Fig 4.3 B) and [211] projection (Fig 4.3 C). All the TEM images present regular patterns with uniform pore size of ~ 10 nm (bright) in the 1,2-PB bulk (dark), identical to the dimension of the feature seen in the SEM and AFM images.

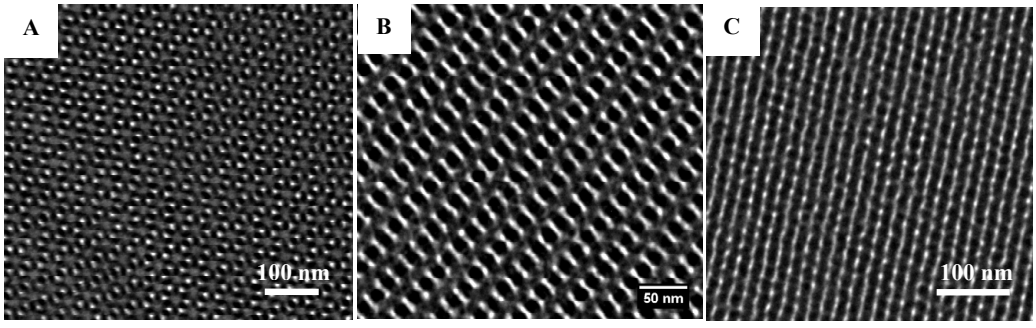

Figure 4.3 TEM micrographs of an ultrathin section of nanoporous membrane showing three different projections of gyroid morphology A: the 'wagon-wheel' projection [111]; B. the 'wishbone' projection [311]; C. the [211] projection.[7]

4.2.2. Surface morphology

Much attention has been given in the last decades to the study of microphase separation in block copolymers, since it is one of the most important factors imparting the physical and mechanical properties unique to these systems. On the other hand, a great interest has been generated in surface behavior of block copolymers, since surface is of critical importance in many applications. A large amount of theoretical and experimental work has shown that the surface may differ from the bulk in chemical composition and morphology.[10] In thermodynamic equilibrium, such block copolymer samples are generally terminated by a thin layer of the lower surface energy block on the free surface and, therefore, exhibit a chemically homogeneous surface. [11,12] The following results and discussion have been reported in the manuscript *Gyroid Nanoporous Membranes with Tunable Permeability* published in *ACS Nano2011*.[6]

As we described in chapter 3.2, a 500 μm thick membrane was prepared by casting onto a glass petri-dish under N_2. During cross-linking, as the temperature increases from 20 ºC to 140 ºC the microphase in the film bulk (far away from the surface) is expected to transform from lamellar (LAM) to gyroid (GYR) passing through the metastable hexagonally perforated layer morphology (HPL).[2] LAM is the stable structure at room temperature and GYR at 140 ºC. Therefore a gyroid structure was captured in the film bulk after cross-linking as shown in Figs. 4.2 and 4.3. However, the outer surface morphology of the block copolymer film is dependent on the interfacial energy between polymer and selected substrate. The SEM image in Figure 4.4 A shows two distinct regions in the cross section near the free surface of the nanoporous film, a dense thin layer, approximately 30 nm as highlighted by red lines and a uniform pattern of GYR nanostructure beneath. This suggests that a dense skin layer may form on the polymer/nitrogen interface (during cross-linking) of the nanoporous film. A top view of the free surface is further visualized in Figure 4.4 B showing no visible pores at the surface. Figure 4.4 C shows a top view of the edge at the free surface. A piece of 'skin' with the same closed surface as seen in Figure 4.4 B is partially peeled off from the surface. The surface beneath displays characteristic feature of HPL morphology, which is the transient morphology between LAM and GYR.[2] The periods of both LAM and HPL for a 1,2-PB-*b*-PDMS sample similar to the precursor of this study are ~21 nm as determined by SAXS. [2] Therefore the observed average skin layer thickness is equal to 1.5 periods of HPL (32 nm), or to one PB lamella and one period of HPL (34 nm). [2] In short,

this phenomenon is probably due to stabilization at this interface of a lamellae morphology driven by PDMS coverage of the top surface to minimize nitrogen-polymer interfacial energy.

In contrast, we observed a porous surface formed at the polymer/glass interface showing a surface porosity of 40 ± 5% as estimated by image analysis of SEM pictures (Figure 4.4 D). As mentioned in chapter 3.2, one sample, for comparison, was cross-linked sandwiched between two glass pertri-dishes (again referring to cross-linking), presenting a similar pattern as seen in Fig. 4.4 D; no skin layer was observed for the surface in contact with glass.

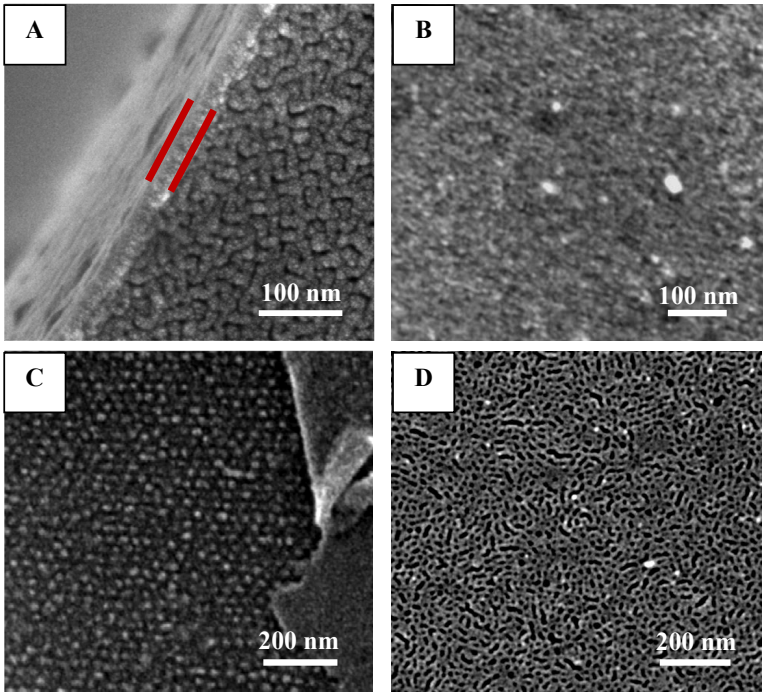

Figure 4.4 SEM images of a 500 μm nanoporous film prepared by solvent casting onto a glass petri-dish: (A) cross-section near the free surface; (B) the surface resulted from polymer/air interface during the cross-linking; (C) the edge of surface resulted from polymer/air interface during the cross-linking; a over-flipped skin layer was observed, and a bumpy structure beneath the skin-layer; (D) the surface resulted from polymer/glass interface during the cross-linking.

In order to have an in-depth understanding of the observations and have an ability to selectively control the surface behavior as expected, we decided to better define the interface

environment. We used two different substrates, a glass plate and a FTDS-coated glass plate (here we also called fluorinated plate; See chapter 3.2), to cast 1,2-PB-*b*-PDMS polymer solutions, thus creating a distinct interfacial environment for the block copolymer films as-casted.

Similar to the free surface shown in Fig. 4.4 B, the FDTS-coated substrate produced a flat dense surface with no discernible pores (Figure 4.5 A). Figure 4.5 B shows a top view of the edge of the membrane prepared between the fluorinated substrates. Again we observed the surfaces beneath showing a typical projection of HPL morphology, consistent with that displayed in Fig. 4.4 C. As discussed above, this may indicate that the skin layer consists of sublayers instead of a single uniform layer, the outmost layer being LAM on the outer side and HPL on the inner side, followed by at least one additional HPL layer.

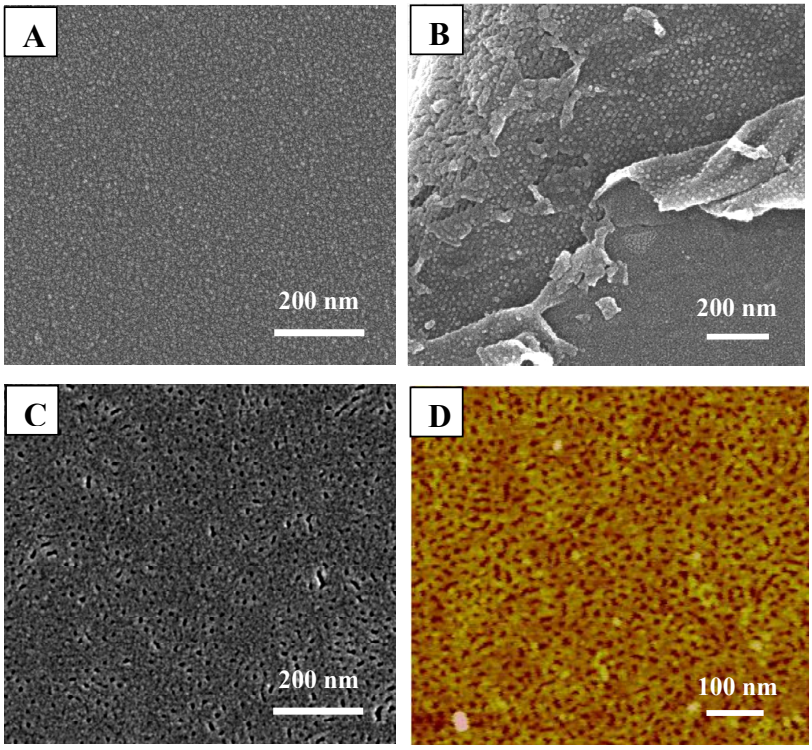

Figure 4.5 SEM images of nanoporous membranes prepared between two plates: (A) surface in contact with fluorinated-glass; (B) top view of the edge of a nanoporous membrane prepared between fluorinated-glass plates; (C) surface in contact with glass, and (D) an AFM image of the same surface as Fig. 4.5C.

Figures 4.5 C and 4.5 D compare SEM and AFM images of the surface prepared between a pair of glass plates. The surface in contact with the glass shows randomly-distributed nanoporosity, having a pore size of ~ 10 nm and a surface porosity of 35 ± 5 % as estimated by image analysis of SEM images and 40 ± 5 % from AFM images. The average lower porosity from SEM images might be attributed to pore narrowing by the sputter-coating layer and worse image contrast. It is interesting to note that both glass petri-dish (Fig. 4.4 D) and glass plate (Fig. 4.5 C) resulted in a porous surface but different appearance. We are unable at this stage to give any reasonable explanation.

In the following section, we focus on the samples prepared between the two plates. For the sake of convenience, membranes prepared between two glasses are referred to hereafter as non-skin (*ns*) membranes, while membranes prepared between fluorinated glasses (i.e. FDTS-coated glasses) are referred to as double-skin (*ds*) membranes. Single-skin (*ss*) membranes are prepared between one fluorinated glass and one glass. Microscope images were supplemented by advancing contact angle (CA) measurements and XPS data on the surfaces of skin and non-skin membranes before and after PDMS removal. The experimental data are summarized in the first row of Tables 4.1 and 4.2.

Table 4.1 Experimental and predicted values of advancing contact angle of water on the surface of double-skin and non-skin samples before and after PDMS removal with uncertainties as subscripts.

	Non-skin		Double-skin		PDMS	1,2-PB-H[d]
	BD36-X-*ns*[d]	BD36-E-*ns*[d]	BD36-X-*ds*[d]	BD36-E-*ds*[d]		
θ_{exp}[a] (°)	$91.1_{3.5}$	$107.1_{9.7}$	$105.6_{0.6}$	$93.3_{4.1}$	106_{6} [c]	$91.0_{0.8}$
θ_{cal}[b] (°)	$91.0_{0.8}$ or $96.9_{2.3}$	$114.2_{3.0}$	106_{6}	$91.0_{0.8}$	-	-

[a.] Experimental values of advancing contact angle of water;
[b.] Calculated values of water contact angle based on the observations from SEM, using equation 4-1;
[c.] Value of water contact angle on PDMS surface reported in reference 13.
[d.] BD36-X-ns: cross-linked non-skin; BD36-E-ns: etched non-skin; BD36-X-ds: cross-linked double skin; BD36-E-ds: etched double skin samples; 1,2-PB-H: cross-linked 1,2-PB homopolymer.

The CA value for the cross-linked double-skin membranes BD36-X-*ds* is similar to the reported value[13] for pure PDMS; while for the etched sample BD36-E-*ds* the CA value is close to that of the cross-linked 1,2-PB homopolymer (1,2-PB-H). Most likely only PDMS block segregates on the outmost surface of the BD36-X-*ds* sample; accordingly a 1,2-PB layer fully covers the outmost surface of the BD36-E-*ds* sample after PDMS removal. For the *ns*

membranes, the water contact angle increased from the cross linked sample BD36-X-*ns* to the etched sample BD36-E-*ns*. This might be due to the porous surface (Fig. 4.5 D) of the etched sample where air-filled nanopores lower the surface energy. We compared the obtained CA values with predictions by Cassie's equation,[14] using the information of surface porosity from the AFM images (See Fig 4.5 D).

$$\cos\theta_p = f_A \cos\theta_A + f_B \cos\theta_B \qquad (4\text{-}1)$$

where θ_p is the water contact angle of the surface made of A and B. f_A and f_B are surface fractions of component A and B, respectively. In our case, A is 1,2-PB; B is PDMS for the cross-linked samples or air for the etched samples. The calculated values are given in the second row of Table 4.1. For the BD36-X-*ns* sample, there are two possibilities, either (1) the outmost surface is covered by a layer of pure 1,2-PB, then the calculated CA value is 91.0º; or (2) a CA value of 96.9 ± 2.3 º can be calculated assuming coexistence of 1,2-PB and PDMS on the surface with the same concentration of PDMS as the surface porosity of the etched sample (40 ± 5 % PDMS). XPS analysis favors this latter scenario (to be addressed later). It's also possible that some slight surface oxidation is present on the outermost PB layer, which may lower the contact angle of PB, accidentally lowering the overall contact angle close to that of pure 1,2-PB. After PDMS removal, the BD36-E-*ns* sample shows a porous surface with surface porosity of 40 ± 5 % consistent with a calculated CA value of 114.2 ± 3.0º.

For the BD36-X-*ds* sample, the observed value is consistent with a surface fully covered by PDMS (106º) [13]. The enrichment of PDMS on the surface in contact with fluorinated glass is driven by minimization of interfacial energy. A CA value of 91º, equal to that of pure 1,2-PB, is predicted for the BD36-E-*ds* sample based on the non porous surface revealed by the SEM image in Fig. 4.5 A combined with the quantitative removal of PDMS in the etching process.

The surface composition of the skin and non-skin samples was further assessed by XPS measurements. The surface composition was studied by XPS analyses at takeoff angle of 90° on skin and non-skin samples before and after PDMS removal. The results on the atomic abundance of C and Si in the skin and non-skin samples are summarized in Table 4.2.

First, all the etched samples show Si concentrations close to zero, consistent with the complete removal of PDMS. The cross-linked non-skin sample show Si/C atomic ratio of 10.1%, close to the ratio of 9.9% predicted for the cross-linked sample with a surface composition equal to that

of the bulk. Accordingly the surface porosity of the etched non-skin sample should be similar to bulk porosity, which is actually consistent to the observed porosity from the AFM images.

Table 4.2 XPS data of the surfaces of skin and non-skin samples before and after etching.

	C (1s) %	Si (2p) %	Si / C %	Calc. Si/C %
BD36-X-ns	79.6	8.1	10.1	9.9
BD36-E-ns	97.7	0.3	0.3	0.2[a]
BD36-X-ds	74.3	11.4	15.3	15.4[b]
BD36-E-ds	95.6	0.6	0.6	0.2[a]

[a] Si directly connected to the 1,2-PB block (C-Si bond) is expected to resist etching, which breaks only Si-O bonds.
[b] This value is calculated for a 4 nm thick PDMS lamella on top of a 13 nm 1,2-PB lamella assuming exponential decay of electron escape on sample depth and a penetration depth of 5 nm.

A Si/C atomic ratio of 15.3% was detected on the surface of the cross-linked skin sample, showing a surface enriched with PDMS relative to the non-skin sample. As suggested by the results of contact angle measurements, the PDMS block is expected to fully cover the outmost surface of the cross-linked skin sample. The period of LAM for the precursor 1,2-PB-*b*-PDMS is ~ 21 nm as determined by SAXS[4.4] then a monolayer of PDMS is expected to be ~ 4 nm thick. A value close to the observed value is calculated for a 4 nm thick PDMS lamella on top of a 13 nm 1,2-PB lamella as schematically illustrated in Figure 4.6. Here we assume exponential decay of electron escape on sample depth with penetration depth of 5 nm.

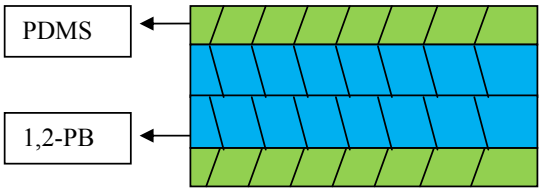

Figure 4.6 A schematic drawing illustrating the surface composition distribution near the surface.

In order to better understand the formation of the surface morphology, the interface energies between homopolymer melt (PMDS or 1,2-PB) and the substrate (glass or FDTS-coated glass) were examined. We used drop-pendant method to estimate the surface tension of homopolymer

melts at 140 ºC and water, methylene iodide and ethylene glycol were further employed to measure the surface energy of two substrates at room temperature. The contact angles of two polymer melts on these two substrates were also measured at 140 ºC. The experimental data are listed in Table 4.3. The $\Delta\gamma_{\text{polymer/glass}}$ or $\Delta\gamma_{\text{polymer/FTDS}}$ was calculated from Young's equation[15] as given in Table 4.3. As expected, the surface energy of the glass is significantly higher than that of PDMS or 1,2-PB homopolymers, while the fluorinated surface shows a value very close to PDMS. The values of $\Delta\gamma_{1,2-PB/substrate}$ and $\Delta\gamma_{PDMS/substrate}$ relative to the same substrate are very close, however, the γ_{Glass} is much higher than γ_{FDTS}. Hence, the glass substrate showed relative neutrality toward the 1,2-PB-*b*-PDMS copolymer, while the fluorinated glass exhibited higher selectivity towards the PDMS block.

Table 4.3 Surface energies of 1,2-PB, PDMS homopolymer and substrates, and the calculated interfacial energy between the homopolymer and substrate.

	γ (mN/m)	$\theta_{\text{polymer/glass}}$ (º)	$\theta_{\text{polymer/FDTS}}$ (º)	$\Delta\gamma_{\text{polymer/glass}}$ (mN/m)	$\Delta\gamma_{\text{polymer/FDTS}}$ (mN/m)
1,2-PB melt	21.7	28.6 ± 1.3	84.9 ± 1.6	41.0	13.7
PDMS melt	15.7	14.9 ± 0.5	68.3 ± 2.6	44.9	9.8

Note: γ_{Glass} =60.1 mN/m, γ_{FDTS} =15.7 mN/m.

4.3. Summary

All the membranes used in the thesis work are identical in the bulk morphology, bulk porosity, pore size and size distribution as confirmed by SAXS and N_2 adsorption in previous work.[2] Different projections of gyroid morphology were visualized by SEM, AFM, and TEM. Pore size and pore density can be roughly estimated based on microscopic imaging but it is not precise as other techniques mainly due to the projection issue. Gyroid nanoporous 1,2-PB membranes prepared from 1,2-PB-*b*-PDMS copolymers show high structure uniformity in the bulk, isotropically percolating porosity with no need for pre-alignment.

We studied the outer surface of nanoporous membranes in terms of morphology and composition. It was verified that the glass substrate can generate a porous surface while the fluorinated substrate can produce a dense skin layer on the near surface of the nanoporous

membrane. As previously reported, [11,12,16,17] if one component of any binary fluid mixture has a lower surface energy than the other then the system as a whole may save free energy by having the free surface enriched by the lower surface energy component which is higher than the bulk composition. On the other hand, there is a free energy cost associated with creating a surface layer with a different composition as the bulk; an additional unfavorable free energy is also associated with the interface between the surface layer and the bulk material. The equilibrium surface composition and morphology are given by the minimization of the overall system free energy. In our case, the glass substrate showed relative preference toward the 1,2-PB block whereas the fluorinated glass exhibited higher selectivity towards the PDMS block, as confirmed by surface energy measurements. For the cross-linked block copolymer film prepared between the fluorinated substrates, lamellae morphology is stabilized at this interface driven by PDMS coverage of the top surface to minimize the interfacial energy between the polymer and the fluorinated surface. A HPL layer was formed beneath the outmost LAM layer and was linked down to the GYR bulk. After selectively removal of PDMS, the skin layer on the nanoporous membrane is a layer of the cross-linked 1,2-PB with coexistence of the LAM and the HPL morphologes in series from the outmost surface.

We can selectively pattern the self-assembled architecture through suitable choice of substrates in the process of membrane fabrication. This in turn significantly affects the membrane permeation and separation as they will be demonstrated in the following chapters.

4.4. References

[1] Guo, F.; Andreasen, J. W.; Vigild, M. E.; Ndoni, S. Influence of 1,2-PB Matrix Cross-linking on Structure and Properties of Sselectively Etched 1,2-PB-b-PDMS Block Copolymers. *Macromolecules* **2007**, *40*(10), 3669-3675.

[2] Schulte, L.; Grydgaard, A.; Jakobsen, M. R.; Szewczykowski, P. P.; Guo, F.; Vigild, M. E.; Berg, R. H.; Ndoni, S. Nanoporous Materials from Stable and Metastable Structures of 1,2-PB-b-PDMS Block Copolymers. *Polymer* **2011**, *52*, 422.

[3] Jakobsen, M. R.; Grydgaard, A Characterization of Nano Cavities in Polymeric Materials, B.Sc. Thesis. Technical University of Denmark, **2006**.

[4] Gaines, G. L. Surface and Interfacial Tension of Polymer Liquids. *Polymer Engineering and Science* **1972**, *12*, 1–11.

[5] Li, L.; Szewczykowski, P.; Clausen, L. D.; Hansen, K. M.; Jonsson, G. E.; Ndoni, S. Ultrafiltration by Gyroid Nanoporous Polymer Membranes. *Journal of Membrane Science* **2011,** *384*, 126-135.

[6] Li, L.; Schulte, L.; Clausen, L. D.; Hansen, K. M.; Jonsson, G. E.; Ndoni, S. Gyroid Nanoporous Membranes with Tunable Permeability. *ACS Nano* **2011,** *5* (10), 7754 – 7766.

[7] Li, L.; Wang, Y.W.; Vigild, M. E. Ndoni, S. Physisorption of SDS in a Hydrocarbon Nanoporous Polymer. *Langmuir* **2010**, *26* (16), 13457–13465.

[8] Smuleac, V.; Butterfield, D. A.; and Bhattacharyya, D. Permeability and Separation Characteristics of Polypeptide-Functionalized Polycarbonate Track-Etched Membranes. *Chem. Mater.* **2004,** *16,* 2762-2771.

[9] West, P.; Starostina, N. A Guide to AFM Image Artifacts.
http://os.tnw.utwente.nl/otonly/afm%20artifacts.pdf

[10] Bates, F. S. Block Copolymer Thermodynamics: Theory and Experiment. *Annu. Rev. Phys. Chem.* **1990**, 41, 525–557.

[11] Binder, K. Acta Surface Effects on Polymer Blends and Block Copolymer Melts: Theoretical Concepts of Surface Enrichment, Surface Induced Phase Separation and Ordering. *Polymer* **1995**, *46*, 204-225.

[12] Jones, R.A.L., Kramer, E.J. The Surface Composition of Miscible Polymer Blends. *Polymer* **1993**, *34*, 115-118.

[13] Bodas, D.; Malek, C. K. Formation of More Stable Hydrophilic Surfaces of *PDMS* by Plasma and Chemical Treatments. *Microelectronic Engineering* **2006**, *83*, 1277–1279.

[14] Cassie, A. B. D.; Baxter, S. Wettability of Porous Surfaces. *Faraday Soc.* **1944**, *40*, 546–551.

[15] Chow, T. S. Wetting of Rough Surfaces. *Journal of Physics: Condensed Matter* **1998**, *10*, L445.

[16] Hasegawa, H. and Hashimotot ,T. Morphology of Block Copolymers and Mixtures of Block Copolymers at Free Surfaces. *Polymer* **1992**, *33*, 475-487.

[17] Mansky, P.; Russell, T. P.; Hawker, C. J.; Pitsikalis, M.; Mays, J. Ordered Diblock Copolymer Films on Random Copolymer Brushes. *Macromolecules* **1997**, *30,* 6810-6813.

Chapter 5 Gas Permeation and Liquid Flow across Nanoporous 1,2-PB Membranes

The previous chapter discussed structural characteristics of gyroid nanoporous membranes as demonstrated by microscopy techniques. This chapter will play a role of linking the previous chapter and the succeeding ones. Here, we focus on the study of the gas permeation and liquid flow in nanoporous 1,2-PB membranes. We limit our efforts to the non-skin thin membranes (See chapters 3.2 & 4.2.2) in this chapter. The aim is to carry on the demonstration of pore structure, e.g. pore size and tortuosity, and address the transport behavior of gas and liquid in the gyroid nanoporous membranes. This part will thus provide useful information for studying the ultrafiltration property as further presented in chapter 7. The work presented in this chapter has been reported in the manuscript *Ultrafiltration by Gyroid Nanoporous Polymer Membranes* published in *Journal of Membrane Science 2011*.

5.1. Background

As described in chapter 1.1, nanoporous membranes refer to the porous materials with average pore diameter in the 2 – 100 nm range. Prior to discussing the results for our nanoporous membranes, we first briefly review several theories for transport through porous membranes. These theories help to guide our interpretation and understanding of the experimental results for the membranes discussed in this chapter.

5.1.1. Gas diffusion in nanoporous membranes

Both porous and dense membranes can be used as selective gas separation barriers as illustrated in Figure 5.1. The gas permeation in dense membranes is often described by solution-diffusion model.[1] Our non-skin membrane without a dense top layer is certainly in the range of porous membranes. In small nanopores, the mechanism of gas permeation can be dramatically different, depending on the Knudsen number, i.e., the ratio of the mean-free path to the pore

diameter (λ / r).[2] If the membrane pores are extremely small, of the order 5 – 20 Å, then gases are separated by molecular sieving. Transport through this type of membrane is complex and includes both diffusion in the gas phase and diffusion of adsorbed species on the surface of the pores (surface diffusion). If the pores are relatively large, i.e. from 0.1 to 10 μm, the mean-free path is much smaller than the pore size. In this region, diffusion is the result of random collisions between different molecules. Gases permeate the membrane by convective flow as described by Poiseuille's law [2] (equation 5-1), and no separation occurs.

$$J = \frac{\varepsilon r^2}{8\eta} \frac{[P_o - P_l][P_o + P_l]}{l \cdot RT} \qquad (5\text{-}1)$$

where J is the gas flux across the membrane of pore radius r and thickness l under a pressure difference $[P_o - P_l]$; ε is the porosity; η is the viscosity of the gas. R is gas constant and T is temperature. The difference from Poiseuille equation for liquids (See equation 5-6) is the additional term $[P_o+P_l]$ which arises from the expansion of a gas as it moves down the pressure gradient.

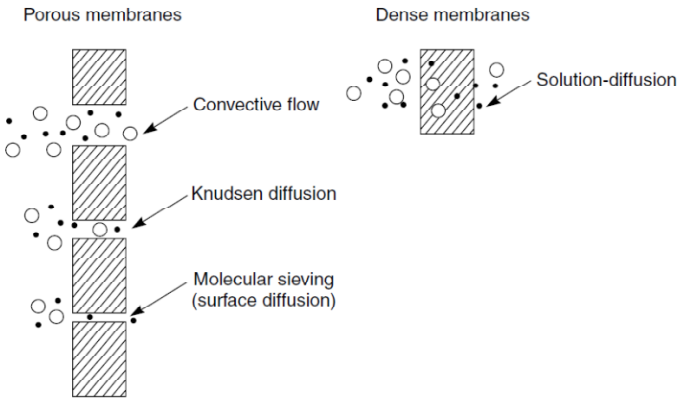

Figure 5.1 Mechanisms for permeation of gases through porous and dense gas separation membranes.[2]

If the pores become comparable with the mean free path of the gas molecules, diffusing gas molecules then have more collision with pore walls than with other gas molecules. Diffusion through such pores is governed by Knudsen diffusion.[1-3] The gas flow in a membrane for Knudsen diffusion is given by equation 5-2,

$$J = \frac{\varepsilon D_{Kn} \Delta P}{\tau \cdot RT \cdot l} \qquad (5\text{-}2)$$

with the Knudsen diffusion coefficient

$$D_{Kn} = 0.66r \sqrt{\frac{8RT}{\pi M_{gas}}} \qquad (5\text{-}3)$$

where M_{gas} is the molecular weight of the gas. ε is the void fraction and τ is the tortuosity. The void fraction accounts for the experimental measurements being based on the total projected area of the membrane, not on the cross sectional area of the pores. The tortuosity accounts both for variations in the size and shape of the pore cross-section and for the additional distance required for a molecule to travel relative to the film thickness.

The important feature of this regime is that the transport rate of any gas is inversely proportional to the square root of its molecular weight. This relationship is called Graham's law of diffusion.[2] The selectivity of this membrane ($\alpha_{i/j}$), proportional to gas permeability, is given by the expression

$$\alpha_{i/j} = \sqrt{M_{gas\_j} / M_{gas\_i}} \qquad (5\text{-}4)$$

If modes of transport other than Knudsen diffusion are occurring, such as bulk diffusion, the selectivity would deviate from this predicted ratio.

5.1.2. Liquid flow in nanoporous membranes

As driven by pressure, the transport of pure liquid through a fresh membrane (J_w) is by viscous flow as described by Darcy's law[1]:

$$J = L_P \Delta P = \frac{\Delta P}{\mu R_m} \qquad (5\text{-}5)$$

where ΔP is the applied pressure across the membrane, L_P is the hydraulic permeability, R_m is the hydraulic membrane resistance and μ is the viscosity of the solution.

Different models have been developed to describe the liquid transport in different pore geometries, showing the effect of specific structural parameters on membrane performance. A simple model of liquid flow through these membranes is to describe the membranes as a series of

cylindrical capillary pores of radius r. The liquid flow through a pore is given by Hagon-Poiseuille's equation as:[1]

$$J = \frac{\varepsilon \cdot r^2}{8 \cdot \tau \cdot \mu \cdot l} \cdot \Delta P \qquad (5\text{-}6)$$

where ΔP is the pressure difference across the pore, μ is the liquid viscosity and l is the pore length, ε is the surface porosity and τ is the tortuosity.

The hydraulic membrane resistance can thus be rendered a physical meaning, which is proportional to r^4. It will be dramatically affected by pore size.

The void fraction is readily calculated from the known volume fraction of the etchable component. We can combine eqs. 5-2 and 5-6 to separate the variables and estimate values for r and τ. These estimated values can then be compared to values obtained using independent material characterization techniques as reported in chapter 4.

5.2. Experimental

All the membranes used in this section were prepared with the sandwich method by solvent casting the 1,2-PB-b-PDMS copolymer solution (BD36 batch) between two glass plates. The membranes thus have a surface porosity of 40 ± 5%. The membranes were surface modified via UV-induced thiolene chemistry method as described in chapter 3.3.

5.2.1. Gas permeation

Single gas permeation measurements were conducted at room temperature in a 2 cm diameter stainless steel dead-end filtration cell, as illustrated in Figure 5.2. A circular disk 1.4 cm in diameter was cut from the membrane sheet to fit into the filtration cell as schematically shown in Fig. 5.2. The sample was placed on a PVC (polyvinyl chloride) disk support and sealed with a rubber O-ring, giving an active area of 0.785 cm^2. The sample with the PVC disk were finally mounted onto the lower part of the cell to separate the cell chamber from the outside. The top of the filtration cell connects with a pressurized N_2 gas bottle (AGA). A 1 mm hole in the center of the PVC disk connects with an outlet drainage to release the permeating gas. Once the membrane

was tightly clamped, the filtration cell was first flushed with the gas to equilibrate for 15 min before recording. The applied pressure was controlled with a regulator and monitored with a manometer with an accuracy of ± 0.025 bar. The permeating gas flow was detected by a bubble flow meter at atmospheric pressure. The measurement for each sample was run about 1 hour at a constant pressure.

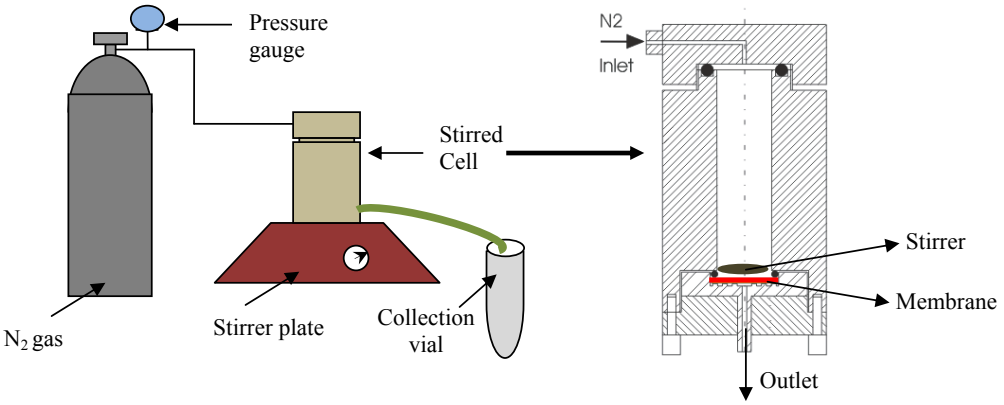

Figure 5.2 Left: An experimental set-up for gas diffusion and liquid flux; **Right:** Detailed schematic drawing of the stirred cell. The tested membrane is highlighted with red color; above the membrane is a stirrer depicted by a dark yellow oval.

5.2.2. Hydraulic permeability

Liquid convection experiments were performed using the same filtration cell as used in the gas permeation tests. Pure water flux (W) and a mixture of ethanol and water in a volume ratio of 80: 20 (EW) were passed through the nanoporous membranes with/without surface hydrophilization. External pressure was applied through the gas inlet by N_2 gas (AGA) to drive convection. For water flux measurement, the original hydrophobic membrane was prewet using ethanol (96% ethanol from KEMETYL A/S, Denmark) for 5 min and replaced with pure water. Once the membrane was in place, the filtration cell was filled with 10 ml liquid and the pressure was set to a desired value. The membrane was flushed for 30 min before the permeating liquid collection. The liquid flow was collected for 1 h in an Eppendorf tube (1.5 ml) and its mass was recorded at planned time intervals on a balance with precision of 0.1 mg. As a new pressure drop applied, the

liquid flow was stabilized for 15 min before the sample collection. Hydraulic permeability was evaluated from the slope of experimental data of the flux (J_w) as a function of the applied pressure drop (ΔP) as described by eq.5-5.

5.3. Results and discussion

5.3.1. Gas permeation

Typical data of H_2, N_2, and CO_2 flow through the original nanoporous membranes are shown in Figure 5.3 as function of applied pressure. The membrane thickness was 25±2 μm. The reproducibility of the same membrane sample and the variation among different membranes of the same thickness were within ± 5%. As expected, the permeation rate of H_2 was greater than N_2, which was in turn greater than CO_2.

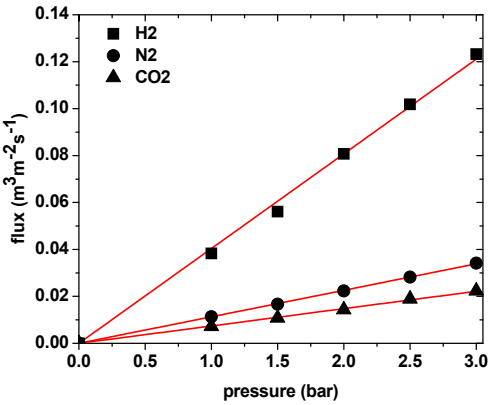

Figure 5.3 Gas permeation vs. pressure. The thickness of membranes was normalized to 25 μm. The solid lines are linear fits of experimental data.

The occurrence of convection flow or Knudsen flow in a pore is mainly determined by the ratio of pore size relative to mean free path of the diffusing gas molecules.[2] At atmospheric pressure the mean free path of common gases is in the range of 50 – 200 nm.[2] It is larger than the pore size (~ 10 nm) of the nanoporous membranes. The diffusing gas molecules then have more frequent collisions with the pore walls than with other gas molecules. Knudsen diffusion is therefore expected to be the dominant mechanism for the gas permeation in the nanoporous

membranes. In this regime, the gas flow in a membrane is given by eq.5-2; the Knudsen diffusion coefficient can be calculated by eq. 5-3.

Table 5.1 summarizes the experimental diffusion coefficient $D_{Kn\_\exp}$ from eq.5-2, using the slope of gas flux vs. applied pressure in Fig. 5.3. Values of theoretical diffusion coefficient D_{Kn_theory} for each gas calculated from eq. 5-3 are also listed in Table 5.1 for a comparison.

Table 5.1 Comparison of experimental and theoretical data of gas diffusion coefficient.

Gas	D_{Kn_theory} [a,b] ($\times 10^{-6}$ m^{2}s^{-1})	D_{Kn_exp} [b] ($\times 10^{-6}$ m^{2}s^{-1})	$\alpha_{i\_Poiseuille}$	α_{i_Kn}	α_{i_exp}
H_2	5.81	5.52	1.00	1.00	1.00
N_2	1.55	1.52	2.00	3.75	3.63
CO_2	1.24	1.22	1.69	4.69	4.52

[a, b.] assume r = 4.95 nm. [b.] assume τ = 1.95, ε = 0.39. The variation of gas diffusion is within ± 5%.

Here porosity ε = 0.39 is determined by volume fraction of PDMS block in the precursor 1,2-PB-*b*-PDMS. We assume tortuosity τ = 1.95, and pore radius r = 4.95 nm (to be addressed later). The values of $D_{Kn\_\exp}$ are very close to the values of D_{Kn_theory} for each gas tested. The selectivity $\alpha_{i\_\exp}$ for the gas relative to H_2 found from experiments is similar within 5% to α_{i_Kn} calculated for Knudsen diffusion from eq. 5-3, showing the molecular weight dependence, i.e. $(1/M_{gas})^{1/2}$. In addition, $\alpha_{i\_\exp}$ shows a big difference from $\alpha_{i\_Poiseuille}$ (3rd data column in Table 5.1) that was obtained for convective flow described by Poiseuille's equation (eq. 5-1). Notably, the order of selectivity for N_2 and CO_2 is wrongly predicted by Poiseuille's flow but rightly predicted by Knudsen diffusion. These findings definitely demonstrate that the gas permeation in the nanoporous membranes occurred by Knudsen diffusion.

5.3.2. Liquid flow

Flux of pure water (W) or 80/20 (v/v) mixture of ethanol and water (EW) were measured for the originally hydrophobic membranes (M) and the hydrophilized membranes (HM) (UV-induced thiolene chemistry, see chapter 3.3). Figure 5.4 shows a plot of liquid flux versus applied pressure across 25 $\pm$2 μm thick membranes. The hydraulic permeability L_p is listed in

Table 5.2, corresponding to the slope of linear fitting lines (Fig. 5.4) based on Darcy's law, eq. (5-5).

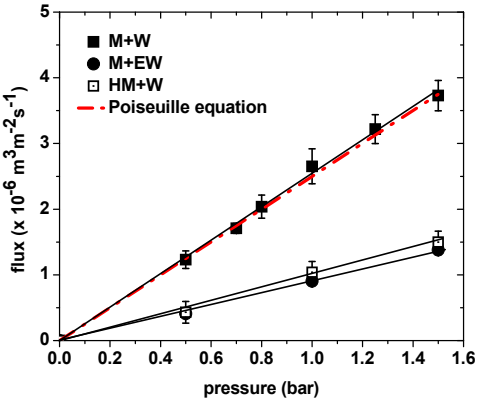

Figure 5.4 Liquid flux through hydrophobic membranes (M): water (W, close square) and a mixture of ethanol and water in volume ratio of 80: 20 (EW, close circle); liquid flux through hydrophilic membranes (HM): W (open square). Black lines are linear fittings to experimental data. Red line: use Hagen Pouiseuille equation to fit experimental data of water flux across the hydrophobic membrane (M+W). Here porosity ε = 0.39 and assume τ = 1.95 and r = 4.95 nm, equal to the gas permeation case (to be addressed later).

For the hydrophobic membranes, the water flux can be well described by the Hagen-Poiseuille equation (eq.5-6) as shown in Fig. 5.4. In the Hagen-Poiseuille equation, the hydraulic permeability L_p is related to membrane structure parameters, porosity ε = 0.39, pore radius r = 4.95 nm, tortuosity τ = 1.95 (equal to the gas permeation case) and thickness l = 25 μm, as well as liquid viscosity μ. The measured EW permeability is only 38% of the water permeability. Most of the lower EW permeability can be explained by an increase of solvent viscosity. The viscosity of EW (v/v 80:20) is twice as large as that of pure water.[4] Other physical or chemical parameters, such as surface tension or surface interaction could also give a contribution to the EW permeability reduction.[5,6]

The hydrophilic membranes experienced a reduction in water permeability by a factor of ~ 2.5. An effective pore size of r ~ 4 nm can be predicted from the dependence of $L_p \sim r^4$ according to the Hagen-Poiseuille equation. Firstly, the sulfonated grafting layer on the pore wall was roughly 4.5 Å with surface density 1.6 groups per nm^7 as estimated from 12% mass increase after the functionalization. This caused a direct reduction in the effective pore size.

Table 5.2 Hydraulic permeability of originally hydrophobic membranes (M) and hydrophilized membranes (HM) for pure water (W) and a mixture of ethanol and water in a volume ratio of 80:20 (EW).

Membrane	Hydraulic permeability ($\times 10^{-6}$, $m^3\ m^{-2}\ s^{-1}\ bar^{-1}$)	
	W	EW
M	2.45	0.93
HM	1.02	-

Moreover, the hydrophilized surface exerted a higher attraction force to water molecules; water mobility therefore decreased at region adjacent to the pore surface. Part of water molecules were presumably bound to sulfonated groups as hydration shells. This certainly reduced the pore size to some extent. If we use Schroeder and Le Bas methods,[8] a projected diameter of a entity of $–S–C_2H_4–SO_3$ with 6 water molecules[9] can be predicted to be 0.92 nm. This estimation is approximately consistent with ~ 1 nm reduction in pore radius as calculated from Hagon-Poiseuille equation. Actually we used DSC measurement to distinguish different water states in the hydrophilized nanoporous membranes (Appendix C). The DSC data confirms the existence of hydration shell (non-freezing bound water). However the DSC data can not quantitatively give precise values for each water state, due to technique difficulties, such as evaporation during DSC, gravimetry error for tiny pieces and other uncertainties.

Finally, using the results of gas permeation and water flux through hydrophobic membrane, we combined eqs.5-2 and 5-6 to obtain the average pore radius 4.95 nm and tortuosity 1.95 for the original nanoporous membranes. These values are calculated from the experimental data and they are not adjustable parameters. We found that the pore size (~ 10 nm in diameter) inferred from gas diffusion and liquid flow is a bit smaller than the value (~ 15 nm in diameter) obtained from SAXS and N_2 adsorption. This might be attributed to the geometric feature of gyroid nanopores as shown in Figure 5.5.[10] The pore structure is periodic; the middle of a pod shows the smallest pore size and the pore size becomes larger at the intersection point of the tripods. The narrowest place should be diffusion determining. Diffusion intrinsically reflects the resistances of pore sizes in series and thus implies a harmonic average of pore diameters.[11] The other methods, e.g. SAXS, often give an arithmetical average pore size.[12] Therefore the value estimated from gas diffusion and liquid flow is expected to somewhat less than that found from SAXS.

Figure 5.5 A bicontinous cubic center structure of gyroid.

The tortuosity 1.95 found in this work is a bit larger than the literature value 1.5.[13,14] It might be due to the inevitable presence of grain boundaries or defects within the matrix which interrupted the percolation of the nanoporosity, thereby showing a somewhat higher value.

5.4. Conclusions

Gas permeation and liquid flux experiments conducted for the gyroid nanoporous 1,2-PB membranes (non-skin samples) resulted in:

- Gas diffusion in our membranes occurred by Knudsen diffusion; selectivity of the diffusing gas is proportional to the inverse square root of molecular weight ratio.
- Water flux through the original nanoporous membrane can be well described by Hagon-Poiseuille equation.
- The permeability reduction in mixture of ethanol/water (80/20, v/v) can be mainly due to an increase in viscosity of the liquid mixture.
- Water flux through the sulfonated hydrophilized membranes showed a water permeability decrease by a factor of 2.5, revealing ~ 1 nm reduction in effective pore radius as predicted by the dependence of $L_p \sim r^4$.

Chapters 4 and 5 have discussed structural characteristics of the nanoporous 1,2-PB polymers as visualized by microscope characterizations and as evaluated by hydraulic permeability and gas permeation. This nano-structured material system exhibits a series of features advantageous to

various membrane applications, such as a uniform and controllable morphology, high nanoporosity, narrow pore size distribution, large surface-volume ratio, and isotropic percolation with no need for structure pre-alignment. At this point, we start to systematically explore the membrane performance of nanoporous 1,2-PB polymer as a dialysis membrane (Chapter 6), ultrafiltration membrane (Chapter 7) and controlled-release membrane (Chapter 8).

5.5. References and notes

[1] Mulder, M. Basic Principles of Membrane Technology, 2ed ed., Kluwer Academic, Netherlands **1996**.

[2] Baker, R. W. Membrane Technology and Applications, 2nd ed., John Wiley& Sons, Ltd., Chichester, **2004**.

[3] Cussler, E. L. In Diffusion, Mass Transfer in Fluid System. Cambridge University Press: New York, **2009**

[4]] Shukla, R.; Cheryan, M. Performance of Ultrafiltration Membranes in Ethanol–Water Solutions: Effect of Membrane Conditioning, *J. Membr. Sci.* **2002**,*198*, 75–85.

[5] Machado, D. R.; Hasson, D.; Semiat, R. Effect of Solvent Properties on Permeate Flow through Nanofiltration Membranes. Part 1: Investigation of Parameters Affecting Solvent Flux, *J. Membr. Sci.* **1999**, *163*, 93–102.

[6] Zaidi, S. K.; Kumar, A. Effects of Ethanol Concentration on Flux and Gel Formation in Dead End Ultrafiltration of PEG and Dextran, *J. Membr. Sci.* **2004**, *237* , 189–197.

[7] Surface modification grafts the pore surface with $–S–C_2H_4–SO_3$ Na via UV-induced thio-lene chemistry. Gravimetry shows 12% mass gain after surface modification, indicating 7.36e-4 mol sulfonate group per unit gram of nanoporous membrane (The molar mass of $–S–C_2H_4–SO_3$ Na is 163g/mol.). This corresponds to 1.6 group per nm^2 surface area (Specific surface area of the nanoporous membrane is 280 m^2/g, Avogadro number is 6.02e-23.).

[8] Poling, B. E.; Prausnitz, J. M. and O'Connell, J. P. The Properties of Gases and Liquids, Fifth Edition, McGraw-Hill, **2004**.

[9] Helfferich, F. Ion exchange, Constable and Company, Ltd, London, **1995**.

[10] http://www.bathsheba.com/math/gyroid/

[11] W. A. Phillip, B. O'Neill, M. Rodwogin, M. A. Hillmyer, E. L., Cussler, Self-assembled block copolymer thin films as water filtration membranes. Applied Materials & Interfaces **2010**, *2*, 847–853.

[12] Schulte, L.; Grydgaard, A.; Jakobsen, M. R.; Szewczykowski, P. P.; Guo, F.; Vigild, M. E.; Berg, R. H.; Ndoni, S. Nanoporous Materials from Stable and Metastable Structures of 1,2-PB-*b*-PDMS Block Copolymers. *Polymer* **2011,** *52*, 422.

[13] Hamersky, M. W.; Hillmyer, M. A.; Tirrell, M. ; Bates, F. S. and Lodge, T. P. Block Copolymer Self-Diffusion in the Gyroid and Cylinder Morphologies. *Macromolecules* 1998, *31,* 5363–5370.

[14] Milhaupt, J. M. and Lodge, T. P. Homopolymer and Small-Molecule Tracer Diffusion in a Gyroid Matrix. *Journal of Polymer Science: Part B: Polymer Physics* **2001,** *39*, 843–859.

Chapter 6 Dialysis Performance of Nanoporous 1,2-PB Membranes

As briefly reviewed in Introduction chapter (chapter 2.3), membrane technology has been realized as a useful tool in biosensor applications.[1] The role of the polymer membranes and the physical properties required intimately rely on the requirements of different types of sensors. Our interest is to develop a diffusion-restricting outer membrane for use in amperometric glucose biosensors. This chapter will focus on the fundamental work on diffusive transport property of nanoporous 1,2-PB polymers as permselective dialysis membranes. Understanding the diffusive permeability properties of the membranes is facilitated by using materials and procedures that allow high degree of control on morphology, substrate-directing surface structure, and tunable active porosity via selectively hydrophilic pattern. This part of work has been reported in the manuscript *Gyroid Nanoporous Membranes with Tunable Permeability* published in *ACS Nano 2011*. The second part of the chapter reports the extended work on evaluation of the performance of the nanoporous 1,2-PB membrane (NPM) in an amperometric glucose sensor. Some problematic issues will be discussed.

6.1. Background

6.1.1. Outer membranes for amperometric glucose sensors

Our work has been performed by collaborating with Radiometer Medical ApS, Denmark. It has primarily been concerned with amperometric enzyme-based glucose sensors. The present efforts have been devoted to develop a diffusion-restricting outer membrane with the nanoporous 1,2-PB polymers.

Here we give a brief description on construction of a conventional Radiometer sensor and the measuring principles. The diagrams (Figures 6.1 and 6.2) and the relevant information are provided by Radiometer, referring to *Reference Manual for ABL^{TM} 700 series*.[2]

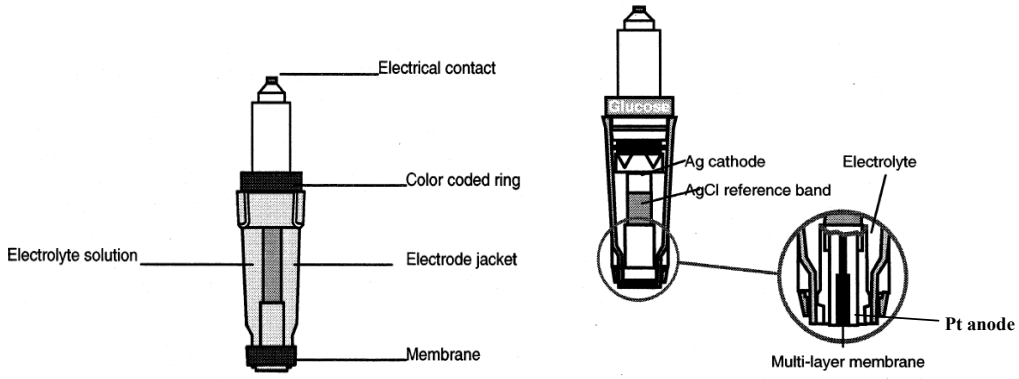

Figure 6.1 A schematic diagram of a generalized Radiometer sensor and a specific glucose sensor.[2]

A generalized diagram of a Radiometer sensor (ABL^{TM} 700 series) is illustrated in Figure 6.1 (left). The main electrode parts consist of 1) electrical contact that provides contact between the electrode and the analyzer; 2) color-coded ring that marks each electrode for easy recognition, e.g. glucose in our case; 3) electrode jacket that holds the electrolyte solution and membrane, and protects the electrode; 4) multi-layer membrane that separates the sample from the electrode, and allows appropriate molecules to pass through from the sample; 5) electrolyte solution that provides an electric contact between anode and cathode inside the jacket. Fig. 6.1(right) shows a specific glucose electrode that consists of a silver cathode, a platinum anode and a AgCl reference band. In this conventional glucose electrode unit, three membrane layers with different

functionality are assembled as a multi-layer membrane and mounted at the tip of the jacket surrounding the electrode. Close to the Pt anode is an inner membrane (IM). It is made of cellulose acetate) which is permeable to H_2O_2 and eliminates interferences as e.g. paracetamol. The middle enzyme layer (EM) composes of glucose oxidase with stabilizers. On the top of the multi-layer membrane is an outer membrane (OM), limiting the throughput of glucose. Enzymes inherently have a maximum rate at which they can catalyze a reaction. If the enzyme is saturated, the rate of reaction is not any longer proportional to the substrate concentration. By placing a diffusion limiting membrane over the enzyme electrode it is possible to increase the external substrate concentration while the rate of reaction is still proportional to the substrate concentration. This is referred to as increased linear range and relies on a decreasing concentration gradient across the membrane. In addition, the outer membrane would be expected to exclude passage of proteins and other large molecules while allowing passage of glucose, oxygen and other small molecules.

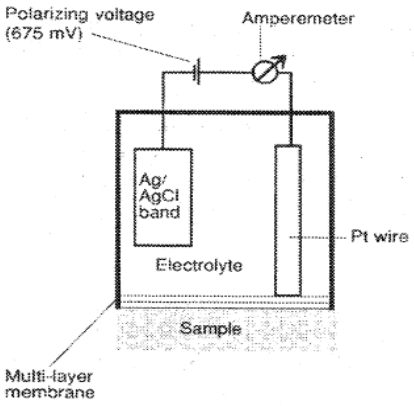

Figure 6.2 A diagram of the electrode chain in amperometric measurements, consisting of the sample, the two electrodes (Pt anode and Ag cathode) and the reference AgCl band, an amperemeter, a voltage source, the membranes and the electrode solutions. [2]

During operation a polarization potential of +675 mV is applied between the working and reference electrode, and the current through the electrode chain is measured by an amperemeter as depicted in Figure 6.2. This current is proportional to glucose concentration in the sample

after appropriate background correction. The potential is applied constantly and the sensor is kept at 37 °C.

Glucose molecules are transported across the outer membrane of the multi-layer membrane. The enzyme glucose oxidase immobilized between the inner and outer membrane layers converts the glucose by the following set of reactions:

$$C_6H_{12}O_6 + H_2O + O_2 \rightarrow C_5H_{11}O_5COOH + H_2O_2 \quad (6\text{-}1)$$

Glucose reaches the enzyme, where it is oxidized to gluconic acid by oxygen, leaving H_2O_2. One molecule of glucose gives one molecule of H_2O_2 at the expense of one molecule of oxygen. O_2 for this reaction is supplied by the outer membrane layer and also by the oxidation of H_2O_2 at the Pt anode. This may require high O_2 permeability of outer membrane, enabling enough O_2 available for the consumption at high glucose concentration. The H_2O_2 produced by the enzyme reaction is transported across the inner membrane to the Pt anode. At the Pt anode H_2O_2 is oxidized and oxygen is regenerated:

$$H_2O_2 \rightarrow O_2 + 2H^+ + 2e^- \quad (6\text{-}2)$$

When a potential is applied to the electrode chain, the oxidation of H_2O_2 produces an electrical current proportional to the amount of H_2O_2, which is directly related to the amount of glucose. In case all the enzymatically generated H_2O_2 reaches the Pt anode the oxygen is fully recovered. In fact, this never happens because the generated H_2O_2 diffuses in all directions, including a diffusion flow back to the sample. In order to limit this back-diffusion the outer membrane must have low permeability towards H_2O_2. To complete the electrical circuit a reduction reaction (where electrons are consumed) at the cathode converts Ag^+ (from AgCl) to Ag:

$$Ag^+ + e^- \rightarrow Ag \quad (6\text{-}3)$$

In the conventional sensor the total processes lead to a net production of HCl, Ag and gluconic acid (at the expense of AgCl, H_2O, and glucose).

A list of specific requirements to the outer membranes used in the conventional glucose sensors is presented here as provided by Lydia D. Clausen from Radiometer Medical ApS at the start of the project.

1. Diffusion limiting in order to show linear response; the characteristic glucose diffusion should be less than 1 x 10^{-9} cm^2/s, maybe even lower, thus enabling that glucose concentration never exceeds 2 to 4 mM in the enzyme layer in order to determine glucose concentrations up to minimum 30 mM in sample;

2. Fast wet-up (< 30 min);
3. Response time < 60 s;
4. Stable glucose diffusion (no swelling);
5. Stable reaction between measurements on blood and aqueous samples (low hematocrit effect); the most pronounced hematocrit effects occur at low and at high hematocrit levels. Block the pores of outer membrane can be one of the reasons causing the hematocrit effect.
6. Allow ion- and buffer diffusion (This is important as the buffer, which stabilizes the pH during the enzymatic reaction must be supplied from the sample/rinse/calibration solution.);
7. Have large O_2-capacity and fast oxygen diffusion rate (must be able to measure on samples with low oxygen content; evaluated by comparison of the measurement results on a 50 mM Glucose sample with 700 mmHg O_2 and 50 mmHg O_2 (Max. 5% decrease);
8. Low paracetamol permeability (no specific value is given);
9. Ratio between H_2O_2 permeability and Glucose permeability close to 3,5 (3,5 is the theoretical value due to differences in their aqueous diffusion coefficients.)

This set of requirements could serve as a reference for our study. However, we did not limit our interests only to biosensor application. In fact, our effort has primarily focused on the study of fundamental transport properties of the membranes. We expect to understand a correlation between structural/physical-chemical properties and diffusive properties of the membranes. Therefore we did not point by point assess the nanoporous 1,2-PB membranes according the requirements above. Instead, we extensively investigated the diffusive transport property of the nanoporous 1,2-PB membranes by adjusting the surface morphology, membrane thickness and active porosity. Membrane selectivity was judged by use of a series of solutes, such as H_2O_2, glucose, proteins, antibiotics and other biomolecules. These results would provide useful information directly or indirectly in relation to the points as listed above.

6.1.2. Diffusive solute transport in pores

The outer membrane in principle functions as a semi-permeable dialysis membrane in the glucose sensor described above. In the absence of significant convective flux, diffusion is an important mechanism for the transport of solutes through the porous membranes. Diffusive transport typically is described using Fick's law that relates the diffusive solute flux to the difference in aqueous phase solute concentration between adjacent regions by means of a diffusion coefficient.[3] Separation between the solutes is obtained as a result of differences in diffusion rates across the membrane arising from differences in molecular size and difference in solubility. Therefore, one of fundamental issues involved in selecting an appropriate outer membrane is to characterize both biomolecule diffusion and size selectivity properties as a function of pore size and pore surface chemistry.

In a porous membrane, the effective diffusion coefficient (D_{eff}) for solute transport is significantly lower than the free-water diffusion coefficient (D_∞), because of the constricted and elongated (tortuous) solute flow paths. The effective diffusion coefficient is related to the free water diffusion coefficient as

$$D_{eff} = \frac{D_\infty \delta \varepsilon}{\tau} \qquad (6\text{-}4)$$

where ε is the effective, transport-through porosity; δ is a constrictivity factor to account for the constricted transport paths caused by the small pores and pore throats in a porous medium; and τ is a tortuosity factor that accounts for the reduction in diffusive flux caused by the tortuous path lengths traced by the solute molecule, compared to the straight paths in an unrestricted aqueous medium. The term D_{eff}/D_∞ is also referred to as diffusive resistance, a measure of the resistance offered by the porous medium to diffusion.[4]

To analyze our diffusion data in relation to pore size and solute size, we used the model which pictures the dissolved solutes as rigid spheres in a cylindrical pore[5,6] as shown in Figure 6.3. Basic assumptions are made regarding the system: 1) the radius of the pore r_p and that of the solute molecules r_s greatly exceed that of the solvent, which is treated as a continuum. 2) The bulk concentration is sufficiently dilute, allowing the solute-solute interactions to be neglected. 3) The pore length l is much larger than its radius r_p. This allows the velocity profile $v(r)$ to fully develop and the velocity of solute molecule to be taken as a constant U (i.e., the system is at steady-state).

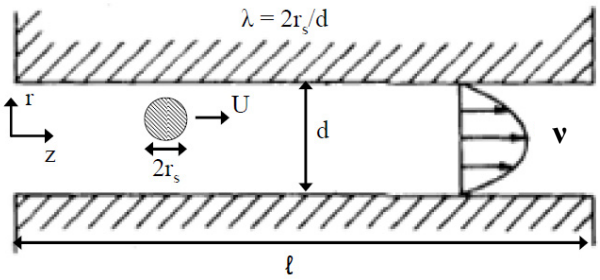

Figure 6.3 A spherical solute in a cylindrical pore. The solute and pore are nearly the same size resulting in a higher drag on the solute than if it were in an unbounded fluid. The magnitude of this additional drag is expressed as a function of the ratio of the solute to pore size.[5]

In average sense, the driving force for diffusion, i.e. the chemical potential gradient, can be viewed as a body force on the solute molecule. With the assumption of steady motion in an isothermal fluid, and neglecting other body forces, this body force is exactly balanced by the hydrodynamic drag:

$$-k_B T \frac{\partial \ln c}{\partial z} - 6\pi\mu r_s K(U - Gv) = 0 \qquad (6\text{-}5)$$

where k_B is the Boltzmann constant; the first term represents the diffusional force per molecule in the + z direction, and the second term is the corresponding hydrodynamic force. The solute concentration is denoted by c and the unperturbed fluid velocity far upstream or downstream from the particle by v. The hydrodynamic coefficients K, the enhanced drag, and G, the lag coefficient, account for the effects of the finite pore size. In an unbounded fluid, $K = G = 1$, and the drag term is equivalent to Stokes' law. One effect of the pore walls is to increase the drag on a sphere translating parallel to the pore axis ($K > 1$). A second effect is to cause the velocity of a freely suspended sphere to lag behind the approach velocity of the fluid ($G < 1$), at any given radial position.

Equation 6-5 can be rearranged by recognizing $Uc = N_s$, so

$$N_s = -K^{-1} D_\infty \frac{\partial c}{\partial z} + Gvc \qquad (6\text{-}6)$$

where N_s is the solute flux. The quantities V, G, K and c all depend on the radial position within the pore, so it is more useful to express the flux averaged over the pore cross section. [5–8]

$$\langle N_s \rangle = -K_D D_\infty \frac{d\langle c \rangle}{dz} + K_C \langle v \rangle \langle c \rangle \quad (6\text{-}7)$$

The coefficients K_C and K_D are the hindrance factors for convective and diffusive transport respectively. Assuming no electrostatic interactions between solute and membrane material, K_C and K_D are functions of the ratio of solute radius and pore size λ $(= r_s / r_p)$. In this study we used Bungay and Brenner model[8] to calculate these two parameters (to be described later).

Integrating eq. 6-7 subjected to the boundary conditions at $z = 0$ and $z = l$ gives an equation for the desired quantity, the macroscopic flux of solutes across a membrane:

$$\langle N_s \rangle = \phi K_C \langle v \rangle c_0 \frac{[1-(c_l / c_0)\exp(-Pe)]}{1-\exp(-Pe)} \quad (6\text{-}8)$$

with $$Pe = \frac{K_C \langle v \rangle l}{K_D D_\infty} \quad (6\text{-}9)$$

where c_l is the solute concentration at $z = l$ and c_0 is the solute concentration at $z = 0$. The equilibrium partition coefficient ϕ for a spherical solute in a cylindrical pore is given by $\phi = (1-\lambda)^2$.

The dimensionless quantity Peclet number is a measure of the speed of convection relative to the speed of diffusion. When transport is dominated by diffusion, i.e., $Pe \ll 1$ the solute flux is given by

$$\langle N_s \rangle = \frac{\phi K_D D_\infty}{l}(c_0 - c_l) \quad (6\text{-}10)$$

When convection dominates transport i.e., $Pe \gg 1$, the solute flux is given by

$$\langle N_s \rangle = \phi K_C \langle v \rangle c_0 \quad (6\text{-}11)$$

In the hydrodynamic models for membrane transport, the reduction in the convective and diffusive contributions to the solute flux, compared with that expected in free solution, is described in terms of the steric and hydrodynamic interactions between the solute and pore walls as described by eqs. 6-10 and 6-11. Bungay and Brenner[8] developed analytical expressions for the hindrance factors of diffusion (K_D) and convection (K_C) for rigid spherical solutes in uniform cylindrical pores using matched asymptotic expansions for both small and close fitting spheres, yielding:

$$K_D = \frac{6\pi}{K_t} \quad (6\text{-}12)$$

$$K_C = \frac{(2-\phi)K_s}{2K_t} \quad (6\text{-}13)$$

The hydrodynamic functions K_s and K_t are both expressed as series expansions in λ and with the coefficients *a*, and *b* given in Table 6.1.

$$\begin{bmatrix} K_t \\ K_s \end{bmatrix} = \frac{9}{4}\pi^2\sqrt{2}\,(1\text{-}\lambda)^{-5/2}\left[1+\sum_{n=1}^{2}\begin{pmatrix} a_n \\ b_n \end{pmatrix}(1-\lambda)^n\right]+\sum_{n=0}^{4}\begin{pmatrix} a_{n+3} \\ b_{n+3} \end{pmatrix}\lambda^n \quad (6\text{-}14)$$

Table 6.1 Expansion coefficients for hydrodynamic functions K_t and K_s in eq. 6-14.

Subscript n	a_n	b_n
1	-73/60	7/60
2	77, 293/50, 400	-2, 227/50, 400
3	-22.5083	4.0180
4	-5.6117	-3.9788
5	-0.3363	-1.9215
6	-1.216	4.392
7	1.647	5.006

In the present work, there is only the diffusive transport across the nanoporous membranes as driven by concentration gradient. As shown in equation 6-15, the diffusive resistance (D_{eff}/ D_∞) as expressed in eq. 6-4 can be predicted by using the hindrance factors of diffusion K_D and will be compared with experimental data.

$$\delta = \frac{D_{eff}}{D_\infty}\,\frac{\tau}{\varepsilon} = K_D\phi\frac{\tau}{\varepsilon} \quad (6\text{-}15)$$

6.2. Experimental

All the membranes used in the chapter 6 were prepared with the sandwich method by solvent casting the 1,2-PB-*b*-PDMS copolymer solution (BD36 batch) between two plates (See chapter 3.2). Non-skin (*ns*), single-skin (*ss*) and double-skin (*ds*) were used for this study (See chapters

3.2 and 4.2.2). The membranes were surface modified via UV photo-oxidation method as described in chapter 3.3.

6.2.1. Diffusion tests

The diffusion cells contain two compartments separated by the membrane disk to be tested, as schematically illustrated in Figure 6.4. The tested membrane was placed onto an O-ring and sealed into the two chambers. Once the membrane was in place, we firstly checked the liquid leakage by filling deionized water in the feed chamber for 1 h. No liquid leakage was observed. Prior to the diffusion tests, both chambers were loaded with ethanol to prewet the hydrophobic membrane for 30 min. The deionized water was then filled to replace ethanol for another 30 min. After prewetting, the feed chamber was set with 5 ml solution to be tested; the permeate chamber was loaded with the same volume of pure solvent (e.g. deionized water or buffer solution). Both chambers were continuously stirred by standard Teflon magnetic stirrers throughout the entire experiment. Equal amounts of solutions were withdrawn from both chambers at planned time intervals. The solutes' concentration (hydrogen peroxide and glucose) in the receiver cell was determined using a commercial electrochemical analyzer at Radiometer Medical ApS; the concentration of the other solutes was determined using an Ultrospec 3000 UV/visible spectrophotometer (Pharmacia Biotech Ltd., Cambridge, UK). All the tested solutes are purchased from Sigma-Aldrich and used as received. They are listed in Table 6.2 together with the specific experimental conditions.

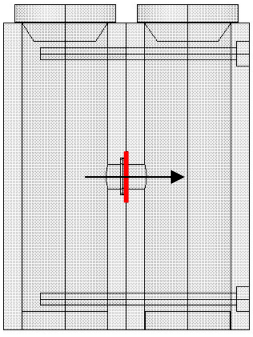

Figure 6.4 A schematic illustration of diffusion cells used in the diffusion tests for all the solutes measured in the present work. The membrane (red) is clamped between two cells. The rubber ring is used for sealing and four screws are used to tighten the two cells.

Table 6.2 Relevant information on solutes used in diffusion tests.

No.	Solute	Concentration	Solvent	UV absorbance peak (nm)
1	Hydrogen peroxide	5 mM	10 mM Imidazole buffer pH 6.5	-
2	Glucose	100 mM	DI[a]	-
3	Sodium L-Lactate	100 mM	DI	-
4	Ciprofloxacin	0.02 g/L	DI	278
		0.02 g/L	DI with 0.15 M NaCl	
		1 g/L	DI	
		1 g/L	DI with 0.15 M NaCl	
5	Ampicillin	1 g/L	DI	257
6	Vancomycin	0.2 g/L	DI	281
		0.2 g/L	DI with 0.15 M NaCl	
		1 g/L	DI	
		1 g/L	DI with 0.15 M NaCl	
7	Cytochrom C[b]	1 g/L	PBS[c] buffer pH 7.4	410
8	Myoglobin[b]	1 g/L	PBS buffer pH 7.4	410
9	Albumin[b]	1 g/L	PBS buffer pH 7.4	278

[a] The deionized water DI was used as it is; pH= 4.5.

[b] The diffusion tests of all the proteins were performed at 8 ºC; the diffusion tests of the other molecules were run at room temperature.

The chemical structures of the solutes used in the study of membrane selectivity are given in Table 6.3.

Assuming constant diffusion and partition coefficients, a linear concentration profile in the membrane is established for diffusion of small solutes e.g. glucose at a much faster time scale than the rate of change in donor or receiver cell concentration (Figure 6.5a). Transport of solute across the membrane can then be described by the pseudo-steady state transport equation[9]:

$$\ln\frac{c_0}{c_1(t)-c_2(t)}=\beta\frac{D_{eff}}{l}t,\quad \beta=A_0\left(\frac{1}{V_1}+\frac{1}{V_2}\right) \qquad (6\text{-}16)$$

where c_0 is the initial glucose concentration in the donor cell; there is no solute in the receiver cell at $t = 0$; $c_1(t)$ and $c_2(t)$ are the glucose concentrations at time t in the donor and receiver cells, respectively; V_1 and V_2 are the solution volumes (cm^3) in the two cells ($V_1 = V_2$); l is the thickness (cm), A_0 is the area (cm^2) of the membrane exposed to the solution, and t is the test time (s). We assume the external mass transfer boundary layer resistance on each side is minimized by

stirring, and that there is no mass accumulation inside the membrane. The slope of the plot $\ln \frac{c_0}{c_1(t)-c_2(t)}$ versus time was used to calculate the effective diffusion coefficient D_{eff}.

Table 6.3 Chemical structure of the solutes.

No	Solute	Chemical structure
1	Hydrogen peroxide	
2	Glucose	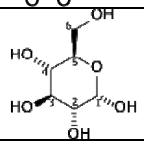
3	Ciprofloxacin	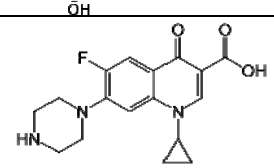
4	Ampicillin	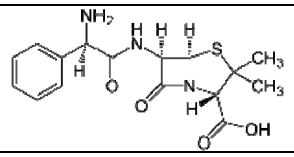
5	Vancomycin	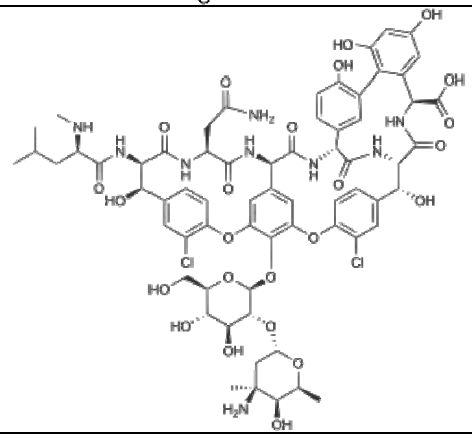
6	Cytochrom C	http://en.wikipedia.org/wiki/File:Cytochromec.png 24 July 2008
7	Myoglobin	http://en.wikipedia.org/wiki/File:Myoglobin.png 27 February 2008
8	Albumin	http://en.wikipedia.org/wiki/File:ALB_structure.png

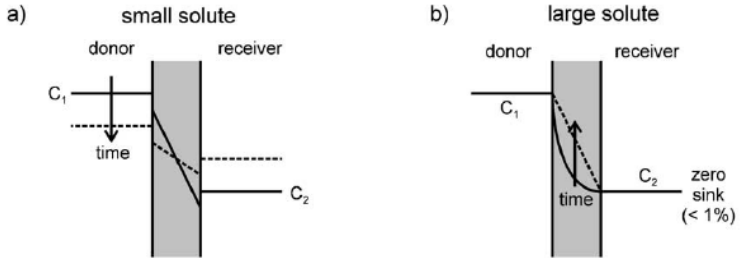

Figure 6.5 Concentration profiles for determination of permeability of membranes toward a) small solutes and b) large solutes.[9]

For large molecular weight solutes such as proteins, the time scale for diffusion in the membrane is much slower and a steady state concentration profile is not reached as quickly. This prevents the use of the pseudo-steady approach. However, since the flux of solute is small, the concentration in the donor cell remains essentially constant and since the tested proteins are detectable at very low concentrations, a zero-sink condition can be assumed on the receiver side (Figure 6.5b). Mass transfer can then be described with the time lag equation[10] written as:

$$M_t(t) = \frac{D_{eff} A_0 c_0}{l}\left(t - \frac{l^2}{6D_m}\right) \qquad (6\text{-}17)$$

where M_t is the total amount of solute that has permeated the membrane at time t, and D_m is the diffusion coefficient in the membrane. The effective diffusion coefficient D_{eff} is determined from the slope of M_t versus time at steady state.

6.2.2. Sensor tests

Preparation of outer membrane assembled electrodes

A series of outer membrane assembled electrodes were prepared for investigating the nanoporous 1,2-PB membrane's performance in a sensor. Because the defects in the skin are not controlled at the present stage (to be addressed later), only non-skin membranes were selected for the sensor tests. Sheets of inner membranes (cellulose acetate) and the enzyme solutions were used as received from Radiometer Medical ApS. 2 µl of enzyme solution was dispensed on the inner membrane, and a piece of nanoporous 1,2-PB membrane (10 mm in diameter, 20 µm in thickness) was then placed on the top of the enzyme solution droplet and slightly pressed down.

As a result, the enzyme layer was immobilized between the inner membrane and the outer membrane. After 1 day drying at room temperature, the multi-layer membrane was then mounted on the tip (inner diameter 4 mm) of the electrode jacket, embraced with an O-ring and further sealed with glue (see Fig. 6.1). The glued electrode was dried for 1 day before any further use. We noticed that the nanoporous membrane was so brittle that it could not withstand the folding around the jacket and the pressure applied by the O-ring sealing. Finally, we decided to apply an extra layer of cellophane on the top of outer membrane thus protecting the outer membrane from directly contacting the O-ring.

Four groups of membrane assembles were tested for evaluation and comparison of sensor responses, as summarized in Table 6.4. Beside the sensor mounted with the nanoporous 1,2-PB membrane (NPM_E), a sensor mounted with the UV-photooxidized nanoporous 1,2-PB membrane (See chapter 3.3) was also tested (NPM_UV_E). In addition, a commercial glucose sensor from Radiometer Medical ApS was used as a standard (Std_E). In order to determine the side-effects of the cellophane layer, e.g. response delay and other possible drawbacks, we also prepared a reference sensor (Ref_E), which consists of the same multi-layer membrane as that in the commercial electrode plus the protective cellophane layer. The outer membranes in both Ref_E and Std_E are track-etched polyethylene terephthalate (PET) membranes.

Table 6.4 Four groups of multi-layer membranes assembled in Radiometer sensors for sensor tests.

Electrode	Std_E	Ref_E	NPM_E	NPM_UV_E
Inner membrane	cellulose acetate			
Enzyme layer	glucose oxidase with stabilizes			
Outer membrane	track-etched PET membrane	track-etched PET membrane	nanoporous 1,2-PB membrane	UV photooxidized nanoporous 1,2-PB membrane
Protective layer	–	cellophane membrane	cellophane membrane	cellophane membrane

Measurement and data analysis

The sensor tests were performed using a Radiometer ABL^{TM} 700 series analyzer with an output for recording current/time (I-t) response. This analyzer was re-built for the use as a sensor evaluation platform in R&D at Radiometer. The re-built platform can give an extended

sensitivity measurement range above 1800 pA/mM, therefore a very high response resulted from NPMs could also be detected (to be addressed later). The jacket was filled with electrolyte solution and mounted on the electrode prior to inserting into the analyzer measurement chamber. The amperometric response of the sensors for glucose was measured in a calibration solution (provided by Radiometer) by applying a potential of + 675 mV to the Pt anode to oxidize the hydrogen peroxide produced by the glucose oxidase enzyme reaction. Different levels of quality control solutions (QC used as received) which contain varying glucose concentrations were used for linearity study. Here it is necessary to first introduce some relevant parameters and data analysis methods in order to better understand the results. Figure 6.6 and the relevant information are provided by Radiometer, referring to *Reference Manual for ABL^{TM} 700 series* [2].

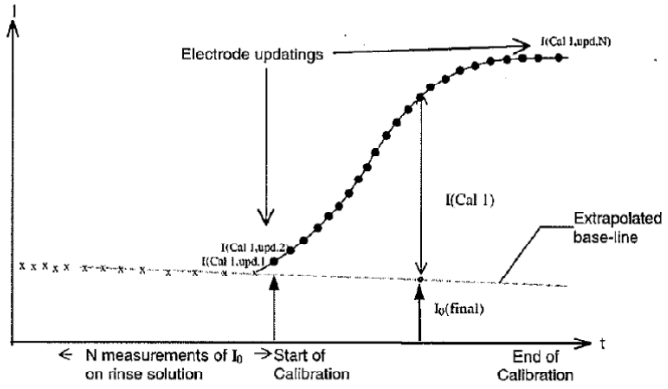

Figure 6.6 A schematic illustration of the registration of electrode response vs. time in expression of *upd.* [2]

Figure 6.6 schematically illustrates the electrode response as function of time in the ABL 700 series. In the ABL 700 series analyzers, electrode signals are registered at 0.982 second intervals during measurements. The registration of each electrode signal begins after the solution to be tested is in position in the measuring modules (black solid circles in Fig.6.6). The measuring time of the electrode is recorded as the number of updating of the electrode's signals. The total updatings (*upd*) from an electrode response are numbered from 1 to 30 for each test, where updating number 1 is the first updating and 30 is the last.

The zero current I_0 is a small background current measured at the electrode as determined from continuous measurements on the rinse solution (no glucose) before a calibration or a sample

measurement starts. The I_0 baseline is obtained from the last 8 registered signals in the rinse solution measurements, as represented by the last cross symbols shown in Fig. 6.6. The baseline is extrapolated throughout the whole electrode calibration or sample measurement period, and represents the zero current time function. The I_0 baseline is used to determine the sensitivity of the glucose electrode.

The sensitivities of the glucose electrodes are calculated by measuring the current on calibration solution 1 (Cal 1, Fig. 6.6) and then subtracting the final zero current (I_0(final), Fig. 6.6). Cal 1 has a nominal glucose concentration of 10 mmol/L. So, the sensitivities of the electrodes are calculated as follows

$$I\,(\text{Cal 1}) = I\,(\text{Cal 1, final}) - I_0(\text{final})$$

$$\text{Sens} = \frac{I(\text{Cal 1})}{c(\text{Cal1})} \qquad (6\text{-}18)$$

where c (Cal 1) is the actual concentration of glucose in the Cal 1 solution, 10 mM/L. I_0(final) is the extrapolated zero current value of the electrode corresponding to the I (Cal 1, final). I(Cal 1) is electrode current due to presence of glucose. The current at the glucose electrodes with Cal 1 in the measuring chamber, I (Cal 1) is measured 30 times at regular intervals. The I (Cal 1, final) is not necessarily the current at last updating. For the commercial electrode (Std_E), it is defined that the current at the 15^{th} *upd* is used as I (Cal 1, final) to determine sensitivity of the glucose electrode. I (Cal 1) in the sample is then calculated as the difference between the current at the final *upd* (the 15^{th}) and the zero current at that time point. For the other electrodes, we select the updating points which give a best fit to a linear dependence of the current response to the varying concentrations. The sensitivity limit of the Std_E is 100-1800 pA/mM.

6.3. Results and discussion

6.3.1. Diffusive permeability of glucose across nanoporous 1,2-PB membranes

Glucose was chosen as a solute for studying the permeation of the nanoporous membranes. Results on glucose diffusion through 20 µm thick non-skin (*ns*), single-skin (*ss*) and double-skin (*ds*) membranes (See chapters 3.2 & 4.2.2) are first presented. Figure 6.7 A is a plot of the

cumulated glucose concentration in the receiver cell as a function of time. As expected, the ns membrane exhibits the fastest glucose permeation, approaching equilibrium of two sides within 30 hours. The *ds* membrane shows the slowest permeation ascribed to the big resistance of the dense skin layer on both sides of the membrane. The equilibrium state of two sides is not achieved for *ss* and *ds* membranes within the measurement time. Figure 6.7 B shows the dependence of the initial glucose permeation rate (at the linear range in Fig. 6.7 A) on membrane thickness for the non-skin, single-skin and double-skin samples. The glucose diffusion across the ns membranes decreased almost linearly with the inverse of membrane thickness. The filled circles in Fig. 6.7 B are data for the ss membrane (empty circles) multiplied by the factor of effective diffusion coefficients calculated for the 20 µm thick membranes in fig. 6.7A (see the discussion below). Figure 6.7 C shows the permeability data for the ds membranes of Fig. 6.7 B re-plotted as a function of membrane thickness l, instead of 1 / l. The surprising increase of flux with membrane thickness can be understood from the model of Figure 6.8 below.

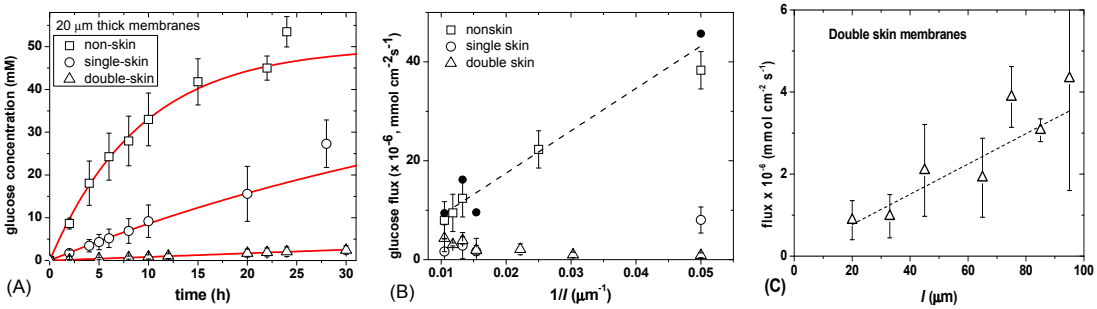

Figure 6.7 Glucose diffusion across non-skin, single-skin and double-skin nanoporous membranes. (A) Glucose concentration in the receiver cell as function of time for 20 µm thick membranes. The solid lines are best fits of eq. 6–16 to the three sets of data (excluding the two data points at longest times for ns and ss, which show higher concentrations due to water evaporation); (B) glucose permeation vs. reciprocal of membrane thickness. The filled circles are the permeability data for the ss membrane multiplied by 5.7 (= D_{ns} / D_{ss}) calculated from the fits of eq. 6-16 to the data in Fig. 6.7 A. The dashed line is a linear fit to the data (squares and solid circles); (C) glucose flux data for the ds membranes as a function of membrane thickness with the dashed line again as a linear fit to the data. The flux increases with membrane thickness! See Fig. 6.8 and the related discussion below.

The best fits of the data in Fig. 6.7 A by eq. 6-16 are shown as solid lines. The fits are very good except for the data points exceeding 20 h, where water evaporation from the cells becomes significant. From the fits the effective diffusion coefficient of glucose was calculated by equation

(6–16) for each type of 20 μm thick membrane: $D_{ns} = 1.20 \cdot 10^{-6}$ cm^2/s; $D_{ss} = 2.09 \cdot 10^{-7}$ cm^2/s; $D_{ds} = 1.88 \cdot 10^{-8}$ cm^2/s. The total diffusive fluxes of glucose for the three types of membranes are proportional to the respective effective diffusion coefficients: $J_{tot,ns} \approx 6 \cdot J_{tot,ss} \approx 64 \cdot J_{tot,ds}$. The flux through ds membranes is almost 2 orders of magnitude lower than through ns membranes.

The skin morphology on ss and ds membranes is the same therefore the resistance-in-series model would predict a maximum reduction by a factor of 2 for the total flux through the ds relative to the ss case, which is significantly lower than the experimental reduction factor of 11. This rather unusual reduction of flux from *ns* to *ss* to *ds* membranes might be due to the existence of few, rather big defects (cracks) randomly distributed on the skin layer(s) with mean inter-distance much bigger than both the membrane thickness and the defect size, as modeled in Figure 6.8. The case of a single skin membrane with cracks was modeled similarly in ref. 13. The dependence of the total stationary fluxes $J_{tot,ss}$ and $J_{tot,ds}$ on the geometric parameters shown in Fig. 6.8 are expected to be valid at the limiting case of $b/l >> 1$ and $b/a >> 1$ [if $b/l >> 1$ but $b/a > 1$ then $J_{tot,ds} \sim l\,\Delta c / (b - a)$].

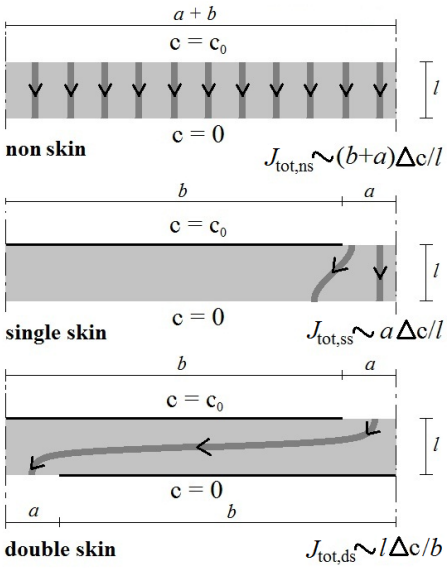

Figure 6.8 Proposed models exhibiting the type of diffusive transport observed for the *ns*, *ss* and *ds* membranes. The membranes are modeled as sheets of thickness l (grey areas) and the skin layer as an infinitely thin impermeable film (black lines) with defects. Defects are presented as parallel non skin stripes of width $2a$ and regular spacing $2\,(b + a)$. Cross-sections of only the symmetry units of the model are shown. In the case of double skin membrane the bottom skin layer is modeled with cracks parallel to those on the upper surface displaced by $a + b$. The dark grey lines with arrows schematically show diffusion transport lines for glucose. The concentrations at $t = 0$ are shown. The approximate relations for total fluxes are expected to be valid at the limiting case of $l/b << 1$ and $a/b << 1$.

The model as described in the caption of Fig. 6.8 reduces the diffusion transport into a two dimensional problem. We believe that it captures the physics behind the differences of diffusive fluxes observed for the three types of membranes. Notice that $J_{tot,ds}$ is expected to increase with

the membrane thickness *l*; this prediction is supported by the data in Fig. 6.7 C showing the flux through *ds* membranes as a function of membrane thickness. Such an unintuitive behavior is actually predicted in all cases with dominant radial transport (parallel to membrane surface). As for the *ss* samples, the model predicts a flux proportional to the defect area and inversely proportional to membrane thickness. The flux is reduced by a factor of $a / (a + b)$ relative to the flux through the ns membrane, which is equal to the fractional area of cracks in ss. Equalizing this factor to the experimental flux reduction factor of 5.7, would correspond to a fractional area of defects in the model equal to 17%. The solid circles in Fig. 6.7 B, which are the flux values for *ss* membranes multiplied by 5.7, overlap within experimental uncertainty with the flux data for *ns* membranes (open squares), in accord with the model prediction. With the above interpretation, values of the model geometrical parameters reproducing the experimental observations for $l = 20$ μm are $b = 5a = 150$ μm. At the moment, the size and distribution of defects is not controlled, therefore in the rest of this chapter we exclusively focus on the non-skin membranes.

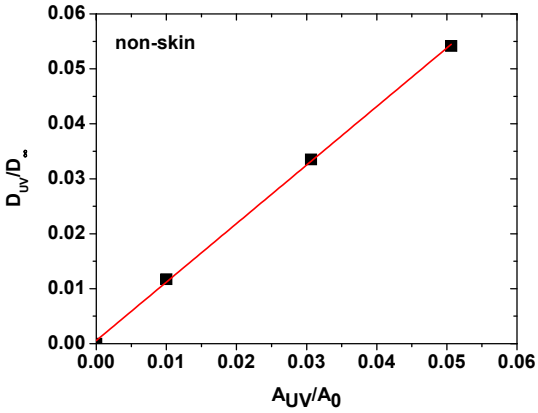

Figure 6.9 Ratio of effective diffusion coefficient of glucose through the selectively hydrophilized membranes relative to that of glucose transport in the fully hydrophilized membranes as function of the ratio of UV-irradiated surface area relative to the effective surface area.

The effective diffusion coefficient D_{eff} across a porous film can be related to the diffusion coefficient in free solution D_∞ by eq. 6-4. Accordingly, we created a series of nanoporous membranes with different active porosity ε to adjust the glucose permeation. We previously reported[14] that the originally hydrophobic membranes can be tuned to be hydrophilic via UV

photo-oxidation (See chapter 3.3). Water can spontaneously penetrate into the hydrophilized nanopores, totally filling the void fraction. As a result, the hydrophilized nanopores are permeable to the diffusing species while no diffusion happens in the native nanopores. This provides an easy means to change active porosity of the nanoporous membrane by hydrophilizing selective regions of the membrane. Figure 6.9 nicely shows that the effective diffusion coefficient of glucose in water through the nanoporous membrane is proportional to the active porosity of the membrane expressed in terms of UV-exposed surface area.

The results above demonstrate that the permeation rate of glucose through nanoporous 1,2-PB membranes can be widely varied either by manipulating the surface morphology of the membrane, or by changing the active porosity. We also attempted to obtain a varying effective diffusion coefficient of glucose by controlling the etching degree of the nanoporous membranes (See chapter 3.2). Unfortunately, a clear correlation between the diffusion coefficient and the etching degree could not be found. The data are presented in Appendix B.

6.3.2. Selectivity of nanoporous 1,2-PB membranes in dialysis

Selectivity was studied as the second important characteristics of the membrane performance. The gained information would help to explore whether this type of nanoporous membrane has practical value in medical device applications. A series of molecules were used to evaluate the selectivity of the non-skin nanoporous membranes with a thickness of 20 μm, including antibiotics, proteins and other biomolecules, as presented in Table 6.5. It summarizes the basic characteristics of the tested solutes. The values of effective diffusion coefficient derived from eqs. 6-16 and 6-17 are listed in the last second column of the table. In the case of proteins, there was a time lag for adsorption equilibration. This equilibration period ensured that the concentration profile across the membrane was at quasi-steady-state.[15] Therefore the starting time for a linear fitting was taken after equilibration rather than at t = 0 as described by eq. 6-17. The values of selectivity α, defined as the ratio of effective diffusion coefficient of glucose to that of the solute tested, are summarized in the last column of Table 6.5. We found that the D_e values for ciprofloxacin (3), vancomycin (4) and cytochrome C (6) were significantly lower than expected from their sizes (see Figure 6.10). Myoglobin and albumin showed extremely little or

no permeation so that the concentration on the receiver cell was lower than the detection limit of the UV-Visible spectrometer used.

Table 6.5 Summary of effective diffusion coefficient, selectivity and related parameters of the solutes tested in the nanoporous membranes [a].

No.	Solute	M_w (g/mol)	r_s [b] (nm)	D_∞ [b] (cm^2/s)	D_{eff} (cm^2/s)	$\alpha_{glucose/i}$ [c]
1	Hydrogen peroxide	34	0.16	1.30E-05	3.20E-06	0.40
2	Glucose	180.16	0.32	6.73E-06	1.28E-06	1.00
3	Ciprofloxacin	311.346	0.55	4.00E-06	4.00E-08	32
4	Ampicillin	349.41	0.58	3.75E-06	5.42E-07	2.36
5	Vancomycin	1449.3	0.79	3.64E-06	1.20E-08	106.67
6	Cytochrom C	12500	1.46	1.50E-06	3.40E-09	376.47
7	Myoglobin[d]	16700	2.33	9.38E-07	< DL	< DL
8	Albumin[d]	66000	3.60	6.07E-07	< DL	< DL

[a] Description of experimental conditions is found in the 'Experimental' section.
[b] Hydrodynamic radius of the solute r_s was calculated from the diffusion coefficient in free solution D_∞, using Stokes-Einstein equation. D_∞ are literature values[16-23].
[c] Selectivity $\alpha_{glucose/i}$ is defined as the effective diffusion coefficient of glucose relative to that of the solute tested.
[d] Below detection limit (0.01 mg/ml for myoglobin and 0.05 mg/ml for albumin).

In general, solute transport in a constricted pore reduces mainly due to equilibrium partitioning and hydrodynamic effects[24]. In order to characterize the hindered diffusion through the nanoporous membranes, the constrictivity δ as determined by eq. 6-4 is plotted *vs.* the ratio of hydrodynamic radius of solutes to pore radius r_s / r_p in Figure 6.10. Here tortuosity $\tau = 1.5$,[25] porosity $\varepsilon = 0.4$ is taken equal to the volume fraction of etched PDMS; the pore radius r_p= 5 nm is determined by gas diffusion and water flux measurements. The hydrodynamic radius r_s of the solute was calculated from the diffusion coefficient in free solution D_∞ using the Stokes-Einstein equation. The plot reveals that space confinement in the nanopores significantly affects the diffusivity of the solutes.

In order to interpret the hindered diffusion of solutes in the nanoporous membrane, the predicted constrictivity from the Bungay & Brenner model[9] (BB) shown by the dashed line in Fig. 6.10 is compared with the experimental data. The BB equation describes quite accurately diffusion of rigid natural molecules through a cylindrical nanopore for r_h / r_p values less than

unity; only steric effects and hydrodynamic interactions between solute and pore wall are considered in this model. It's evident from Fig. 6.10 that only hydrogen peroxide, glucose, and ampicillin follow the model prediction. This indicates that size exclusion and hydrodynamic interactions govern the diffusion of these three molecules in the nanopores.

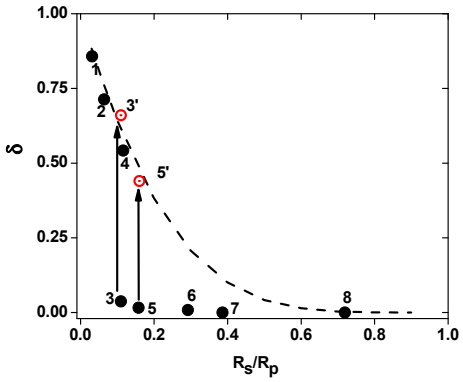

Figure 6.10 Plot of constrictivity of solutes as a function of the ratio between solute radius and the pore radius. The experimental conditions for samples denoted by black solid circles are described in the 'Experimental' section; the detailed explanation of the data shown by open circles is given below in relation to the discussion of Figure 6.11. The dashed curve is prediction from the Bungay & Brenner model.

On the other hand, the hindered diffusion of the other molecules is much slower and the selectivity much higher than expected by BB equation. The permeation of solutes across a membrane does not only depend on the size of solutes or pores; in most cases it strongly depends on a number of solute- solute and solute-membrane interactions[26-30], such as electrostatic, hydrophobic, charge transfer, and hydrogen bonding interactions. These interactions can be significantly influenced by physicochemical parameters, such as pH, ionic strength, transmembrane pressure, surface chemistry of the nanopore wall and so on. In addition, these interactions also depend on concentration which can possibly induce concentration polarization or surface fouling. For instance, the significant reduction in diffusion of cytocrome C can be explained by the fact that the hydrophobic interaction between proteins and the hydrophobic membrane are significant. The resulting reduced effective pore size accounts then for the low transport of proteins.

The influence of the physicochemical parameters on the solute transport through the nanoporous membranes was further investigated in the case of ciprofloxacin and vancomycin. Figure 6.11 illustrates clearly that both the solute concentration and the ionic strength can change the diffusion rate. The diffusion rate increased with increasing ionic strength due to charge screening, which reduces electrostatic interactions between molecules. A lower concentration creates more free space between molecules in water, reducing the effect of electrostatic interaction or hydrogen bonding. In comparison, the solute concentration played a more important role in the diffusion of vancomycin, while the ionic strength affected more significantly the diffusion of ciprofloxacin. This difference may be related to the higher charge density of ciprofloxacin compared to vancomycin and to the extended planar shape of this last, promoting molecular stacking stabilized by hydrogen bonds and π–π interactions. The maximum D_e values shown by the open circles in Fig. 6.11 were used in the calculation of constrictivities for the two solutes as shown by the same symbols in Fig 6.10. It's evident that by altering physicochemical parameters, the diffusion of ciprofloxacin and vancomycin can be changed to follow the BB model.

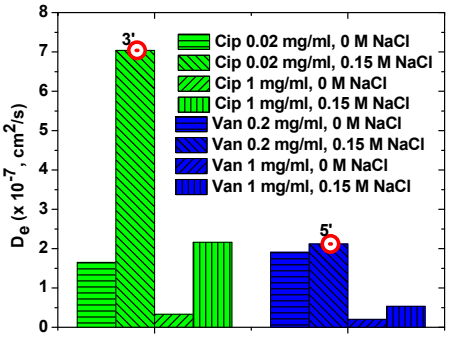

Figure 6.11 Effective diffusion coefficient for ciprofloxacin and vancomycin through the nanoporous membranes at different concentrations and ionic strengths. The red open circles represent the D_{eff} values used to calculate the constrictivities of the two solutes shown by the same symbols in Fig. 6.10.

By now, we have studied the transport properties of nanoporous 1,2-PB in terms of permeability and selectivity by diffusion tests. The transport behaviors of the membranes are of critical importance for weighing the qualification of the nanoporous 1,2-PB membrane as an outer membrane in a sensor. Thus, Table 6.6 compares the relevant parameters for the

nanoporous membranes and the track-etched PET membranes which are used in the conventional glucose electrode for Radiometer sensors. The values for PET membranes are provided by Radiometer; the values for NPMs are from the results presented above. From the comparison, we can see that a reduction of pore size in NPM did not cause a significant decrease in effective diffusion coefficient of glucose ($D_{eff\_glucose}$); however a high porosity of NPM resulted in an effective diffusion coefficient 3 orders of magnitude higher than that of PET. If the NPM is used as an outer membrane for the sensor tests, we possibly have a few problems as

- An undesired high glucose concentration in enzyme layer due to a high glucose permeation; the need of substrate concentrations [S] « K_M for a linear response is thus not satisfied for a sample with high glucose concentration;
- A strong O_2 depletion due to the large amount of transported glucose to enzyme layer;
- Possible effect of high concentration of gluconic acid on the enzyme activity; e.g. disruption in pH stability during the reaction.

Table 6.6 Basic physical properties of track etched PET and nanoporous 1,2-PB membranes.

	pore size (nm)	porosity ε	gas permeability ($m^3/m^2/s/bar$)	$D_{e\_glucose}$ (m^2/s)	D_{e_H2O2} / $D_{e\_glucose}$
Track-etched PET	100	1.3e-04	2.02e-04 (Air)	0.8e-09 (12 µm)	3.5
NPM (*ss*)	10	0.4	1.14e-05 (N_2)	1.28e-06 (20 µm)	2.5

6.3.3. Sensor tests of nanoporous 1,2-PB membranes as outer membranes

In this section we present the results from the preliminary work on evaluation of amperometric response from an electrode assembled with a nanoporous membrane. All the sensor tests were performed at Radiometer Medical ApS, using a re-built ABL^{TM} 700 series analyzer. As we mentioned above, the NPM outer membranes are very brittle. We can not exclude the possibility that some cracks may occur during the measurements. All the following discussions are based on an assumption that no cracks exist.

We used calibration solution 1 (Cal. 1) which contains 10 mM glucose as samples for investigating the amperometric sensor response and stability. As presented in Table 6.4, four sensors with different multi-layer membranes were tested for a comparison. We first check the sensitivity of different sensors. Figure 6.12 represents the sensor sensitivity as function of time.

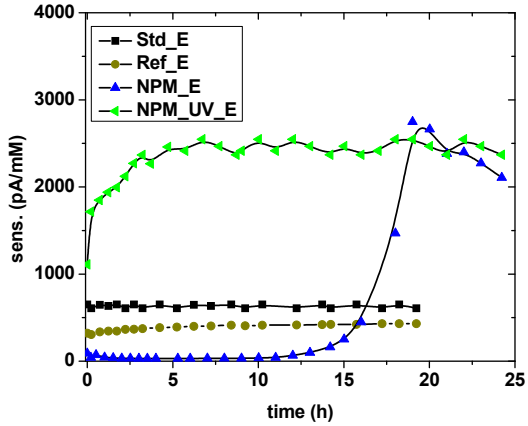

Figure 6.12 Sensitivity of amperometric glucose sensors for different membrane systems: Std_E (black), Ref_E (dark yellow), NPM_E (blue) and NPM_UV_E (green).

The commercial standard sensor (Std_E) showed a constant sensitivity around 600 pA / mM within the limits range of 100 – 1800 pA / mM^2. The reference sensor mounted with a layer of cellophane (Ref_E) had a slight increase within the initial 2 h thereafter a stable status could be reached. The relatively smaller sensitivity given by Ref_E at the stable state might be attributed to the existence of additional protective layer. The inclusion of the protective layer caused a longer diffusion distance to the enzyme layer and lower glucose permeation thus lower signal at steady state. For the nanoporous 1,2-PB membrane assembled electrode (NPM_E), we found that a gentle increase started from 10 h, followed by a sharp transition from 15 h to 20 h. It shows a very low sensitivity at zero current level before 10 h while having a big jump to approx. 2500 pA/mM after 20 h. Similar phenomena were observed for the other NPM_E samples as we repeated the sensor tests. The reason for such transition is uncertain at present. Unfortunately due to time limitation of the project, we could not be able to perform H_2O_2 sensor measurements that would have helped in clarifying if the membrane became cracks after some systematic maintenance schedule. If we assume no cracks occurred, it can be possibly explained with the fact that the nanoporous 1,2-PB membrane is naturally hydrophobic material thus giving little or no permeation to calibration solution. However, each calibration or measurement was always

immediately followed by auto-cleaning step with rinse solution. At standby status, the electrode was also kept in contact with rinse solution. The rinse solution consists of some surfactants that may modify the surface property of the original hydrophobic outer membrane. As a result, a 20 h pre-conditioning period is needed for NPM_E before it can give a stable and detectable current response. Such a long preconditioning period is undesired since a fast wet-up is required which should be less than 30 min. In contrast, the electrode assembled with the photo-oxidized hydrophilic NPM showed a much shorter conditioning time that is comparable to Ref_E; a short initial delay is mainly due to the protective layer.

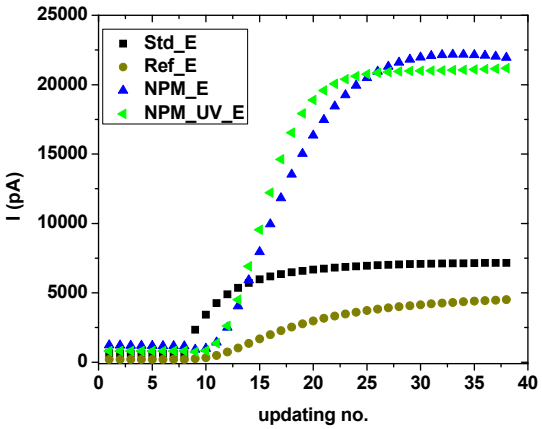

Figure 6.13 Representatives of response curves to 10 mM glucose at the stable state for the different sensors, Std_E, Ref_E, NPM_E, and NPM_UV_E, by use of calibration solution 1 (Cal.1).

Figure 6.13 shows typical *I–t* response curves for each type of electrodes at their stable state. Approximately a 2-updating delay (~ 2 s) occurred to the electrodes with inclusion of the protective cellophane layer. Excluding this point, the NPM_E and NPM_UV_E displayed a sharper slope than the Std_E. A rapid response with 95% plateau current can be attained within 8 s (Note: the first 8 updating data are from the measurements of rinse solution before the measurement of calibration solution starts). The NPM_E and NPM_UV_E generated significantly higher electrical current than the Std_E and Ref_E after the initial stage, which are outside the accepted sensitivity range by Radiometer system. This confirms that the NPM_E and NPM_UV_E produced a dramatically higher glucose throughput. This is because the nanoporous

membranes hold a large porosity relative to the PET membranes (Table 6.6). Such a high current response is produced at the expense of a large consumption of O_2, which requires high O_2 permeability. As presented in Table 6.6, the N_2 permeability is 1.14e-05 $m^3/m^2/s/bar$. Chapter 4 has concluded that the gas permeation follows Knudsen diffusion. Therefore O_2 permeability of ~ 1.06e-05 $m^3/m^2/s/bar$ can be predicted by the dependence of inverse square root of gas molecular weight.

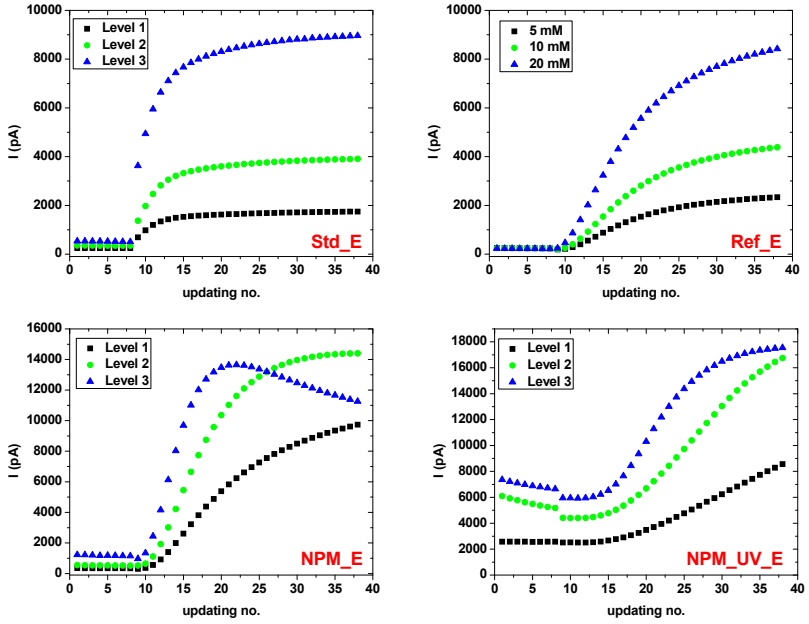

Figure 6.14 Glucose response of different membrane assembled sensors Std_E, Ref_E, NPM_E, and NPM_UV_E, corresponding to varying glucose concentrations.

A series of glucose aqueous solutions with varying concentrations were prepared for the linearity study, as shown in Figure 6.14 for Ref_E. In particular we used different levels of QC solutions (provided by Radiometer) for testing Std_E, NPM_E and NPM_UV_E, and the formulation is as follows:

Level 1: glucose 2.4 mM (1.9 mM ~ 2.9 mM); pO_2 20.40 kPa

Level 2: glucose 5.8 mM (5.0 mM ~ 6.6 mM); pO_2 15.00 kPa

Level 3: glucose 13.8 mM (12.0 mM ~ 15.6 mM); pO_2 8.98 kPa

Note that the difference in pO_2 only exists for the original QC solutions as sealed in glass containers. We leave them exposure to air for enough time before measurements, so we believe that the influence caused by pO_2 difference can be minimized between samples.

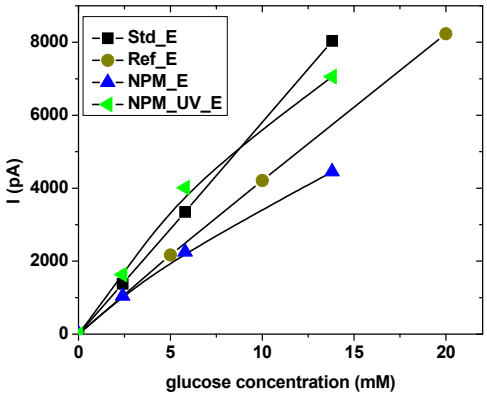

Figure 6.15 Linearity response *vs*. glucose concentration using different sensors Std_E, Ref_E, NPM_E, and NPM_UV_E. The data are selected from Fig. 6.14 to give a best fit to linear relationship.

A dependence of current response on glucose concentration for each type of electrodes is presented in Figure 6.15 by selecting the data (Fig 6.14) which can best fit to a linear correlation (Note it is not necessary to be the data at equilibrium state). As shown in Figure 6.15, Std_E and Ref_E had a wide linear range due to low pore density PET outer membrane. The PET membrane diminishes glucose diffusion by reduction of effective porosity while maintaining relatively free diffusion of the enzyme co-substrate oxygen; both of these effects clearly accentuated the benefits of low pore density membranes. Unfortunately, the NPM outer membrane gave linearity only to ~5 mM. Apparently, decreasing the pore size of the NPM did not result in enhancement of linearity that may balance the linearity loss due to high porosity. In our case, the depletion of H_2O_2 due to a back diffusion is not significant as confirmed by the experimental D_{eff} ratio of H_2O_2 and glucose (Table 6.6). From these observations, it is clear that proper control over the incoming glucose flux is needed to increase sensor linearity. It is important that the sensor is linear in the whole measurement range also on samples with low oxygen. An outer membrane which has high oxygen permeability and the ability to properly control glucose diffusion is preferred. The gas permeation has been in detail discussed in chapter

5. A proper use of diffusion limiting membranes makes it even possible to measure aqueous glucose concentration at values several hundred times higher than the enzyme Michaelis–Menten constant, K_m.[11]

A decrease appeared in NPM_E response after experiencing a maximum value as shown in Fig 6.14. Similar observations were also found for some of NPM_UV_E samples. This is mainly caused by the strong depletion of oxygen, resulting in an undesired O_2 dependence response. It can be also due to limitations in the read-out of electrical signal. In addition, we may take other considerations into account, e.g. enzyme activity in acidic environment, the stability in sensitivity over time as measuring such high glucose samples.

6.4. Conclusions

Diffusive transport properties of NPMs

The diffusive transport can be altered over a significant range by changing surface morphology, thickness, and active porosity. Diffusion profiles for the glucose transport through non-skin, single-skin and double-skin membranes were presented and interpreted by a simple model of defects' size and distribution on the skin layer(s). Particularly for double skin samples the increasing flux with thickness was found. The flux through *ds* membranes is almost 2 orders of magnitude lower than through *ns* membranes. The permeation rate of aqueous solutions can be also tuned by generating patterned hydrophilized regions of the membranes thus varying active porosity. The effective diffusion coefficient over a range of 3 orders of magnitude can be possibly attained as quality of UV source and patterned mask are enhanced. The selectivity of the nanoporous membranes was investigated relative to a series of antibiotics, proteins and other biomolecules. The solute transport was discussed in terms of size exclusion and hydrodynamic interactions. A precise selection can be attained by the size-sorting based on the narrow distributed nanoporosity. In addition, a desired selectivity can be created by involving other interaction effects depending on the nature of molecules. The demonstrated flexible diffusion renders this type of nanoporous membranes interesting for various applications. For example, the skin membranes (when we can well control the defects) with a low flux might be useful for

sensor applications where diffusion restriction is needed. The non-skin membranes might be promising for hemodialysis applications where high flux is desired.

Sensor performance with assembled NPM outer membranes

Due to time limitation, only the preliminary work was performed as presented above. It has been shown that the non-skin nanoporous membrane is not a good candidate for Radiometer glucose sensors because of high glucose permeation. The reduced pore size of NPM relative to PET membrane did not provide significant effect in restricting glucose transport. However, the high porosity of NPM gave rise to unexpected large glucose permeation. As a result, a nonlinear response within reasonable concentration range and a serious oxygen-dependence at high concentration were derived. In order to be comparable with the effect of PET in restricting glucose diffusion, the porosity of NPMs need be reduced by a factor of 3 orders of magnitude.

An outer membrane with glucose diffusion limiting and high oxygen permeation is desired in glucose sensors. As described in chapter 5, gas permeation can occur by Knudsen diffusion as the pore size becomes smaller than the mean free path of the gas (e.g. NPMs) or occur by normal convective flow described by Poiseuille' law as the pores are 0.1 μm or larger (e.g. PET). The latter shows a dependence of J vs. εr^2 while the former shows J vs. εr. Therefore we expect to increase gas permeation by enhancing porosity and pore radius. On the other side we have to keep in mind the glucose diffusion. This can be estimated by Bungay & Brenner model if only size effect exists. In general, low hindrance diffusivity occurs at large ratio of r_s / r_p thus a small pore size is preferred to restrict the glucose diffusion. Finally, a balance between pore size and porosity should be taken by combining these transport theories. In reality, it is much more complex than just taking glucose diffusion and gas permeation into account. For instance, elimination of undesired proteins and interferences is preferred. This will be mainly determined by size sieving or surface adsorption thus pore size and surface chemistry of the membranes become important in this issue. Increasing the membrane thickness is not encouraged since a fast response is required. Enhancement in hydrophilicity would give a fast wet-up and minimize membrane fouling.

There are few possibilities to optimize the NPMs performance in a sensor. For example, it may help by coating a layer of polyurethane on the membrane surface thus reducing both porosity and pore size, or using the double skin nanoporous membranes (with a good control over the

defects). In addition, the mechanical strength of the nanoporous 1,2-PB membranes is also a serious concern in this application and others. Both a reasonable high molecular weight copolymer precursor with less cross-linking degree might make enhanced flexibility for the resultant nanoporous membranes.

6.5. References

[1] Davies, M.L.; Hamilton, C.J.; Murphy, S. M. and Tighe, B. J. Polymer Membranes in Clinical Sensor Applications I. An Overview of Membrane Function. *Biomaterials* **1992**, *13*, 971–977.

[2] Reference Manual for ABL^{TM} 700 series, Radiometer ApS.

[3]Baker, R. W. Membrane Technology and Applications, 2nd ed., John Wiley& Sons, Ltd., Chichester, **2004**.

[4] Saripalli, K. P.; Serne, R.J.; Meyer, P.D.; McGrail, B.P. Prediction of Diffusion Coefficients in Porous Media Using Tortuosity Factors Based on Interfacial Areas. Ground Water **2002**, *40*, 346–352.

[5] Deen, W. M. Hindered Transport of Large Molecules in Liquid-Filled Pores. *AIChE J.* **1987**, *33*, 1409–1425.

[6] Dechadilok, P.; Deen, W. M. Hindrance Factors for Diffusion and Convection in Pores. *Ind. Eng. Chem. Res.* **2006**, *45*, 6953-6959.

[7] Anderson, J. L.; Quinn, J. A. Restricted Transport in Small Pores – Model for Steric Exclusion and Hindered Particle Motion. *Biophys. J.* **1974**, *14*,130–150.

[8] Bungay, P. M.; Brenner, H. The Motion of a Closely Fitting Sphere in a Fluid-Filled Tube. *Int. J. Multiph. Flow*, **1973**, 1, 25–56.

[9] Kermis, H. R.; Rao, G.; Barbari, T. A. Transport Properties of Phema Membranes for Optical Glucose Affinity Sensors. *J. Membr. Sci.* **2003**, *212*, 75–86.

[10] Crank, J. The Mathematics of Diffusion, Oxford Univeristy Press, Oxford, **1975**.

[11] Cornish-Bowden, A. Fundamentals of Enzyme Kinetics. Portland Press, London, **2004.**

Chapter 7 Ultrafiltration Performance of Nanoporous 1,2-PB Membranes

The previous chapter reported the work on diffusive transport properties in the nanoporous 1,2-PB membranes towards a series of proteins, antibiotics and other biomolecules. This chapter will present the study on ultrafiltration properties of the membranes in different conditions and explore their values as ultrafilter. At the present stage, only the non-skin membranes (See chapters 3.2 & 4.2.2) with thickness of 25 μm have been extensively investigated.

A series of PEG molecules with varying molecular weight (MW) were used to explore the effects of fouling on the flux and sieving property of the nanoporous membranes. We begin with a discussion of the membrane–solute interaction by evaluating static adsorption of PEG molecules from two different solvents. An adsorptive fouling with PEG is reflected by reduction of water flux after static adsorption and after ultrafiltration equilibration. We determined the rejection profiles of the nanoporous membranes using a series of single PEG solutions and mixtures of PEG solutions at different flux rates. The effects of solvent properties and surface hydrophilization on the permeate flow and rejection profile were in detail investigated for the nanoporous membranes. Different separation mechanisms can be possibly attained in the ultrafiltration mainly depending on the pore surface chemistry. This part of work has been reported in the manuscript *Ultrafiltration by Gyroid Nanoporous Polymer Membranes* published in *Journal of Membrane Science 2011*.

7.1. Background

7.1.1. Flux model

During ultrafiltration of macromolecules, a severe flux decline is often observed after a short time due to a decrease in the hydrodynamic driving force by osmotic pressure ($\sigma\Delta\pi$) and due to the fouling resistance (R_f,) from surface adsorption and pore plugging.[1] The osmotic-pressure-adsorption model accounts for these effects and was used in the present study. The transport of pure water through a fresh membrane (J_w) by viscous flow is described by Darcy's law: [1]

$$J_w = L_p \Delta P = \frac{\Delta P}{\mu R_m} \qquad (7\text{-}1)$$

where ΔP is the applied pressure across the membrane, R_m is the hydraulic membrane resistance and μ is the viscosity of the solution.

Pure water flux through a fouled membrane after static adsorptive (J_{wa}) and after ultrafiltration-equilibration (J_{wf}) can be described by the resistance-in-series model[1] as shown in equations (7-2) and (7-3), respectively:

$$J_{wa} = \frac{\Delta P}{\mu(R_m + R_a)} \qquad (7\text{-}2)$$

$$J_{wf} = \frac{\Delta P}{\mu(R_m + R_f)} \qquad (7\text{-}3)$$

where R_m is a membrane constant and R_a is the static adsorption resistance. R_f is the fouling resistance that can be divided to subresistances: the initial adsorption layer as described by R_a and further deposition of macromolecules on top of the earlier adsorbed molecules. The difference between R_f and R_a will provide information on the extent of continuous growth of the adsorption layer under dynamic conditions. Relative to the static adsorption, the pressure-forced fouling may produce a denser or thicker adsorptive layer or cause a rearrangement of the molecules adsorbed.

Further, as the filtrate solution passes across a membrane with flux J_v, the osmotic pressure difference across the membrane should be taken into account, especially at high concentration. So eq.7-3 can be extended to an osmotic-pressure-adsorption model,

$$J_v = \frac{\Delta P - \sigma \Delta \pi}{\mu (R_m + R_f)} \qquad (7\text{-}4)$$

where σ is the osmotic reflection coefficient. The osmotic pressure difference term $\Delta\pi$ is determined by the concentration of the filtrate solution at the membrane surface c_m.

The contribution of the osmotic pressure and fouling to flux decline can be more effectively characterized and compared between different types of membranes by normalizing fluxes and flux reductions in relation to the individual membrane resistances. The relative flux reduction (J_r) is defined as

$$J_r = 1 - \frac{J_i}{J_w} \qquad (7\text{-}5)$$

where J_i can be J_{wa}, J_{wf} or J_v to respectively express the relative water flux reduction either after static adsorption (J_{ra}), after pressure-forced fouling (J_{rf}) or the relative filtrate flux decline during the ultrafiltration (J_{rv}).

The relative filtrate flux reduction during ultrafiltration (J_{rv}) can be expressed by

$$J_{rv} = 1 - \frac{J_v}{J_w} = \frac{\pi' + R_f'}{1 + R_f'} \qquad (7\text{-}6)$$

where the normalized resistance parameters are

$$R_a' = R_a / R_m,\ R_f' = R_f / R_m,\ \pi' = \sigma \Delta\pi / \Delta P \qquad (7\text{-}7)$$

J_{rv} can be thought of as the sum of a fouling term (J_{rf}) and an osmotic pressure term (J_{ro})

$$J_{rf} = 1 - (J_{wf} / J_w) = R_f' / (1 + R_f') \qquad (7\text{-}8)$$

$$J_{ro} = \pi' / (1 + R_f') \qquad (7\text{-}9)$$

7.1.2. Transport model

A theoretical description of the relationship between solute transport, pore size and solute molecular size is necessary in order to assess the porous properties of a membrane from an experimental retention curve. In general, the solute flux across the membrane (N_s) is given by the sum of the convective and diffusive contributions,[2]

$$N_s = K_C v c_s - K_D D_\infty \frac{dc_s}{dz} \qquad (7\text{-}10)$$

where c_s is the radially averaged solute concentration in the pore, v is the radially averaged solvent velocity in the pore, D_∞ is the diffusion coefficient in free solution and z is the membrane thickness. The coefficients K_C and K_D are the hindrance factors for convective and diffusive transport respectively. Assuming no electrostatic interactions between solute and membrane material, K_C and K_D are functions of the ratio of solute radius and pore size λ $(= r_s / r_p)$. In this study we used Bungay and Brenner model[3] to calculate these two parameters (See chapter 6.1.2).

With considering size exclusion and hydrodynamic effect alone, the actual rejection Rej_{actual} can be evaluated by integrating eq. 7-10 across the membrane, yielding:

$$\mathrm{Rej}_{actual} = 1 - \frac{c_p}{c_m} = 1 - \frac{S_\infty \exp(Pe_m)}{S_\infty + \exp(Pe_m) - 1} \qquad (7\text{-}11)$$

with the Peclet number Pe defined as

$$Pe = \left(\frac{K_C}{K_D}\right)\left(\frac{vl}{D_\infty}\right) = \left(\frac{S_\infty}{\varepsilon \phi K_D}\right)\left(\frac{J_v l}{D_\infty}\right) \qquad (7\text{-}12)$$

where c_p is the solute concentration at the permeate side ($z = l$) and c_m is the solute concentration at membrane surface at the feed side ($z = 0$); ε is pore volume fraction. The equilibrium partition coefficient ϕ for a spherical solute in a cylindrical pore is given by $\phi = (1-\lambda)^2$. The asymptotic value of the sieving coefficient at large Peclet number (S_∞) is the product of equilibrium partition coefficient ϕ and the hindrance factor for convection K_C. For a semipemeable membrane, at low flux ($Pe << 1$), solute transport is governed primarily by diffusion; the solute concentrations on the two sides of the membrane become nearly equal and Rej_{actual} approaches zero. As the flux increases, Rej_{actual} increases and approaches its asymptotic value at very high flux.

However, as the flux increases, the concentration polarization c_m / c_f also increases as described by the film theory, [4]

$$\frac{c_m - c_p}{c_f - c_p} = \exp\left(\frac{J_v}{k}\right) \qquad (7\text{-}13)$$

where c_f is the solute concentration at the feed side; $k = D_\infty / \delta_m$ is the solute mass transfer coefficient. δ_m is the thickness of boundary layer near the surface. By taking the concentration polarization into account, eq. 7-11 can be rewritten as equation 7-14, relating the observed rejection ($\mathrm{Rej}_{obs} = 1 - c_p / c_f$) and the actual rejection to the flux and mass transfer coefficient:

$$\frac{\mathrm{Rej}_{obs}}{1-\mathrm{Rej}_{obs}} = \frac{\mathrm{Rej}_{actual}}{1-\mathrm{Rej}_{actual}} \exp(-\frac{J_v}{k}) \quad (7\text{-}14)$$

7.1.3. Concentration polarization and fouling

Ultrafiltration (UF) membranes are usually characterized by solute molecular weight cut-off (the molecular weight of the globular molecule that is 90% rejected by the membrane).[4] Pore size and surface chemistry are the intrinsic factors to determine the UF membrane separation by the mechanisms of size-sieving, adsorption or both. However, during ultrafiltration of macromolecular solutions, a severe flux decline or an unexpected separation is often observed after a short period of time. These are mainly caused by concentration polarization and membrane fouling.

Concentration polarization is a natural consequence of selectivity of a membrane. [1,4] This leads to an accumulation of particles or solutes in a mass transfer boundary layer adjacent to the membrane surface that can affect the flux. Dissolved molecules accumulating at the surface reduce the solvent activity and this reduces the solvent flow through the membrane. This can be represented as a reduction in the effective transmembrane pressure driving force due to an osmotic pressure difference between the filtrate and the feed solution adjacent to the membrane surface. This phenomenon is inevitable, but is reversible. As described in eq. 7-13, the concentration polarization can be reduced by reducing the flux J via manipulating the transmembrane pressure, and by enhancing the mass transfer coefficient k through increasing the feed velocity along the membrane or changing the module configuration. The ratio of J / k can be used to predict the degree of concentration polarization in UF experiments.

Membrane fouling is a build-up material on the membrane surface. Membrane fouling may occur as the following forms: [5]

- *Adsorption*: this occurs when attractive interactions between the membrane and the solute or particles exist. A monolayer of particles and solutes can grow even in the

absence of permeation flux leading to an additional hydraulic resistance. If the degree of adsorption is concentration dependent then concentration polarization exacerbates the amount of adsorption.

- *Pore blockage*: when filtering, pore blockage can occur leading to a reduction in flux due to the closure (or partial closure) of pores.
- *Deposit*: a deposit of particles can grow layer by layer at the membrane surface leading to an additional hydraulic resistance. This is often referred to as a cake resistance.
- *Gel*: it is initially caused by concentration polarization; the level of concentration polarization may lead to gel formation for certain macromolecules.

Membrane fouling often causes a severe flux decline. Several distinct periods of behavior have been identified in relation to the flux decline as depicted in Figure 7.1. [6]

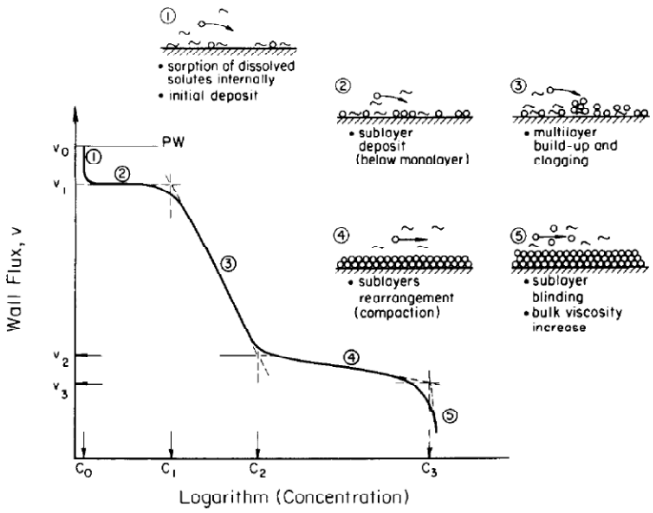

Figure 7.1 Periods of different physical phenomena during flux decline with suspended and dissolved solutes in the feed.[6]

The physical phenomena at Periods 1 and 2 might be the main reasons to explain the flux decline in our case. At the initial phase of the experiment (*Period 1*), the membrane is immediately exposed to the dissolved macromolecules in the medium. If there membrane-solute interaction exists, a fast adsorption of the dissolved macromolecules may occur onto the membrane surface (most of which is within the membrane structure). This can result in a decline

in the permeation rate. The kinetics of macromolecule sorption is thought to be fast and the binding constants high. [7] When all the sorption sites are occupied, a pseudo-steady state is reached. *Period 2* is build-up of first sublayer. During this period the suspended solutes begin to deposit onto the membrane slowly increasing the sublayer coverage. Since for most of this period monolayer coverage has not yet been attained, there is little effect on the permeate rate. As monolayer coverage approaches, if solute-solute interaction happens, there will be followed by a build-up of multilayer (*Period 3*).

7.2. Experimental

Non-skin nanoporous 1,2-PB membranes were used in the present work. All the membranes were prepared with the sandwich method by solvent casting 1,2-PB-b-PDMS copolymer solution (BD36 batch) between two glass plates, thus showing surface porosity of 40%. The membrane thickness is designed to be 25 μm. The nanoporous 1,2-PB membranes are natually hydrophobic. For comparison in ultrafiltration properties, one batch of the original membranes was functionalized via UV-initiated thoil-ene chemistry. Both membrane preparation and surface hydrophilization have been described in detail in chapters 3.2 and 3.3.

7.2.1. Static adsorption of PEG

Nanoporous membranes were immersed into PEG solutions (1 g/L) and kept on a shaker. Prior to dipping in the PEG solution, the original hydrophobic membranes were prewet with ethanol and then replaced with pure water. After 48 h of immersion, they were rinsed twice in pure water, 1 min for each time in order to remove the excess solution on membrane surface. Gravimetry, FTIR and water flux of the membranes were measured before and after exposure to PEG solutions. The PEG adsorption is defined as the difference in the dry mass before (m_0) and after PEG adsorption (m_a) normalized by m_0 as follows:

$$\Delta m_{PEG} = \frac{m_0 - m_a}{m_0} \cdot 100\% \qquad (7\text{-}15)$$

The static adsorption resistance R_a was calculated from experimental data of relative water flux reduction J_{wa} according to eqs. 7-1 and 7-2.

Three systems were tested to study the effect of solvent property or surface hydrophilization on membrane-PEG interaction. They were original hydrophobic membranes in aqueous solution of PEG (M+W); original hydrophobic membranes in PEG solution in a 80/20 (v/v) mixture of ethanol and water (M+EW); and hydrophilized membranes in aqueous solution of PEG (HM+W). The basic information relevant to the used PEG molecules is listed in Table 7.1.

Fourier transform infrared FT-IR spectroscopy (Perkin-Elmer Spectrum One) spectrum was recorded to analyze the surface chemistry of nanoporous membranes after static PEG adsorption. 64 scans were accumulated for each run both in ATR mode and transmission mode in the range of 4000–600 cm^{-1} with 4 cm^{-1} resolution.

7.2.2. Ultrafiltration of PEGs

PEG ultrafiltration experiments were conducted at room temperature in a 2 cm diameter stainless steel dead-end filtration cell, as illustrated in Figure 7.2. This is the same set-up as described in chapter 5.2.1 for gas permeation and liquid flow measurements.

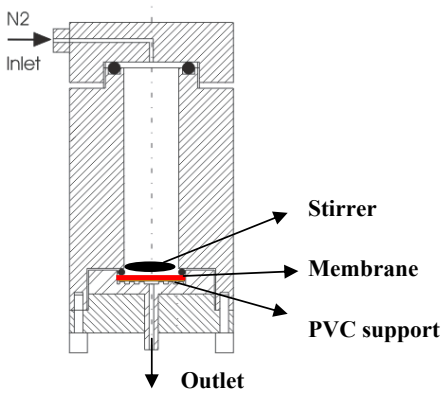

Figure 7.2 An experimental set-up for PEG ultrafiltration measurements. The tested membrane is highlighted with red; above the membrane is a stirrer depicted by a black oval.

A circular disk 1.4 cm in diameter was cut from the membrane sheet to fit into the filtration cell. The sample was placed on a PVC disk support and sealed with a rubber O-ring, giving an active area of 0.785 cm^2. The applied pressure was controlled by a regulator and monitored with a manometer with an accuracy of ± 0.025 bar. A series of solutions of single PEG molecules or a mixture of PEG molecules were used to explore the differences in ultrafiltration properties of

the three systems, M+W, M+EW and HM+W. PEG were dissolved in either pure water (W) or a mixture of ethanol and water (EW, v/v 80:20) at a concentration of 1.0 g/L. Seven different molecular mass of PEG molecules (see Table 7.1) were tested to characterize the rejection profiles of the nanoporous membranes. A mixture of PEG solutions only contains PEG molecules with molecular weight (MW) from 1 kg/mol to 35 kg/mol and 0.2 g/L for each molecular weight of PEG.

Table 7.1 Basic characteristics of PEG molecules used in this study.

PEG Sample	M_n (kg/mol)	R_h (nm)[a]	Producer
PEG1K	1.0	0.78[8]	Sigma-aldrich
PEG4K	4.0	1.72[9]	Merck
PEG8K	8.0	2.62[8]	Fluka
PEG12K	12.0	3.53[10]	Fluka
PEG35K	35.0	8.22[8]	Fluka
PEG56K	55.6	10.54[8]	Polymer Laboratories
PEG100K	97.4	18.11[8]	Polymer Laboratories

[a.] the cited hydrodynamic radius of each PEG molecule.[8-10]

Wetting procedures were the same as for the liquid convection measurements. Once the membrane was in place, wet, and flushed, the pure solvent flux was run for 1 h at a pressure drop of 1 bar to check if the membrane performed consistently with the membranes used for liquid convection experiments. At this point, the filtration cell was filled with 10 ml of feed solution, the stirring speed was set at 500 rpm and the pressure drop was then set to the desired value. The system was flushed for 30 min before collecting the permeate solution. The mass of the permeate solution was measured at certain time intervals to obtain a profile of the permeate solution flux with time. Thereafter, the solution was removed and the cell was rinsed twice by filling with pure water to remove the excess of PEG solution on the membrane surface. Each ultrafiltration run was followed by pure water flux measurement for 1 h in order to reveal the pressure-forced membrane fouling and compare with the static PEG adsorption. The water flux measurement was conducted as the liquid flow measurements presented in chapter 5.2.2. The relative water flux reduction and fouling resistance were calculated from eqs. 7-3, 7-5 and 7-7. After each

measurement, the membrane was washed in chloroform for at least 3 hours and then rinsed with ethanol and water before it was used for next measurement.

The concentrations of the PEG solutions from both permeate side and feed side were analyzed by size exclusion chromatography (Shimadzu) with a RI detector (RID-10A), using an Ultrahydrogel^{TM} 250 column (particle size 6 μm, 7.8x300 mm) (Waters). The mobile phase was 95% water with 5% methanol. The flow rate was set to 1 ml/min and the injection volume 100 ul. The observed rejection $Rej_{obs}(=c_p / c_b)$ was determined by integrating the area under the SEC peak.

7.3. Results and discussion

7.3.1. Membrane fouling under static and dynamic conditions

Membrane performance, both filtrate flux and selectivity can be severely affected by concentration polarization and membrane fouling.[1, 4, 5, 11] The latter includes gel layer, adsorption, pore blocking, deposit, and cake formation. Macromolecules such as proteins, polysaccharides and synthetic polymers in the feed solution are generally considered to highly contribute to the build-up of membrane fouling.[5] In this study, PEG was selected as to examine ultrafiltration properties of the nanoporous membranes. To reveal the potential fouling and better interpret the ultrafiltration results, we first present the static adsorption of PEG from two different solvents for both hydrophobic and hydrophilic membranes.

Static PEG adsorption was performed in the M+W, M+EW and HM+W systems with 1 g/L PEG solutions for 48 h. Figure 7.3 shows the mass gain after static adsorption of PEG with different molar masses. Over a molecular weight (MW) range of 1 – 35 kg/mol, the M+W system showed a significant mass increase (Note it is much higher than the values expected for the only outer-surface-adsorption); while much less mass was gained in the HM+W system and even less in the M+EW system. In conditions of equi-partition of PEG between the pores and the bulk, the mass would increase by at most 0.067%, which is negligible relative to the observed adsorption values. In fact, it should be much less for the bigger molecules due to the exclusion effect.

Therefore significant PEG adsorption occurred on the large hydrophobic pore surface in the M+W system. The adsorbed mass increased from 8% for the PEG1K to about 17% for PEG35K, as shown in Fig. 7.3. Diffusive permeability of the molecules on the basis of size would decrease exponentially with the ratio of solute size to pore size as depicted by solid curve in Fig. 7.3. From size considerations alone, no detectable mass uptake would be expected for PEG35K, since it has a hydrodynamic radius larger than the pore radius (Table 7.1).

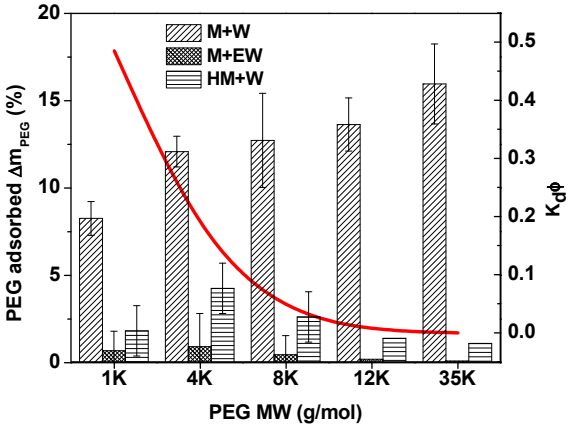

Figure 7.3 The amount of adsorbed PEG relative to the original mass of the membrane after 48 h of contact with PEG solutions (1g/L) in 3 different systems: M+W, M+EW, and HM+W. The solid curve represents diffusional hindrance factor for PEG in the membranes as a function of r_s / r_p as described by Bungay and Brenner model,[3] with consideration of size effect alone.

However, the mass of the nanoporous membrane increased by 17% in the presence of PEG35K in water (M+W). In our opinion, unlike rigid solutes, the adsorption onto the pore walls changes the conformation of the flexible PEG macromolecules thus allowing the infiltration of the large molecules into the nanopores. In other words, the adsorption enthalpy gain in the case of the hydrophobic membrane in water compensates for the reduction in conformational entropy of the macromolecules in confinement inside the nanopores. In the HM+W system, surface hydrophilization significantly diminished the PEG–membrane interaction. The decreasing mass uptake for PEG molecules larger than PEG4K was mainly governed by the size exclusion effect due to a smaller effective pore size in the hydrophilic membrane (this has been addressed in chapter 5.3.2). On the other side, the enthalpy adsorption effect is expected to be weaker in this case, though still present giving rise to a measurable PEG35K mass uptake. Lastly we found that

the presence of ethanol seems to efficiently prevent the accumulation of PEG on the hydrophobic surface.

Interfacial energy can possibly account for the different phenomena of the static PEG adsorption in the three systems. The surface tension decreases in the order: H_2O (~72 mN/m)> PEG (~44 mN/m) > 1,2-PB (~25 mN/m) > Ethanol (~22 mN/m). For M+W system, PEG molecules show a strong tendency to adsorb on the hydrophobic surface to minimize $\Delta\gamma_{W-M}$ via hydrophobic interaction. In EW system, $\gamma_{Ethanol}$ is much closer to $\gamma_{1,2-PB}$ than γ_{PEG} thus there is no driving force for PEG adsorption in this case. As the original membrane surface was functionalized with sulfonated groups, a layer of water would bind on the hydrophilic surface as a consequence of hydration. Hence PEG adsorption is not preferred any longer. However, still some detectable adsorption happened in the HM+W system as reflected by mass gain. It is probably due to dipolar interaction or H-bonding between PEG molecules and the bound water molecules or the sulfonate groups.

Water flux was measured across the membranes after static adsorption in order to evaluate its effect on flow. The relative flux reduction of pure water after static adsorption (J_{ra}) was determined by eq. 7-5, as denoted by the square symbols shown in the three panels of Figure 7.4.

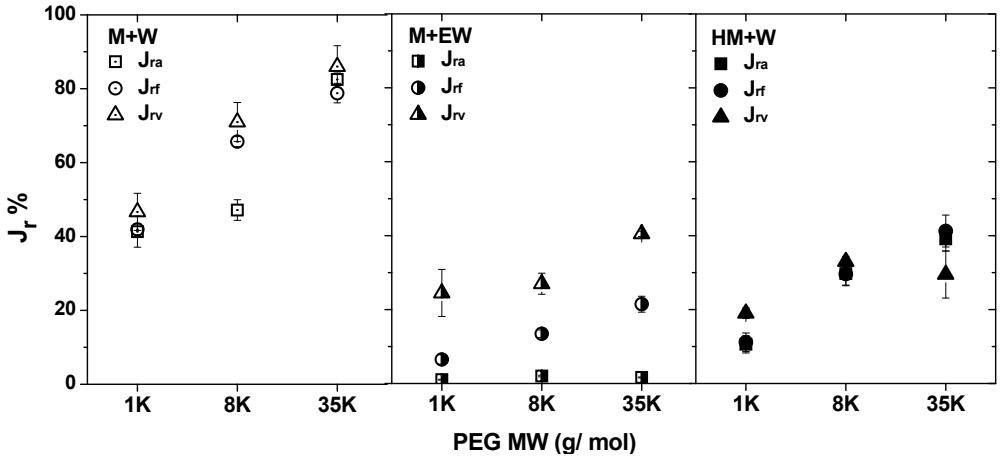

Figure 7.4 Relative flux reduction of pure water after static adsorption (J_{ra}, square symbols) and after ultrafiltraion equilibration fouling at 1 bar (J_{rf} , circle symbols); the filtrate flux decline during ultrafiltration relative to the pure solvent (J_{rv} , triangle symbols). PEG1K, PEG8K and PEG35K were measured for the 3 systems: M+W (left), M+EW (middle) and HM+W (right).

After static adsorption, the M+W system presented a significantly greater reduction in water permeability than the other two systems, giving a water flux reduction of ~ 40% for PEG1K and up to 80% for PEG 35K. Negligible water flux reduction J_{ra} was seen in the M+EW system; the small difference in water flux is of the same order as the experimental uncertainty. In the HM+W system, J_{ra} is considerably smaller than for the M+W system, but surface hydrophilization apparently is not as effective as ethanol in preventing PEG static adsorption. These observations agree well with the results shown in Figure 7.3.

A pronounced effect of molar mass on the water flux reduction J_{ra} is clearly seen in Figure 7.4 for the M+W and HM+W systems. We noticed that the dependence of J_{ra} (Fig. 7.4) is not simply proportional to the amount of PEG adsorbed (Fig. 7.3). In the HM+W system a relatively higher J_{ra} was observed than what we expected from the mass gain. Firstly, this could be interpreted as due to pore-blocking which is more likely to occur with larger molecules; while smaller molecules mostly cause pore-narrowing by adsorption onto the pore walls.[5] With increasing r_s / r_p the probability for pore blocking will increase. As suggested by Zydney et al.,[5] the pore blocking will yield a higher contribution to membrane resistance than pore narrowing. Ulbricht et. al. also observed a similar effect from Dextran on adsorptive fouling of PES membranes.[12] Secondly, water mobility could also be slowed down due to the larger PEG molecules that cause a higher friction to water molecules inside pores. Particularly, due to the smaller effective pore size in the HM+W system (this has been addressed in chapter 5.3.2), the same extent of static adsorption would lead to a more serious flux reduction as shown in Fig. 7.4. At the moment we do not understand the location of the data point (two measurements) for the sample PEG8K in Fig. 7.4 for the M+W system.

We also examined the hydrophobic membrane samples after static adsorption in water by performing FTIR measurements in both ATR and transmission modes (TM). Figure 7.5 gives representatives of ATR and transmission spectra for PEG1K and PEG100K. The main feature of these spectra is the presence of all the bands of PEG molecules in the spectrum of the nanoporous 1,2-PB. These spectra clearly demonstrate the PEG adsorption. A peak at ~ 1640 cm^{-1} is a characteristic peak of double bounds in 1,2-PB; A broad peak at ~ 1100 cm^{-1} is ascribed to the –CH2–OH group in PEG molecules. ATR mode usually reflects the informative depth of 1~ 2 μm while transmission mode can be able to give the information across the entire bulk

thickness (i.e. 25 μm). In order to reveal the effect of molecular weight on the depth of PEG penetration into the deep pore structure, we made a plot as shown in Figure 7.6.

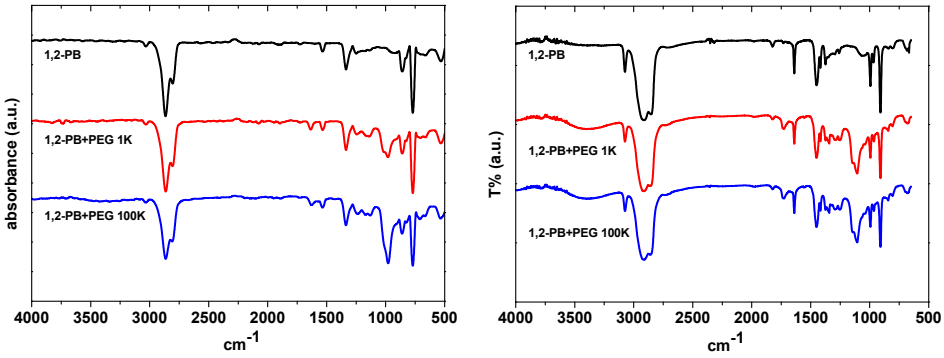

Figure 7.5 IR spectra of ATR mode (left) and transmission mode (right) for nanoporous membranes before and after static adsorption of PEG1K and PEG100K.

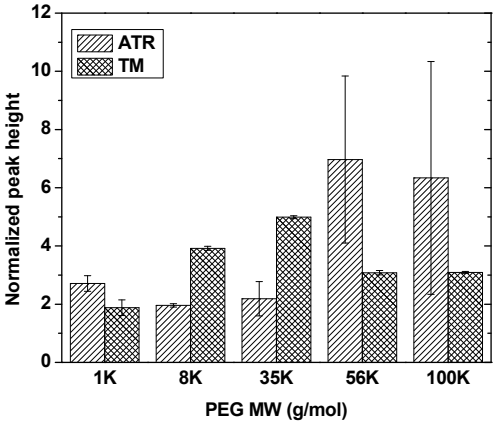

Figure 7.6 Normailized peak height of the peak at 1100 cm^{-1} relative to the peak at 1640 cm^{-1} in ATR mode and transmission mode for the nanoporous membranes after static adsorption of PEG molecules with different molar mass.

Fig. 7.6 compares the normalized peak height of peak 1100 cm^{-1} (relative to peak 1640 cm^{-1}) in the spectra of ATR mode and TM mode for the static adsorption of PEG molecules in the range of 1–100 kg/mol. Due to many technique limitations, it is though not easy to make quantitative comparisons between the two sets of results from ATR and TM. One of the reasons

is that the probing depth of ATR increases with the wavelength, therefore it's a problem to compare signal ratios at two different wavelengths derived from the two techniques. Another reason is related to the absorption coefficient, which is defined by Lambert–Beer's law. This law may break in cases of very high absorption/concentration or high scattering. Especially scattering may be a problem for opaque materials and it will definitely be different in ATR relative to TM. Thus, we can only have rough qualitative comparison between results from these two modes. For PEG 56K and 100K, the TM mode shows the normalized peak height significantly lower than that in ATR mode. This may indicate most of PEG 100K molecules accumulated at the outer surface or stuck at the entry of the pores. This quantitatively supports the discussion described above.

Pressure-forced adsorption was further performed for the three systems with 1g/L PEG solutions at a pressure of 1 bar for 2 hours. Relative water flux reduction after ultrafiltration equilibration (J_{rf}) was calculated from eq. 7-8 evaluating the extent of adsorption under dynamic conditions, as shown by the circle symbols in Fig. 7.4.

The fouling resistance can be considered as a continuous growing deposition on the membrane surface, including the fast built-up of adsorption layer on the membrane surface and subsequent deposition of molecules on the initial adsorption layer. The initial adsorption layer can be thought of to be the same as the static adsorption layer depending on intrinsic surface chemistry of the membrane (Fig 7.1, Period 1) while the further deposition mainly depends on solute–solute interaction, regardless of the membrane type. Fig. 7.4 shows that the M+W system and the HM+W had each J_{rf} similar to J_{ra}, that is, in these two cases the fouling resistance R_f is similar to the static adsorption resistance R_a. This may suggest two possibilities for 1) A maximum adsorption was reached under the static conditions and the applied pressure did not result in further deposition of PEG molecules. This is indicative that solute-solute interactions are negligible in the M+W and HM+W systems. 2) As suggested in Fig 7.1, *Period 2* can also occur in our case. During this period the PEG molecules, particularly for small MW, begin to deposit onto the pore wall slowly increasing the initial layer coverage. As a result, the flux decline can not be observed.

Interestingly, the M+EW system exhibited an increased J_{rf}, indicating a relatively higher fouling resistance under pressure. This reflects that the addition of high concentration of ethanol can not absolutely eliminate the PEG adsorption; PEG adsorption would happen and even

increase with the applied pressure. This observation is supported by reported findings in literature.[13-15] It has been discussed that the presence of ethanol could weaken the PEG adsorption on the hydrophobic surface or could postpone its occurrence to a higher PEG concentration.

Furthermore, we measured the relative filtrate flux reduction (J_{rv}) during ultrafiltration as denoted by the triangle symbols in Fig. 7.4. Note that J_{rv} is a filtrate flux reduction relative to the corresponding pure solvent as determined by eq. 7-6. The M+W and HM+W systems showed little or no difference in J_{rv} relative to the flux of pure water J_{rf}. A significant change was found between J_{rv} and J_{rf} in the M+EW system. This might be due to concentration polarization.

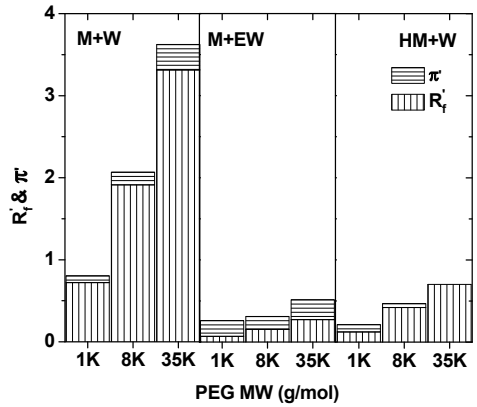

Figure 7.7 Relative fouling resistance (R'_f, black) and relative osmotic pressure resistance (π', red) during the ultrafiltration of 1g/L PEG solutions in the 3 systems: M+W (left), M+EW (mid) and HM+W (right).

The total filtrate flux reduction J_{rv} as shown in Fig. 7.4 is a combined result of both membrane fouling resistance (R_f) and osmotic pressure resistance ($\sigma\Delta\pi$). In Figure 7.7, the experimental data of J_{rf} and J_{rv} from Fig. 7.4 were transformed into the relative fouling resistance R'_f by eq. 7-8 and the relative osmotic pressure resistance (π') by combining eqs. 7-6, 7-8 and 7-9. Overall, fouling resistance R'_f in the M+W system is significantly higher than the other systems while the osmotic pressure resistance π' is small in all the systems. The severe filtrate flux decline in the M+W system is mainly due to the big fouling resistance. Even with the negligible concentration polarization, an increasing osmotic contribution can be still observed as PEG molar mass increases. This is consistent with extensive discussions in many publications.[16] For the M+EW system, the filtrate flux was somewhat decreased due to both the fouling and osmotic pressure

resistance. Since the fouling resistance is low in this system, the π' became comparable to the R'_f thus causing an observable increase in J_{rv} relative to J_{rf} as already shown in Fig. 7.4. For the HM+W system, the filtrate flux decline is mainly caused by some extent of PEG adsorption.

7.3.2. Ultrafiltration of single PEGs—filtrate flux

The rejection characteristics of the nanoporous 1,2-PB membranes were evaluated by ultrafiltration experiments with a series of single PEG molecules over a large range of solute size for the three systems at 0.5, 1.0 and 1.5 atm pressures.

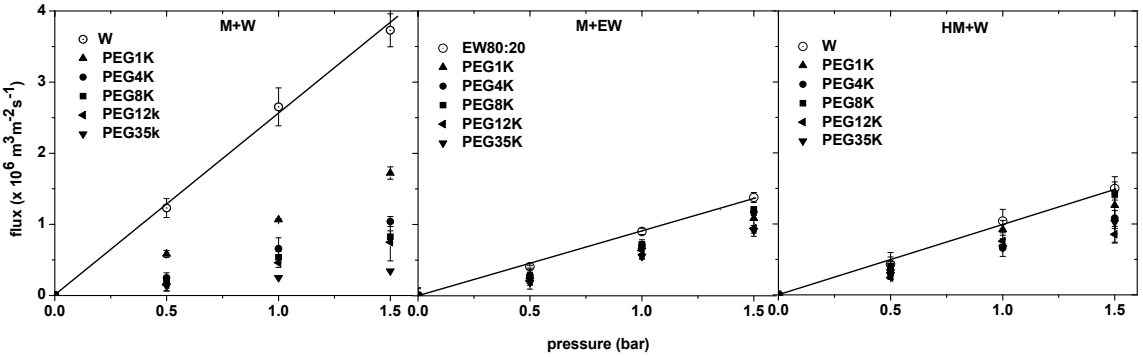

Figure 7.8 Flux as a function of the applied pressure in 3 different systems: left. M+W, mid. M+EW, right. HM+W for both filtrate solutions of PEG molecules with various molar mass and pure solvent. Concentration of the single PEG solutions is 1g/L.

Figure 7.8 shows (within experimental uncertainty) a linear dependence of filtration flux on the applied pressure for each PEG molecule in all the systems. However, a significant flux decline relative to the pure water flux was observed in the M+W system. As discussed previously, this is caused by a fast built-up of the adsorption fouling in the M+W system at the outset of filtration, independent of pressure up to 1.5 bar. We can conclude that at pressures up to 1.5 bar, concentration polarization has little effect and membrane fouling is independent of the applied pressure in the three systems.

7.3.3. Ultrafiltration of single PEGs— rejection profiles

Figure 7.9 compares the observed rejection data Rej_{obs} versus r_s / r_p obtained at a constant pressure of 1 bar for the three systems: M+W, M+EW and HM+W. r_s / r_p is the ratio of

hydrodynamic radius of the solute (See Table 7.1) to the effective pore size (5 nm for the hydrophobic membranes and 4 nm for the hydrophilic membranes, see chapter 5.3.2). The solid curves in Fig. 7.9 are the actual rejection coefficient Rej_{actual} at experimental flux rates of corresponding filtrate solutions, as predicted by eq. 7-11 without taking the concentration polarization (eq.7-13) into account.

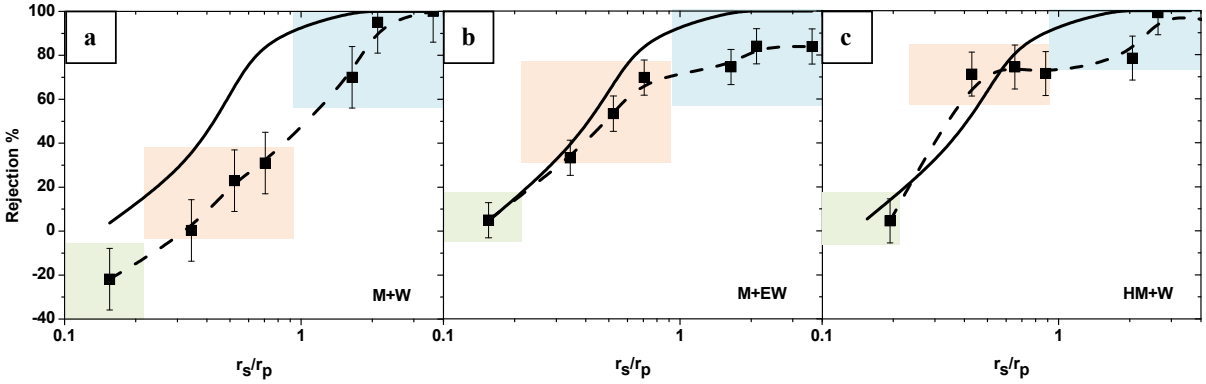

Figure 7.9 The observed rejection (Rej_{obs}) of single PEG solutions vs. r_s/r_p at applied pressure 1 bar; a. M+W, b. M+EW, c. HM+W. The solid curves are the actual rejection at each experimental filtrate flux rate as calculated from eq. 7-11, without taking concentration polarization into account.

The M+W system showed a rejection Rej_{obs} significantly below the predicted actual rejection in the range of PEG MW from 1 kg/mol to 35 kg/mol. Particularly, permeate concentrations higher than feed concentrations were observed for PEG1K and PEG4K. We believe that the large adsorptive fouling is the main reason causing the reduced rejection. For PEG1K and PEG4K ($r_s < r_p$), molecules could easily enter the pores and deposit onto the pore walls as the solvent passes through the membrane as depicted in Figure 7.10a.

A dense adsorption layer is expected to be formed on the interior surface. As a consequence of the nanoporous polymer's large specific surface area, a concentration of ~ 180 g/L inside the pore could be reached as estimated by the mass gain of static PEG adsorption. This value is two orders of magnitude higher than the feed solution concentration of 1g/L. Such big concentration gradient strongly drives PEG to depart from the pore wall to the permeating solution, giving rise to the results of $c_p > c_f$ for these small PEG molecules. Surface adsorption, from the thermodynamics perspective, supports therefore the occurrence of $c_p > c_f$. From the kinetics point of view, a quick build-up of the equilibrium adsorption (due to the small membrane

thickness and small pore volume relative to feed volume) is a key factor so that a stable source is available to provide extra PEG molecules as the filtration solution passes through the pores. For small molecules, the equilibrium adsorption (no pressure) is comparable to flow-induced adsorption. The diffusivity of large molecules is low and the rejection is high at the membrane surface, which would cause a higher concentration on the membrane surface[1]. Therefore the phenomenon $c_p > c_f$ was not observed for molecules larger than PEG4k. More serious concentration polarization for large molecules e.g. PEG12K and PEG35K resulted in a certain decrease in rejection as shown in Fig. 7.9.

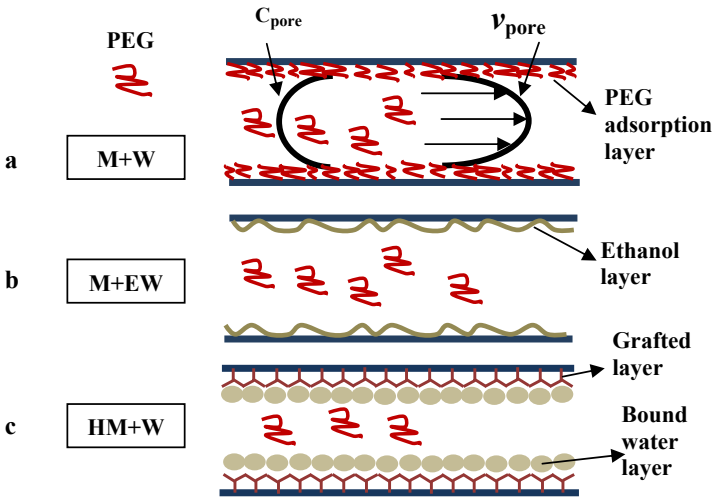

Figure 7.10 Proposed qualitative models for interpreting the observed rejection behaviors in the three systems a. M+W; b. M+EW; and c. HM+W.

The M+EW system followed much better the calculated actual retention. As revealed by Figs. 7.4 and 7.7, no significant PEG adsorption was found in the M+EW system due to the presence of high concentration of ethanol. Therefore, the observed rejection of this system more truly reflects the intrinsic size rejection property of the nanoporous membrane (Figure 7.10b). The observed rejection of small PEG molecules perfectly fit to the actual rejection while it becomes slightly below the actual rejection with molar mass increase, which is probably due to increased concentration polarization.

The HM+W system showed a sharp variation between 1K and 4K. Above 4K, the rejection profile slowly changed from 80% to 100%. This is due to a big reduction in effective pore size

(Figure 7.10c) as confirmed by the significant decline of water flux for the fresh membrane (See chapter 5.3.2).

For all the three systems, the observed rejection is somehow below 100% for large PEG molecules with $r_s / r_p >> 1$, e.g. PEG 56K and PEG100K. The reason is not clear. The filtration flux for these large molecules is much less than the critical flux as described in literature[17,18]. Therefore permeation of these large molecules would not be expected in the present conditions. Possible defects in the membranes can not be excluded in this case, apparently more in the M+EW system. In addition, the polydispersity of PEGs with high molecular weights may ease the filtration for lower MW fraction of PEG molecules.

7.3.4. Ultrafiltration of single PEGs– sieving vs. flux rates

In order to have additional insights into the retention characteristics of the nanoporous membranes, ultrafiltration of single PEGs were conducted under different pressure thus enabling varying filtrate flux rate. Figure 7.11 presents the observed sieving coefficient vs. the filtrate flux for experiments performed at 0.5 bar, 1 bar and 1.5 bar. Three different systems, M+W, M+EW, and HM+W are compared for each PEG molecule. For M+EW system, we can observe a clear decrease with increasing filtrate flux for all the PEG molecuels. This is due to the reduction in the contribution of PEG diffusion through the membrane relative to PEG convection. This behavior has been extensively discussed in many publications[4]. Usually, in a wide range of filtrate flux, the sieving coefficient will then pass through a minimum before increasing at high filtrate flux. The latter behavior mainly arises from concentration polarization effects, but it did not occur within the limit measurement range in our study. This observation, on the other side, well supports the results discussed in Figs. 7.7 and 7.9.

For the systems M+W and HM+W, we could not see any clear or significant change tendency of sieving with increasing flux rate. With the consideration of measurement error, HM+W system gave more or less the same sieving behavior at the three filtrate flux rates. As we discussed in Fig. 7.9, a smaller effective pore size give rise to a higher intrinsic retention, thus the sieving behavior relies less on the filtrate flux, particularly in the limit flux range given in our study. For M+W system, it is obvious that the nanoporous membranes have no ability to retain the PEG1K and PEG 4K at feed side. Sieving coefficients slightly increase with flux rate in the

case of PEG1K and PEG4K. As the filtrate solution passes through the pores, it can sweep more adsorbed molecules away from the pore walls at higher flux rate, and as a consequence, a higher permeate concentration at high flux rate is observed. A gentle decrease occurred in the case of PEG8K and PEG12K.

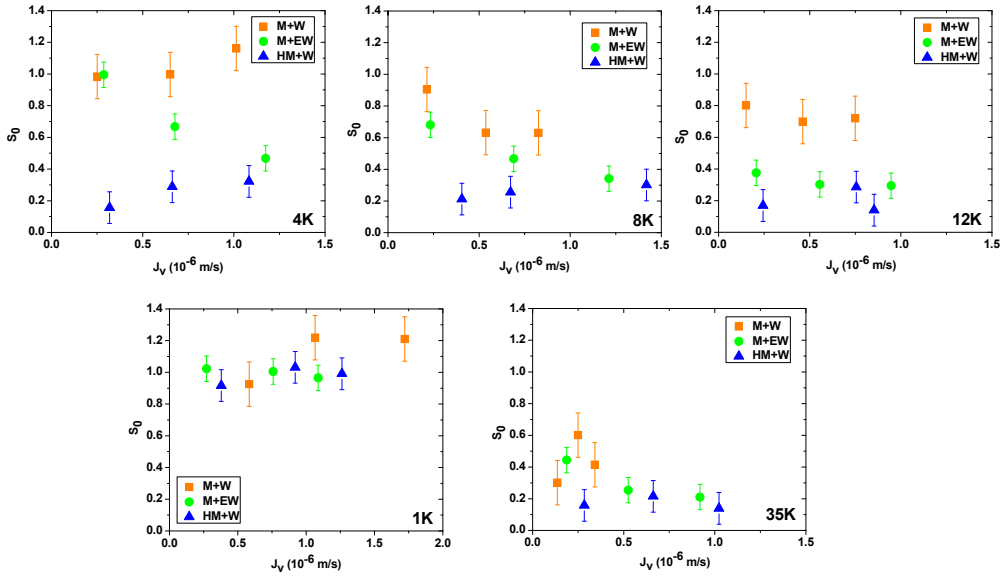

Figure 7.11 Observed sieving coefficients vs. filtrate flux for PEGs ultrafiltration through the nanoprous 1,2-PB membranes in different systems: M+W, M+EW and HM+W.

7.3.5. Ultrafiltration of mixture PEGs

Finally we challenged the three systems with a mixture of PEG molecules (PEG1K – PEG35K) at a concentration 1 g/L under 1 bar. The similar rejection properties were observed as displayed in Figure 7.12. At this stage we can not give a clear explanation for the rejection lower than 100% retention at PEG 35K.

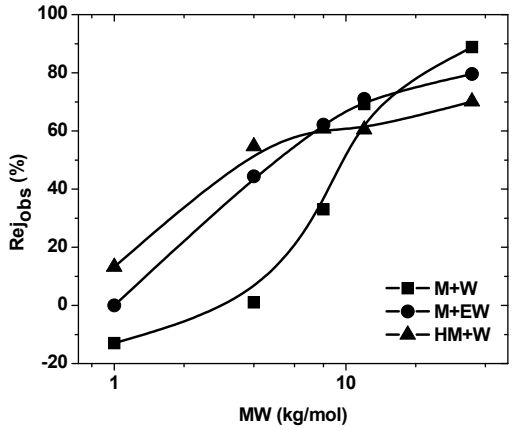

Figure 7.12 Rejection profiles vs. molecular weight for mixture of PEG ultrafiltration through the nanoporous 1,2-PB membranes in different systems: M+W, M+EW and HM+W.

7.4. Conclusions

Block copolymer templated nanoporous 1,2-polybutadiene membranes with uniform pores of 10 nm in diameter were developed for ultrafiltration applications. A series of PEG molecules were used to explore the effects of membrane fouling on the flux decline and rejection profiles. A significant filtrate flux decline occurred through the hydrophobic membrane, mainly due to adsorptive fouling. The presence of high concentration of ethanol in the filtration solution resulted in a negligible PEG adsorption under static condition; however some membrane fouling appeared when pressure was applied. The hydrophilized membrane diminished the membrane fouling thus effectively suppressing the flux reduction. The effect was insensitive to the pressure applied (0.5 – 1.5 atm). The observed rejection of PEG was compared with theoretical predictions based on size effects and hydrodynamic effects alone, as described by the Bungay-Brenner model. The model satisfactorily described the case of hydrophobic membranes in the presence of ethanol. In this case, no significant fouling occurred thus maximally reflecting the intrinsic sieving property of the UF membrane. A significantly reduced rejection relative to model expectation was found for the hydrophobic membrane in water due to the severe surface

adsorption. We may take advantage of the selective adsorption as an alternative separation mechanism in some applications, for example affinity membrane absorbers in hemodialysis. For the hydrophilized membrane the molecular weight cut off shifted to lower MW range i.e. between 1 kg/mol and 4 kg/mol, due to the reduction of pore size. This is very attractive for the separation of low MW species. It can be concluded that solvent property and surface chemistry have critical effect on UF performance in both flux and selectivity. It is possible to attain tunable UF performance for specific applications by use of nanoporous 1,2-PB membranes under different conditions.

At present, we prepared the free membranes with thickness of 25 μm. Such thick membranes result in lower permeation rate compared with commercial membranes. Therefore making a composite membrane with the nanoporous membrane as a thin selective top layer will be a necessary route to enhance the values of the nanoporous membranes in relevant UF applications.

7.5. References

[1] M. Mulder, Basic principles of membrane technology, 2ed ed., Kluwer Academic, Netherlands 1996.

[2] W. M. Deen, Hindered transport of large molecules in liquid-filled pores. AIChE J. 33 (1987) 1409–1425.

[3] P. M. Bungay, H. Brenner, The motion of a closely fitting sphere in a fluid-filled tube. Int. J. Multiph. Flow 1 (1973) 25–56.

[4] L. J. Zeman, A. L. Zydney, Microfiltration and ultrafiltration: principles and applications, Marcel Dekker, New York, 1996.

[5] G. Belfort, R. H. Davis, A. L. Zydney, The behavior of suspensions and macromolecular solutions in crossflow microfiltration, J. Membr. Sci. 96 (1996) 1–58.

[6] N. Nagata, K. Herouvis, D.M. Dziewulski and G. Belfort, Cross-flow membrane microfiltration of a bacterial fermentation broth, Biotechnol.Bioeng., 44 (1989) 161–181.

[7] Th. F. Hesselink, Adsorption of polyelectrolytes from dilute solution, in G. Parfitt and C.H. Rochester (Eds.), Adsorption from Solution at the Solid / Liquid Interface, Academic Press, New York, NY, 1983, pp. 377– 412.

[8] P. Szewczykowski, Nano-porous materials from diblock copolymers and its membrane application, Ph.D. thesis, Technical University of Denmark, 2009.

[9] S. Lentsch, P. Aimar, J. L. Orozco, Separation albumin-PEG: transmission of PEG through ultrafiltration membranes, Biotechnology and Bioengineering 41(1993) 1039–1047.

[10] J. D. Bloustine, Experimental investigations into interactions and collective behavior in protein/polymer mixtures and granular gods, Ph.D. thesis, Brandeis University, Waltham, Massachusetts, 2005.

[11] R. W. Baker, Membrane technology and applications, 2nd ed., John Wiley& Sons, Ltd., Chichester, 2004.

[12] H. Susanto, S. Franzka, and M. Ulbricht, Dextran fouling of polyethersulfone ultrafiltration membranes—Causes, extent and consequences, J. Membr. Sci. 296 (2007) 147–155.

[13] R.Shukla, M.Cheryan, Performance of ultrafiltration membranes in ethanol–water solutions: effect of membrane conditioning, J. Membr. Sci. 198 (2002) 75–85.

[14] D. R. Machado, D. Hasson, R. Semiat, Effect of solvent properties on permeate flow through nanofiltration membranes. Part 1: investigation of parameters affecting solvent flux, J. Membr. Sci. 163 (1999) 93–102.

[15] S. K. Zaidi, A. Kumar, Effects of ethanol concentration on flux and gel formation in dead end ultrafiltration of PEG and Dextran, J. Membr. Sci. 237 (2004) 189–197.

[16] G. Jonsson, Selectivity in membrane filtration, Desalination 51 (1984) 61–77.

[17]F. Jin and C. Wu, Observation of the first-order transition in ultrafiltration of flexible linear polymer chains, Physical review letters 96 (2006) 237801.

[18] P.G. de Gennes, Flexible polymers in nanopores, Adv.in Polymer Science 138 (1999) 91-105.

Chapter 8 SDS Loading and Release in Nanoporous 1,2-PB Membranes

As we introduced in chapter 2.5, nanoporous membranes with large surface-volume ratio, well-controlled pore size offer an attractive route for making capsules that may provide controlled release of pharmacologic or biologic reactive agents. Our effort to explore the potential of the nanoporous 1,2-PB membranes as a sustainable-release carrier is the main focus of this chapter. Amphiphilic molecule, sodium dodecyl sulfate (SDS) is selected as a model molecule for studying the loading and release in the nanoporous membranes. In addition, surface modification via SDS physisorption is also an important objective of this work. The infiltration of SDS to an original hydrophobic nanoporous membrane is examined by gravimetry and complementarily confirmed by XPS. SDS adsorption isotherm is discussed in terms of the Langmuir model. Incorporating SDS imparts water wettability to the originally hydrophobic nanoporous membranes. We will show results on the water wetting kinetics and the release kinetics of SDS in the presence of excess water or methanol. This part of work has been published in *Langmuir 2010, 26(16), 13457–13465*.

The second part of work in this chapter deals with the preliminary anti-biofilm tests. The aim is to give a preliminary demonstration on the use of SDS-infilled nanoporous films as a sustainable-release carrier. The SDS-infilled nanoporous membrane was kept in contact with mediums containing two different bacteria. We attempted to challenge the effectiveness of SDS-infilled nanoporous membrane in inhibiting bacterial attachment and biofilm formation on its surface via sustainable releasing SDS.

8.1. Background

8.1.1. Capillary filling

Capillary filling is, mostly, dominated by capillary effect due to the large surface-to-volume ratio. This phenomenon occurs because the interfacial energy of the pore wall–water interface is much lower than that of the pore wall–air interface, i.e. $\gamma_{sv} > \gamma_{sl}$. The free energy reduction on surface wetting is balanced by the potential energy gain by the liquid rising in a gravitational field. If the pore wall shows good wettability to the liquid, i.e. the meniscus is concave, the liquid is expected to be pushed up the wall (called capillary rise) (Figure 8.1a). If the liquid is non-wetting on the wall due to the low surface energy of the wall, a convex surface would be formed (Figure 8.1b). Hence, a negative capillary effect is observed in this case.

(a) **(b)**

Figure 8.1 Schematic representation of the capillary phenomenon: (a) Capillary rise and (b) Capillary depression.

Capillary phenomena were first studied quantitatively by Lucas and Washburn in the early twentieth century. [1,2] They found that in case of a fully wettable capillary, capillary rise height is proportional to the square root of time, as described by

$$l(t)^2 = \frac{\gamma r \cos\theta t}{2\mu} \qquad (8\text{-}1)$$

where r is the capillary radius, γ the liquid surface energy, θ the contact angle, t the time and μ the viscosity of the liquid.

8.1.2. Surfactants

Surfactants are amphiphilic molecules that consists of a non-polar hydrophobic portion, usually a linear or branched hydrocarbon or fluorocarbon chain containing 8–18 carbon atoms, which is attached to a polar or ionic portion (hydrophilic).[3] As dissolved in aqueous environment, surfactants with polar heads (that tend to dissolve in water) and non-polar tails (that tend to dissolve in oil or stick out into air) have the tendency to strongly adsorb and orientate on interfaces. The adsorption of ionic surfactants on hydrophobic surfaces such as carbon nanotubes, polymer surfaces, etc. is governed by hydrophobic interaction between the alkyl chain of the surfactant and the hydrophobic surface.

In addition to the surface adsorption properties of surfactants, they also have the remarkable ability to self-assemble in aqueous solution. The self-assembled structures called 'micelles' in solution are created to reduce the exposure of the hydrocarbon chains to water. In the micelle, the surfactant hydrophobic groups are directed towards the interior of the aggregate and the polar head groups are directed towards the solvent. The driving force behind micellization is the entropic effect, that is, there is a positively entropic increase in water molecules when the surfactants associate to form micelles due to hydrophobic effect. These micelles are in dynamic equilibrium and the rate of exchange between a surfactant molecule and the micelle may vary by orders of magnitude.

8.1.3. Biofilm

A biofilm is an aggregate of microorganisms in which cells adhere to each other and/or to a surface. These adherent cells are frequently embedded within a self-produced matrix of extracellular polymeric substance, which is generally composed of extracellular DNA, proteins, and polysaccharides. Biofilms may form on living or non-living surfaces and can be prevalent in natural, industrial and hospital settings.[4]

In nature, microorganisms usually attach to solid surfaces, especially on the liquid–solid interface. After attachment, they form microcolonies, produce extracellular polymeric substances, entrapdebris and other species of cells, and form biofilm.[4] Biofilm is very resistant to antibiotics and some physical treatments and it is also a serious problem for infectious disease. Biofilm is also a potential hazard in food processes, water treatment, ships and etc.[5]

Biocides and disinfectants have been the principal weapons used to control unwanted biofilms such as those that foul cooling water towers, oilfield produced water pipelines, or food processing plants.[5] These agents work by inhibiting the growth of microorganisms. Furthermore, in many systems where problematic biofilm fouling occurs, the desired end result is a clean surface rather than an inactive yet physically intact biofilm. Antimicrobial agents may achieve this indirectly by stopping growth and allowing the natural detachment process to slowly remove the biofilm. The anionic surfactant SDS has been reported to exhibit bactericidal activity against numerous bacteria and effectively detach the inactive biofilm.[6] An in-depth discussion of biofilm and an overview of approaches to detach and inhibit biofilms are out of scope of this thesis.

8.2. Experimental

We used two different polymer films in this study. One is non-porous cross-linked 1,2-polybutadiene (1,2-PB) film that was made of 1,2-PB homopolymer (weight-average molecular weight $\langle M_w \rangle$= 12.5 kg/mol, polydispersity index PDI=1.05). The 1,2-PB homopolymers were cross-linked as the same procedure used for block copolymers (chapter 3.2). The cross-linked 1,2-PB films were only used for the contact angle measurements in relation to surface tension investigation. Nanoporous 1,2-PB film was prepared by solvent casting the 1,2-PB-*b*-PDMS (BD14 batch) solution onto a glass petri-dish. The preparation process has been in detail described in chapter 3.2. The top side of the cast precursor film was exposed to N_2 during cross-linking. Thus, a thin skin-layer is expected to form on the free surface. For comparison, we also prepared one 1,2-PB-*b*-PDMS sample by sandwiching between two glass petri-dishes for cross-linking, thereby eliminating the free surface. Under this condition, non-skin nanoporous film is formed as a result. The thickness of the nanoporous films is approximately 500 μm. They were cut to square pieces with a mass differing within ± 5% of a target value for the following experiments. In this study, nanoporous samples used for loading and adsorption isotherm experiments were prepared from the same batch of cross-linked samples.

8.2.1. SDS loading and release in nanoporous 1,2-PB membranes

Preparation of surfactant solutions. Sodium dodecyl sulfate (purity ≥98.5%, Sigma-Aldrich), was used as received. We prepared SDS solutions in de-ionized (DI) water and stirred on a shaker at room temperature for at least 15 h before use. Molar concentrations in the range 0.5 mM – 50 mM were used for the SDS loading experiments.

Loading of SDS aqueous solutions. In the SDS loading experiment, each piece of nanoporous 1,2-PB film (20 ± 1 mg) was placed in 15 ml of SDS aqueous solution and kept under shaking at planned time intervals. The solution loading rates for different SDS concentrations were followed by gravimetry. Each sample was taken out of the solution, gently wiped with a tissue, immediately weighed in a balance with precision 0.1 mg and placed back to the solution for the next time interval. At the end of the loading experiment, the outer surface of the sample was wiped with a tissue and dried under nitrogen flow without further treatment. The mass of the SDS-loaded film was notified after complete drying.

SDS adsorption isotherm in the nanoporous films. We dipped the nanoporous 1,2-PB films in methanol for 1 h to completely prewet the surface. Subsequently, the prewetted samples stayed in the SDS aqueous solutions of different concentrations for 7 days that was tested as an abundantly sufficient time for equilibrium loading at the tested concentrations. The SDS-loaded samples were completely dried under nitrogen flow after the loading. The amount of adsorbed SDS was determined by gravimetry.

SDS release in water and in methanol. We first prepared 30 SDS-loaded samples by following the procedure described above. Each nanoporous sample was placed in 15 ml of 10 mM SDS aqueous solution for 24 h that was a sufficient time for equilibrium loading at 10 mM. They were then completely dried under nitrogen flow before starting the release experiment. 22 of the SDS-loaded samples were used for the measurement of SDS release kinetics in water and the remaining 8 for the release kinetics in methanol, as follows. Each SDS-loaded sample was immersed in 300 ml of DI water (or methanol) on a shaker for a planned time interval. The amount of SDS released from each sample was determined by the difference between the dry masses of the sample before and after release. The kinetics of water uptake into two of the dry SDS-loaded samples was also monitored gravimetrically.

Contact angle measurement (CA). CA was performed at 25 °C in a Contact Angle System OCA 20. The surface tension (γ_{lv}) of SDS aqueous solutions was measured by the pendant drop method.[7] Contact angle (θ) of SDS aqueous solutions on the cross-linked 1,2-PB substrates were measured by the sessile drop method.[7]

X-ray photoelectron spectroscopy (XPS). The SDS infiltration in the film was also determined by XPS. A SDS-loaded sample was cut with a blade and the cut surface was trimmed flat on an ultramicrotome. Thereafter we examined the freshly exposed surface by XPS on a Surface Science Instruments Sage-100 with a monochromated Al Kα X-ray. Elements present on the surface were identified from a survey spectrum over the energy range 0-1400 eV with pass energy of 100 eV and resolution of 0.5 eV. The spectrum was analyzed with the software Avantage provided by the manufacturer.

8.2.2. Anti-biofilm demonstrations by SDS-infilled nanoporous 1,2-PB membranes

The SDS-infilled nanoporous films were evaluated in biofilm inhibition tests. The tests were designed and performed by Postdoc. Liang Yang at DTU-BIO. Two different biological materials were used in the tests, Escherichia coli Sar18 (*E.coli*) and Staphylococcus epidermidis RP62A (*S. epidermidis*).

Biofilm inhibition assay. SDS-loaded films were first glued on glass slides with the non-skin surface faced to air. Original nanoporous films without SDS infiltration were used as control samples. They were submerged into bacterial cultures in petri-dishes as shown in Figure 8.2.

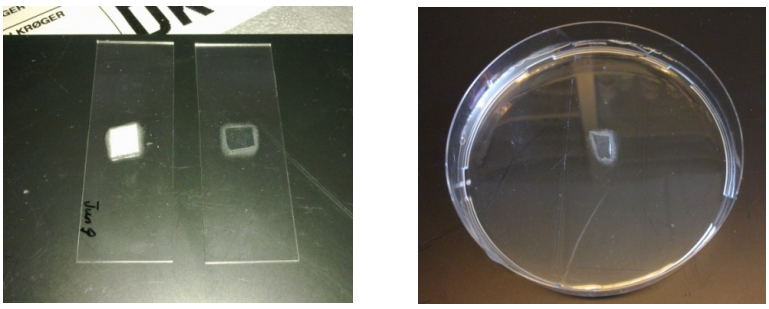

Figure 8.2 Left: photographs of a SDS-loaded sample (white) and a control sample (transparent), both are glued on glass slides; Right: a glued sample is submerged in a bacterial culture medium.

Bacteria were cultivated in AB minimal supplemented with 30 mg glucose l–1 at 37 degree for 24 hours. Thereafter the sample slides were taken out from the petri-dishes and submerged into distilled water to wash away the unattached bacterial cells. Then the film samples were observed under Carl Zeiss LSM510 META Confocal Laser scanning Microscopy (CLSM) for biofilms. The LIVE/DEAD ® Bacterial Viability Kit was used to determine live (appears green) and dead (appears red) bacterial cells. Images were obtained using a 63x/1.4 objective. Simulated three-dimensional images and sections were generated using the IMARIS software package (Bitplane AG).

8.3. Results and discussion

8.3.1. Polymer films

The nanoporous 1,2-PB film was characterized by SAXS and N_2 adsorption in previous work.[8] The pore diameter was approximately 15 nm and the specific surface area was $A_{spec} = 278 \pm 40$ m^2/g. The specific volume of the nanoporous sample was $v_{spec} = 0.79$ cm^3 per gram of polymer, as evaluated by methanol uptake.[9] Figure 8.3 is a photograph of three types of dry films: cross-linked non-porous 1,2-PB (left), nanoporous 1,2-PB (middle) and SDS-loaded nanoporous 1,2-PB films (right). The cross-linked homopolymer 1,2-PB and the native nanoporous 1,2-PB film are transparent, whereas the SDS-loaded nanoporous sample is translucent, probably due to the 2-d crystalline packing of SDS onto the pore-wall surface.

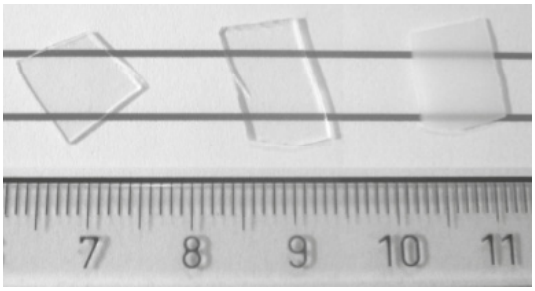

Figure 8.3 A photograph of a cross-linked homopolymer 1,2-PB film (left) and nanoporous 1,2-PB films before (mid) and after (right) loading with SDS.

Due to our technique limitation we cannot directly probe the interior surface of nanoporous 1,2-PB film, therefore its surface and interface energies were estimated by contact angle measurements on the surface of non-porous cross-linked 1,2-PB homopolymer substrates.

Figure 8.4a illustrates the trend of surface tension of water γ_{lv} with different SDS concentrations. The critical micelle concentration (CMC) was determined to be 8.1 mM, similar to reported vaules.[10] Figure 8.4b shows the contact angle θ of solutions with varying SDS concentration on the cross-linked 1,2-PB substrate. It diminishes with SDS concentration and shows a slight change above 6 mM. The corresponding interfacial tension γ_{ls} also shown in Fig. 8.4b was calculated according to the Young's equation $\gamma_{ls} = \gamma_{sv} - \gamma_{lv} \cdot \cos\theta$. The value of the surface tension γ_{sv} of cross-linked 1,2-PB film was determined to 24 mN/m by extrapolating to $\cos\theta = 1$ in a plot of $\cos\theta$ against γ_{lv}. One γ_{sv} literature value of 25 mN/m was found for 1,2-PB.[11] As shown in Fig. 8.4b, the contact angle of pure water on the cross-linked 1,2-PB substrate was above 100°; while 90° (critical angle) can be reached at a SDS concentration of ~ 2.4 mM.

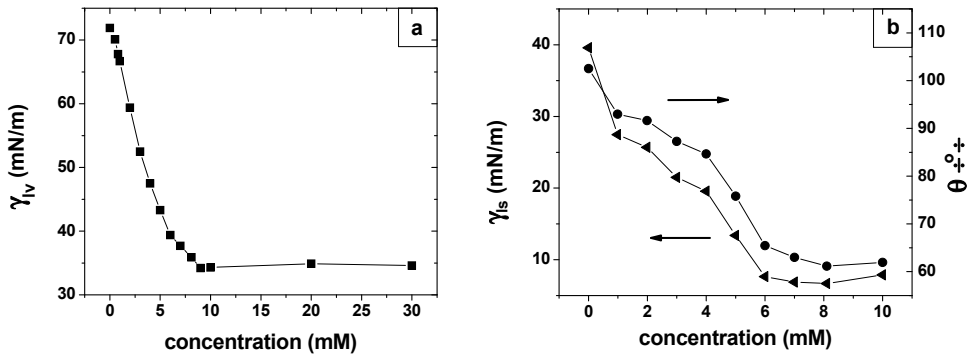

Figure 8.4 (a) Surface tension of water γ_{lv} as a function of SDS concentration; (b) Contact angle θ of SDS aqueous solutions on the cross-linked 1,2-PB substrates versus SDS concentration (circles, right) ; the resultant interface tension γ_{ls} deriving from $\gamma_{ls} = \gamma_{sv} - \gamma_{lv} \cdot \cos\theta$ (triangles, left).

The behavior of SDS on the non-porous substrate was assumed to be valid for the nanoporous samples. SDS, as an amphiphilic molecule, tends to adsorb and orient on the interface to reduce the free energy. The long hydrocarbon chain of SDS in water is likely to attach onto the hydrophobic substrate via hydrophobic interaction, while the hydrophilic head leans to expose to aqueous environment.[12-14] The driving force for the loading of a liquid in capillary systems is

capillary force, which depends on the liquid/solid interface tension γ_{ls}. Most aqueous solutions are rejected from the hydrophobic nanoporous 1,2-PB films. However, it is possible to fill surfactant solutions to the nanopores since the interfacial energy can be reduced by surfactant adsorption.

For the nanoporous 1,2-PB, however, one end-group -Si(-)-F per chain is expected to remain after removal of PDMS.[15] The surface density of -Si(-)-F was estimated to 0.26 nm^{-2}, or 5.2% relative to the 1,2-PB repeating units exposed to the surface.[16] These groups are expected to lower the surface energy for the nanoporous samples compared to the pure 1,2-PB cross-linked substrates. Therefore we expect the critical contact angle of 90° to be reached at a higher concentration than 2.4 mM, where the capillary rise would start as a consequence.

8.3.2. Loading of SDS aqueous solution: kinetics

We investigated the kinetics of the liquid uptake process for different initial bulk concentration c_b of SDS aqueous solutions in the range $0.5\ \text{mM} < c_b \leq 50\ \text{mM}$. The *loading* is defined as the amount of SDS solution uptaken in the nanoporous film relative to the original mass of the film, i.e.

$$loading = (m_{wet} - m_{PB}) / m_{PB} \qquad (8\text{-}2)$$

Here m_{wet} is the wet mass of the nanoporous film measured at a certain time, and its original mass is $m_{PB} = 20 \pm 1$ mg. Note that there was noticeable decrease in the concentration of the SDS solution surrounding the polymer due to SDS adsorption onto the large specific surface area of the nanoporous film. For example, for the solutions with initial concentrations $c_b = 5$ mM and $c_b = 8.1$ mM, the concentrations decreased to 4.4 mM and 6.9 mM, respectively, after 7 days of loading.

We divided the results of loading as a function of time for a period of 7 days into two panels depending on c_b. Figure 8.5a shows loading profiles for c_b around CMC (8.1 mM), referred to as the CMC zone. Figure 8.5b shows profiles for c_b either well below or well above CMC. It is

evident that at low concentrations ($c_b \leq 4$ mM), nearly no loading of aqueous SDS solutions was detected within the maximum measurement time.

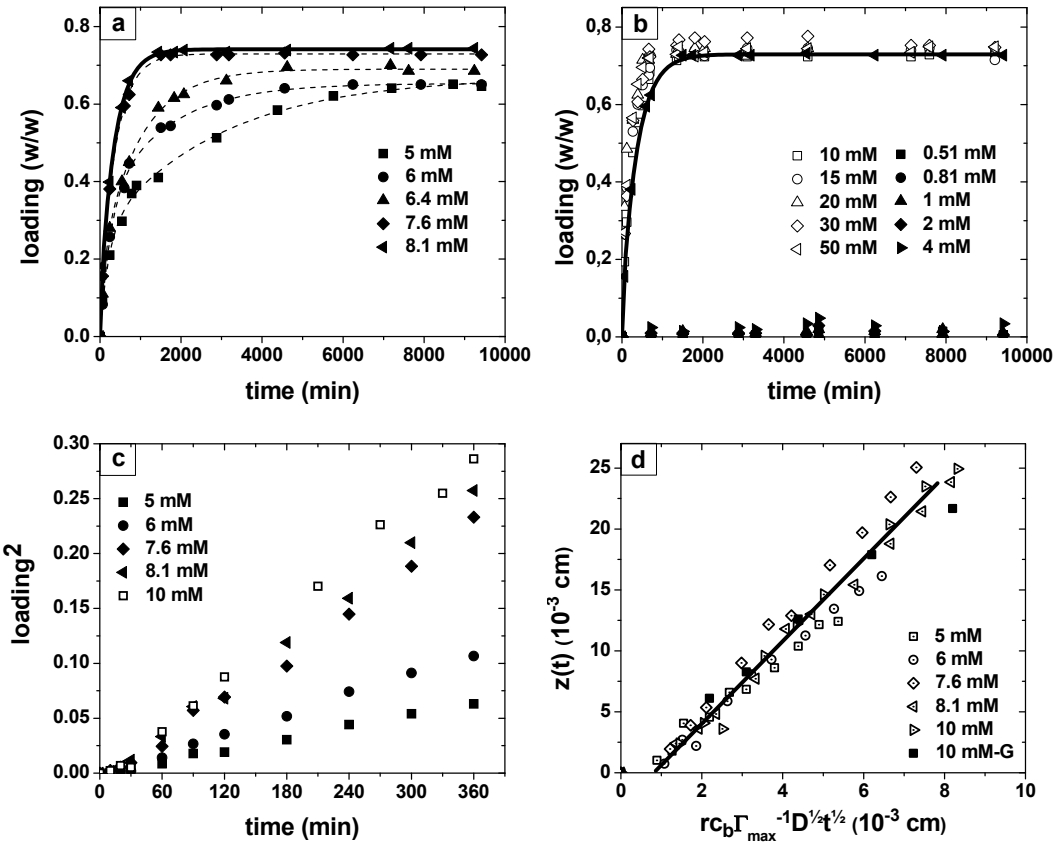

Figure 8.5 Loading of SDS aqueous solution versus time at varying SDS concentration. (a) loading vs. time at the CMC zone; lines denote empirical fittings to experimental data by double exponential functions (see eq. (8-4)); (b) loading vs. time at high concentrations (above CMC) and low concentrations ($\leq$4 mM); the fitting curve at CMC (8.1 mM) is shown in both panels (a) and (b) in order to ease the comparison; (c) the loading profiles plotted as the square of loading vs. time within the initial 6 hours; (d) comparison of the estimated *z(t)* from the experimental data given in Fig. 8.5c with the scaling relation (8-2). The non-zero intercept is due to the existence of an induction period in the data of Fig. 8.5c as discussed in the main text. The sample 10 mM-G was cross-linked sandwiched between two glasses; it is expected to miss the skin layer thus its effective outer surface area of $A \sim 1.6$ cm^2 is bigger than that of the other samples, 0.9 cm^2. The solid line is a linear fitting for visual aid.

In the CMC zone and above CMC, the loading profiles displayed a typical saturation behavior: the loading increased with time but the rate of loading gradually decreased with time, and eventually the loading seemed to reach a plateau value for a given c_b. In the CMC zone, there was a noticeable influence of c_b on the loading kinetics and only a slight influence on the plateau values. At high concentrations (above CMC), loading data for different c_b nearly overlapped. The spontaneous imbibition of a liquid into the pores of a porous medium is driven by the capillary force, which depends on surface wettability. The fact that no loading was found for low SDS concentrations ($c_b \le 4$ mM) thus indicates that the critical contact angle of 90° may have not been reached for these solutions at the entrance of the nano-capillaries. This observation supports the previous argument that the existence of -Si-F on the interior surface of the nanoporous sample caused a lower surface energy, and therefore loading starts at a concentration higher than the value 2.4 mM observed for the cross-linked 1,2-PB hompolymer substrate.

Figure 8.5c shows the loading squared as a function of time for the initial 6 hours; after the very first 15 – 30 s all the data show a good linearity. Such linearity in the short-time limit is expected from the Lucas-Washburn equation for pure liquids.[1,2] However, for the imbibition of surfactant solutions into hydrophobic capillaries, the Lucas-Washburn equation may not be applicable.[17-20] Consider, for instance, the loading of SDS solution at 5 mM where $\gamma_{lv} = 4.3\times10^{-2}$ N/m, $\cos\theta = 0.245$, and $\mu = 10^{-3}$ Pa·s. A direct use of the Lucas-Washburn equation that neglects SDS adsorption predicts an imbibition rate about two orders of magnitude higher than that shown in Figure 8.5d. Alternatively, the linearity between the square of loading and time may result from a diffusion-controlled dynamics.[17, 18]

The imbibition of SDS aqueous solution into hydrophobic capillaries may differ significantly from that of pure liquids.[17-20] As the filling proceeds, the newly formed liquid/solid interface rapidly adsorbs SDS molecules from the liquid/vapor interface (surface adsorption of SDS is fast especially in such confined geometries[21]). This causes a significant decrease of SDS concentration near the advancing liquid front considering the large specific area of nanoporous films.[18] Consequently, the capillary driving force decreases and even vanishes until the loss of surfactant at the advancing liquid front is compensated by diffusion transport from deeper liquid regions. A rigorous theoretical framework for the imbibition of SDS aqueous solution into

hydrophobic capillaries thus should involve the coupling among the dynamic equation of capillary rising, the adsorption/desorption kinetics and the diffusion equation.[18] In the case of strong depletion near the liquid/vapor interface, the following scaling relation

$$z(t) \approx \frac{rc_b}{\Gamma_{\max}}\sqrt{D_\infty t} \qquad (8\text{-}3)$$

has been obtained from mass balance in a quasi-steady state process.[17,18] Here, r is the capillary radius, $\Gamma_{\max}$ is the monolayer capacity of surfactant molecules at the solid/liquid interface, and $z(t)$ is the filling depth. Eq. (8-3) shows that $z(t)$ is proportional to the characteristic diffusion length $\sim \sqrt{D_\infty t}$. In order to estimate $z(t)$ from the loading data in Fig. 8.5c, we modeled the nanoporous film as a bundle of capillaries. The amount of SDS aqueous solution loaded in the nanoporous film is roughly related to $z(t)$ by

$$loading \times m_{PB} \approx A\varepsilon_A z(t)\rho \qquad (8\text{-}4)$$

where A denotes the effective surface area of the film (here we excluded the surface with the skin layer); ε_A is the surface porosity 40% ± 5%, and ρ is the liquid density. It is likely that eq. (8-4) overestimates $z(t)$ because the amount of SDS adsorbed onto the capillary walls was not considered. However, this should not violate the scaling relation $z(t) \sim loading \sim t^{0.5}$ since the amount of adsorbed SDS should also be proportional to $z(t)$.

A reasonable agreement was found between our experimental results shown in Fig. 8.5c and the scaling relation in eq. (8-3). This is demonstrated in Fig. 8.5d. It is evident that on a plot of $z(t)$ vs. $(rc_b / \Gamma_{\max})\sqrt{D_\infty t}$, the loading curves for different c_b nearly collapsed onto a single curve with a nearly linear part. The linear part seems to occur after an induction period which is also noticeable in Fig. 8.5c. However, whether in the induction period $z(t)$ grows linearly with time in the same manner as predicted by Tiberg and co-workers[18] is not conclusive from our data. The following parameters were used in preparing Fig. 8.5d: liquid density ρ = 1 g/cm^3, capillary radius $r = 7.5$ nm, surface porosity ε_A = 0.4, monolayer capacity Γ_{max} = $2.9 \cdot 10^{-10}$ mol/cm^2 estimated from the adsorption isotherm study (to be addressed), and the diffusion coefficient of SDS at 25 ℃ in aqueous solution D_{SDS} = $7.8 \cdot 10^{-10}$ m^2/s.[22] The effective outer surface area of the tested film with skin layer is estimated to be 0.9 cm^2 and is significantly

lower than the overall surface area ($1.6\ \mathrm{cm}^2$) due to the presence of skin layer. As a control test, we also investigated the loading kinetics at $c_b = 10$ mM of a film without skin layer (and thus $A \approx 1.6\ \mathrm{cm}^2$). The results as shown in Fig. 8.5d (filled squares) nearly collapsed with the results for films with skin layers, indicating that the loading through the side with skin layer was negligible.

Empirically, the full-time loading curves in the CMC zone (Fig. 8.5a) and above CMC (Fig. 8.5b) were very well fitted by double exponential functions of the form:

$$loading = a_0 - a_1 e^{-t/t_1} - a_2 e^{-t/t_2} \qquad (8\text{-}5)$$

with five fitting parameters (a_0, a_1, t_1, a_2 and t_2). In the case of $c_b = 8.1$ mM, we got $a_0 = 0.74$, $a_1 = 7.8\times10^{-2}$, $a_2 = 0.66$, $t_1 = 2.7\times10^{-9}$ min, and $t_2 = 358$ min, suggesting that eq. (8-5) could be simplified to a single exponential function, i.e. $loading \approx a_0 - a_2 \exp(-t/t_2)$. This is equivalent with a single time-scale (t_2) describing the entire loading process. The data fitting by a single exponential, however, was not satisfactory (statistical R^2 < 0.99) for the two lower concentrations (5.1 mM and 6 mM). The long time-scale t_2 from fitting, characterizing the diffusion controlled dynamics, varied from 3000 min (at 5.1 mM) to about 200 min (at $c_b \geq 15$ mM).

The loading curves for SDS concentrations well above CMC (c_b > 15 mM) show substantial overlap. This approximate kinetic overlap means that (a) the SDS mass transport into the nanopores, and (b) (sticking to the strong depletion model (8-3)) the concentration gradient of SDS close to the advancing liquid front, both are roughly independent of SDS concentration in this concentration range. The concentration gradient at the liquid-vapor interface in the strong depletion regime is approximately $c_b/(D_\infty t)^{1/2}$.[17] In the high concentration range considered here c_b in the gradient expression can be substituted by CMC – a good estimate for the concentration of free SDS molecules, thus satisfying point (b) above. In the strong depletion zone only free SDS should be present in solution, as the diffusion coefficient of free SDS molecules is about an order of magnitude higher than that of free SDS micelles (the diffusion coefficient of spherical micelles with radius 22 Å [23,24] obtained from the Stokes-Einstein relation is $D_{mic} \approx 1\cdot10^{-10}\ \mathrm{m}^2/\mathrm{s}$ at $25\ ^\circ\mathrm{C}$). Point (a) is more intriguing. By the way, requirement (a) is a sufficient condition for (b). Point (a) would require some mechanism that at this concentration regime kept the

concentration of micelles diffusing inside the pores the same, independent of c_b. This could occur due to a combination of electrostatic repulsion and confinement. In any case a proper elucidation of this point requires more accurate experiments and a better assessment of the real distribution of SDS aggregation states inside the nanopores.

8.3.3. Loading of SDS aqueous solution: equilibrium

We investigated the equilibrium loading and the final SDS adsorption as a function of the initial bulk concentration. In the long time limit, the fitting function, eq. (8-4), has the asymptotic value of a_0, which we took as the equilibrium loading for initial bulk concentrations in the CMC zone and above CMC.

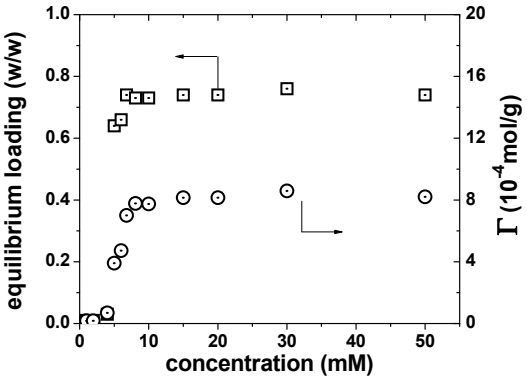

Figure 8.6 Equilibrium loading (squares) of SDS aqueous solution and the final SDS adsorption (circles) in nanoporous 1,2-PB films at different initial bulk concentrations.

For all the concentrations well below CMC, the equilibrium loading was taken from the last data point within our measurement time in Fig. 8.5b since nearly no loading was detected. The final SDS adsorption, Γ (given in mol of SDS per gram of nanoporous film, which is different from the units used for Γ_{max} in eq. (8-3)) in the nanoporous film after loading was determined by

$$\Gamma = \frac{(m_{dry} - m_{PB}) / M_{SDS}}{m_{PB}} \qquad (8\text{-}6)$$

where m_{dry} denotes the mass of the SDS loaded film after complete drying, and $M_{SDS} = 288$ g/mol is the molar mass of SDS. Strictly speaking, the weight gain ($m_{dry} - m_{PB}$) comprises both the adsorbed SDS on the pore walls and the SDS deposited from the aqueous solution filling the pores before drying. However, due to the large specific surface area in the nanoporous film, the weight contribution from the solution-deposited SDS is at the most 5% (for the case of highest SDS concentration used in this study, i.e. the 50 mM solution). It is not possible to see such a contribution in our data due to a data variability of similar magnitude, as can be seen in the plateau regions of Figs. 8.5b and 8.6. In other words, had the weight gain due to SDS deposition from the solution been significant, a plateau in the final SDS adsorption as that observed in Figure 8.6 would have been absent.

The dependences of the equilibrium loading and the final SDS adsorption on the initial SDS concentration c_b are shown in Fig 8.6. At $c_b \leq 4$ mM, the loading of SDS aqueous solution and the final SDS adsorption were both practically negligible as discussed earlier. After a sharp transition in the CMC zone, the equilibrium loading saturated at $c_b \geq 6.8$ mM, indicating that the interior volume of the nanoporous film was fully loaded with SDS aqueous solutions. Similar, but slightly more gradual saturation behavior was found for the final SDS surface adsorption. The maximum adsorption $\Gamma_{\max}$ was 8.1×10^{-4} mol/g, which agrees well with the maximum capacity determined by SDS adsorption isotherm to be discussed in the next section. The maximum solution equilibrium loading can be thought of as consisting of two parts: a liquid part and a SDS adsorbed on the surface part, therefore:

$$loading_{\max} = \rho v_{eff} + \Gamma_{\max} M_{SDS} \qquad (8\text{-}7)$$

where v_{eff} denotes the effective volume accessible to the loaded SDS aqueous solution per gram of nanoporous film. Inserting $loading_{\max}$ = 0.76± 0.03 and $\Gamma_{\max} = 8.1\times10^{-4} \pm 0.3\text{x}10^{-4}$ mol/g and assuming ρ = 1 g/cm^3, eq. (8-7) gives v_{eff} = 0.53 ± 0.03 cm^3/g. The volume occupied by the SDS layer per gram of the nanoporous film is then $v_{spec} - v_{eff} = 0.27 \pm 0.03$ cm^3/g. Given the specific surface area of the nanoporous film A_{spec} = 278 ± 40 m^2/g, we estimated a thickness of the adsorbed SDS layer of 1.0 ± 0.2 nm, as calculated by

$$l_{sds} = (v - v_{eff}) / A_{spec} \qquad (8\text{-}8)$$

For comparison, a value of $l_{sds} = 1.5 \pm 0.2$ nm was reported for the self-assembled monolayer of SDS at polystyrene/water interface at CMC[25], and a value of 1.53 ± 0.04 nm for the thickness of SDS hemimicelles.[26] The significant difference in monolayer thickness between our estimation and the literature values hints to a more compact monolayer of SDS in the dry state.

The Γ_{max} value itself allows an estimation of the average occupied area per adsorbed SDS. For a monolayer coverage (to be addressed), the occupied area per SDS molecule, A_0, at the maximum adsorption was 0.57 ± 0.08 nm^2, as calculated by

$$A_{spec} = \Gamma_{max} N_A A_0 \qquad (8\text{-}9)$$

where N_A is the Avogadro constant, and A_{spec} is the same as in eq. (7). Day et al.[27] reported values of 0.4 - 0.7 nm^2 in the low concentration regime of SDS adsorbed on hydrophobic graphitized carbon black. A value of 0.5 nm^2 per molecule was reported for adsorption of SDS on silicon substrates.[28]

Table 8.1 Summary of atom percentage of Sulfur and Carbon in the samples loaded at different SDS concentrations; comparison of surface adsorption Γ calculated from XPS and gravimetry.

	c_{SDS}	Atom%		Γ (10^{-3} mol/g)	
	(mM)	S	C	XPS(S)	Gravimetry
Sample0	0	0	97.9	0	0
Sample1	4.0	0.21	92.3	0.17	0.07
Sample2	8.1	0.81	91.8	0.73	0.76
Sample3	10	0.86	91.8	0.78	0.83

The quantitative analysis by XPS (Table 8.1) provided a direct evidence for the SDS adsorption inside the nanoporous film. As representatives of SDS-loaded samples at different concentrations, three samples obtained from solutions with SDS concentrations below, equal to and above CMC were investigated. Atomic percentage of Sulfur (S) and Carbon (C) derived from the integrated intensities of the corresponding S (2p) and C (1s) peaks are summarized in Table 8.1. A control sample of untreated nanoporous polymer is also included in the table as 'Sample0'. The data were transformed to mass ratios between adsorbed SDS and 1,2-PB film, and compared with the results from gravimetry (last column). Given the high uncertainty for the

XPS results, the signal intensity for S being below 1%, the comparison in the table is considered as satisfactory.

8.3.4. SDS adsorption isotherm

All the samples used for constructing the SDS adsorption isotherm were pre-wetted with methanol therefore they are expected to show the same access to the filling of SDS aqueous solutions, even for $c_b < 4$ mM and equal availability of adsorption sites for the SDS molecules.

The adsorption isotherm at a broad range of concentration is presented in Figure 8.7A.

In Figure 8.7B, the set of experimental data from Fig. 8.7A was fitted by the Langmuir model using the linear regression method, as expressed by:

$$\frac{c_{EQ}}{\Gamma} = \frac{c_{EQ}}{\Gamma_0} + \frac{1}{K_{eq}\Gamma_0} \qquad (8\text{-}10)$$

where K_{eq} (M^{-1}) is the Langmuir equilibrium constant, and c_{EQ} (mol/l) is the SDS concentration in solution at equilibrium. The successful description of the experimental data by the Langmuir model is consistent with a monolayer adsorption of SDS on the surface of the nanoporous polymer. The maximum surface capacity determined by the asymptotic value of the Langmuir fitting is $\Gamma_0 = 8.6\times10^{-4}$ mol/g, slightly larger than the maximum SDS adsorption Γ_{max} = $8.1\times10^{-4} \pm 0.3\cdot10^{-4}$ mol/g measured in our experiments.

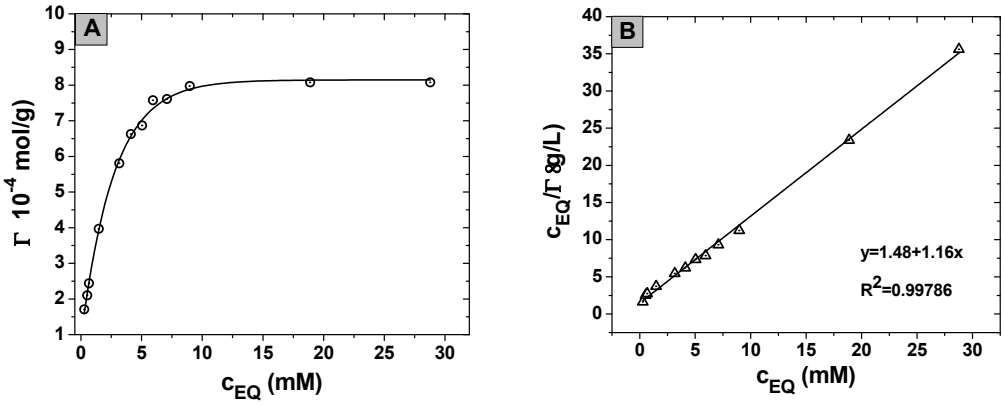

Figure 8.7 (A) Adsorption isotherm of SDS in nanoporous 1,2-PB film in water medium; (B) Linear regression of Langmuir adsorption fitting to the experimental data in Fig. 8.7A.

Assuming an activity coefficient of 1 for SDS in solution, the Langmuir equilibrium constant K_{eq} (7838 M^{-1}) gives a Gibbs free energy of adsorption of $\Delta G_{ads} = -RT \ln K_{eq}$ = -21.8 kJ/mol. For comparison, a value of -14.8 kJ/mol was reported for SDS adsorption on cellulose acetate membranes[29] and a value of -28 kJ/mol for SDS adsorption on a polystyrene surface.[30] Depending on the assumption used, values of Gibbs free energy of micellization ΔG_{mic} in the range -10 to -35 kJ/mol are reported.[31–34] This large spread of literature values prohibits a quantitative comparison of the thermodynamic preference of SDS unimers on one side to form micelles and on the other side to adsorb on the hydrophobic walls of nanoporous 1,2-PB. The amount of adsorbed SDS is significant; if it were all released in the pore volume the concentration would have been about 1M or 130 times CMC (which is beyond the solubility of SDS in water at $25\ ^{\circ}C$). From this consideration the adsorption of SDS onto the pore walls is expected to be favored relative to micelle formation inside the nanopores of the present material.

8.3.5. Stability of SDS physisorption in nanoporous 1,2-PB membranes

We demonstrated the water wettability of SDS-loaded nanoporous 1,2-PB films by measuring water uptake.

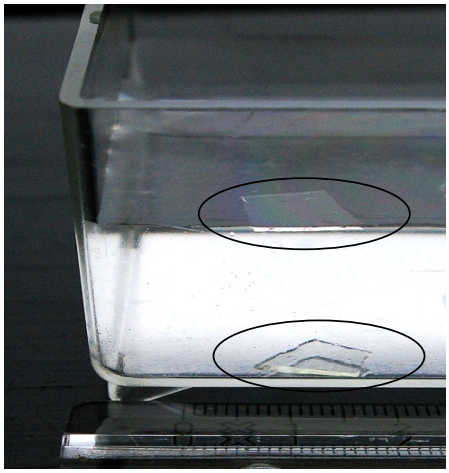

Figure 8.8 A photograph of a native nanoporous film (top) and a SDS-modified nanoporous film (bottom) in water. The ovals highlight the samples.

A native nanoporous film whose macroscopic density is approximately 0.6 g/cm^3, and a SDS-loaded nanoporous film after maximum loading were dipped in DI water. Figure 8.8 illustrates that the native sample floated on the surface of water, while the nanoporous 1,2-PB with incorporated SDS sank into the water. After 24 h, the water uptake of all the SDS-modified samples after a maximum loading was 0.54 ± 0.03 mg per milligram of tested sample, which is close to the previously mentioned (see discussion following eq. (8-6)) accessible mass ρv_{eff} = 0.53 ± 0.03 gram of SDS solution per gram of nanoporous sample. The quick water uptake clearly demonstrates that the hydrophobic nanoporous 1,2-PB films can be rendered hydrophilic by physisorption of SDS.

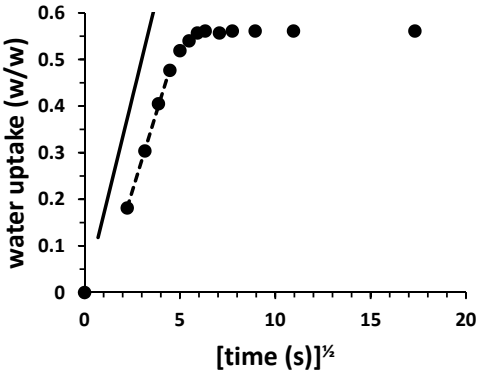

Figure 8.9 The solid circles are experimental data of water uptake as a function of square root of immersion time for a nanoporous 1,2-PB film loaded to saturation with SDS and then immersed into excess of deionized water. The solid line is a prediction from the Lucas-Washburn equation (see main text and note[35]). The dashed line is the linear trend line for the experimental data between 5 and 20 s.

The kinetics of water uptake into one SDS-modified nanoporous polymer is shown in Figure 8.9 by the filled circles. The mass of water relative to the mass of the polymer matrix is plotted as a function of square root of time. The saturation value is reached in about 30 s; a linear increase relative to $t^{1/2}$ is observed for the 4 data points between 5 and 20 s (segmented line), after a possible time lag at earlier times (data missing for times shorter than 5 s). The linearity relative to the square root of time qualitatively agrees with the kinetics of capillary rise predicted by the Lucas-Washburn equation (L-W).[1,2] A quantitative comparison of the uptake results with the prediction from the L-W equation is questionable due to possible changes of liquid and interface

composition in the process of imbibition and to the complex geometry of water access into the porous samples. However, we compare in Fig. 8.9 the trend slope of the initial experimental data with the prediction of the L-W equation (solid line) under the simplifying assumptions listed in note 35. The contact angle (61°) and the surface tension (34 mN/m) were taken equal to the plateau values in Figs. 8.4 (a, b); a tortuosity factor of 1.5 was included[35], which is characteristic for the gyroid porosity.[36] The slope predicted from the L-W equation under the mentioned assumptions[35] is 25% larger than the experimental observation. It's interesting that under reasonable assumptions the simple L-W model gives a rather good estimate of the intermediate slope for the kinetics of water uptake, despite the complexity of the system.

8.3.6. SDS release from nanoporous 1,2-PB membranes in water and methanol

Finally we present in Figure 8.10 results on the kinetics of SDS release in excess of water or methanol. SDS release is defined as the mass loss of the SDS-loaded sample over the initial amount of SDS adsorbed in the sample. The SDS release in water (full symbols) is significantly slower than the release in methanol. About 70% of the adsorbed SDS was released after 72 h in excess of water. The release of SDS in excess of methanol (empty symbols) was quantitative within 40 minutes. The release data in methanol (see the insert) are well fitted by a single exponential function of the form: $release\ (\%) = 100 \cdot [1 - \exp(-t/\tau_0)]$ with the characteristic time τ_0 = 10.4 min (segmented line in Fig. 8.10). The release data in water can be formally fitted by a double exponential function of the form of eq. (8-5) comprising two characteristic times τ_1 = 51 min. and τ_2 = 3900 min (solid line in Fig. 8.10). We conclude this paragraph by a discussion of the order of magnitude for the time-scales of SDS release in the two solvents.

We firstly observe that the solvent capillary uptake (see Fig. 8.9) is faster than the SDS desorption (Fig. 8.10), therefore we assume in the following that the solvent uptake does not delay significantly the SDS release process. Generally the release process comprises SDS desorption from the surface, formation of micelles, diffusion through the nanopores either as single molecules or as micelles, and re-adsorption onto the pore walls. A simple uninterrupted diffusion of a SDS molecule out of a 0.5 mm long nanochannel would take approximately 5 minutes in water and 3 minutes in methanol (the diffusion coefficient of single SDS molecules in

methanol was estimated from that of water by using the Stokes-Einstein relation and assuming the solvent viscosity as the only changing parameter). In the case of methanol we conjecture that the release of SDS can be described as a simple process of fast desorption and uninterrupted diffusion throughout the pores. The solubility of SDS in methanol is about 0.32 M at 20° C with no micelle formation[37]. Therefore not all of the adsorbed SDS can be dissolved at the first contact with methanol, as the capacity of adsorbed SDS exceeds the solubility by a factor of 3.1. The characteristic release time of SDS in methanol (10.4 min) is for that reason larger but of the same order of magnitude as the diffusion time of single SDS molecules out of the nanoporous sample (3 min).

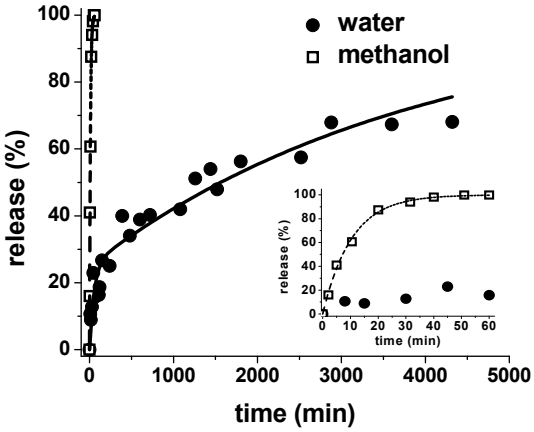

Figure 8.10 SDS release profiles in excess deionized water (solid circles) and excess methanol (open squares) from nanoporous 1,2-PB films preloaded with SDS. The solid line is a double exponential function fitting to the experimental data of release in water (see text and eq. (8-4)); the dash line denotes a single exponential fitting to the experimental data of release in methanol (see text). The insert shows the SDS release profiles within the first 60 min.

In water, half of the SDS was released in approximately 25 h, which is a factor of 300 slower than the characteristic uninterrupted diffusion time of single SDS molecules out of the nanopores (5 min). The desorption/re-adsorption process limits the SDS concentration in the solution filling the nanopores, which may cause the actual concentration gradient across the film orders of magnitude smaller, slowing down the release process. Assuming that the transport of SDS out of the nanopores is mainly happening by diffusion of single molecules, the time-scale of the release process could be understood as follows. The initial concentration of single SDS molecules in the

nanochannels (at time = 0 in Fig. 8.10) is of the order of 10 mM as estimated by the amount of adsorbed SDS and the Langmuir equilibrium constant. The amount of SDS with this concentration in the porous volume is 1% of the total adsorbed SDS, which brings the characteristic release time from minutes (single SDS molecule) to hours. We are missing at present a quantitative description of the SDS release profile in water. Such a description may be obtained by solving the diffusion problem in the presence of Langmuir's type desorption/adsorption kinetics, which is outside the scope of this contribution.

8.3.7. Anti-biofilm demonstrations

We attempted to explore the potential of nanoporous film as a sustainable release carrier. As a demonstration example, we evaluated the ability of SDS-infilled nanoporous 1,2-PB films to suppress or minimize the formation of biofilm by two different bacteria, gram negative *E.coli* and gram positive *S. epidermidis*. Figure 8.11 compares the results for the original nanoporous film and the SDS-loaded nanoporous film after they were in contact with *E. coli* culture for 24 h. Three columns in Figure 8.11 shows the view of the same location on the film surface by 3-dimensional image projection in left column, *xy* dimensions in middle column and 3-D image in right column. Obviously, the SDS-loaded nanoporous film efficiently restricted the *E.coli* biofilm formation on the nanoporous film surface. Relatively insignificant amount of dead (appears red) *E. coli* cells stay on the surface. In contrast, the dense and thick biofilm of living cells (appears green) was formed on the original film without SDS infiltration.

After 48 h, *E. coli* bacterial cells continuously grew and cell population became significantly large in culture leading to a denser and thicker biofilm on the surface of the control sample (Figure 8.12). In comparison, the SDS-loaded film still retained an anti-biofilm surface. Similar to the first day, the dead cells did not significantly adhere to the surface. In the case of *E.coli*, the SDS-loaded film could suppress the formation of biofilm to some extent. Because the released SDS served as biocides to stop the growth of *E.coli*, and in the meantime served as detergents to prevent or reduce the cohesion of *E.coli* cells and adhesion to the surface. In addition, the sustained release made the surface continuously effective against the formation of biofilm for at least 48 h.

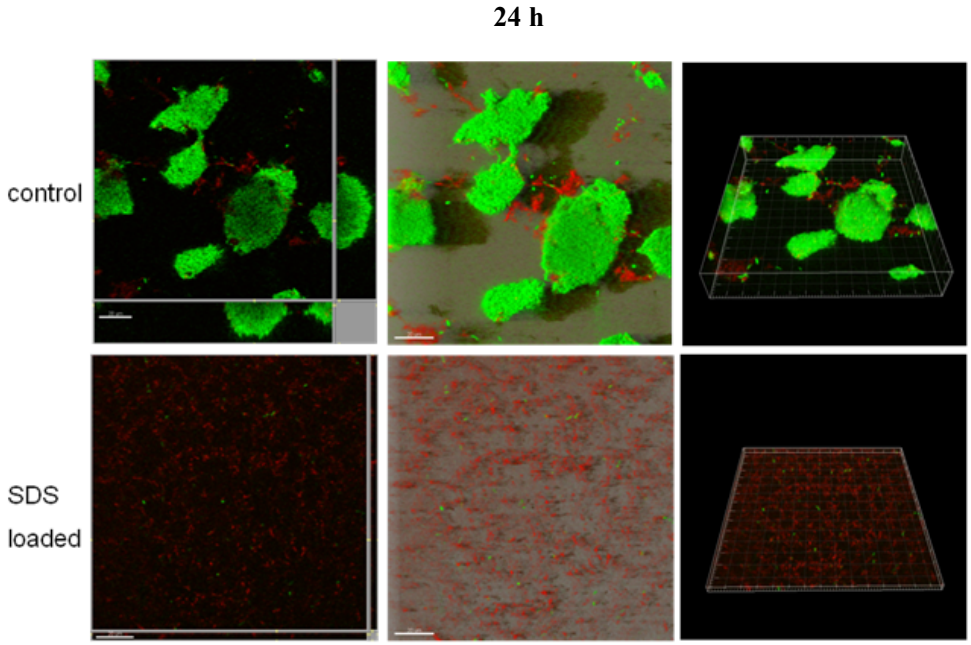

Figure 8.11 Comparison of the surface of original nanoporous 1,2-PB film (up row); and the surface of SDS-loaded nanoporous 1,2-PB film (down row) after contact with *E. coli* medium for 24 h. Three-dimensional image projection (left column); *xy* dimensions (middle column) and 3-D image (right column). Live bacterial cells appear green and dead cells appear red.

We further challenged the SDS-loaded nanoporous film with *S. epidermidis*. Figure 8.13 shows a dense living biofilm formed on the surface of the original nanoporous film (left) and a dense but inactive (dead) film attached on the SDS-loaded film (right). This means SDS could be able to destroy the cells and inhibit their growth but could not detach the *S. epidermidis* biofilm. We found that the biofilm formed by *S. epidermidis* was far denser than that formed by *E. coli* (Figs 8.11 and 8.12).

These observations underscore the fact that detachment and inhibition of biofilm are distinct phenomena. Chemical agents that exhibit bactericidal activity will not necessarily cause removal of the inactive biofilm; while those that promote removal may or may not destroy microorganisms. The formation of biofilm on a surface is mainly due to multiple inter-active forces which contribute to biofilm cohesion and its adhesion to surface, e.g. electrostatic interactions, hydrogen bonding, hydrophobic interaction. All these forces mainly depend on the nature of the bacteria or the solid surface used, as well as the existing medium conditions.

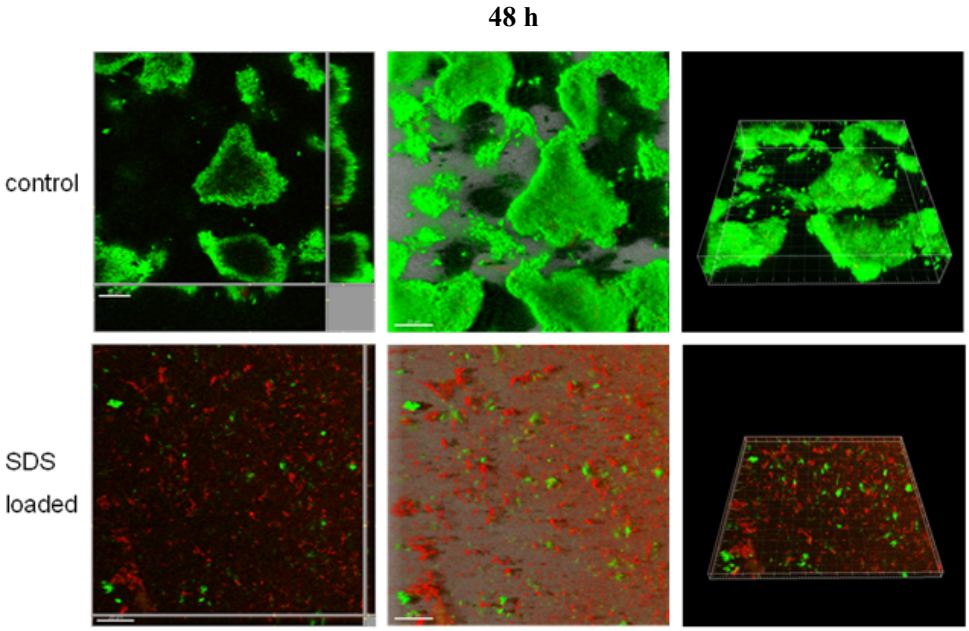

Figure 8.12 The surface of original nanoporous 1,2-PB film (up row); and the surface of SDS-loaded nanoporous 1,2-PB film (down row) after 48 h contact with *E. coli* cuture.

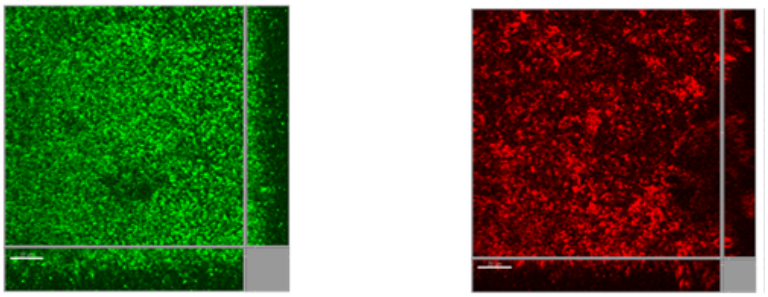

control **SDS-loaded**

Figure 8.13 3-D image projection for the surface of nanoporous 1,2-PB film with (right) and without (left) SDS infiltration, after 24 h contact with *S. epidermidis* culture.

As shown above, in both cases the SDS-loaded film surface has a capability of inhibiting the growth of the bacterial cells. Here we have a short discussion on the release-derived inhibiting concentration at the local interface. Minimum inhibitory concentration (MIC), in microbiology,

is the lowest concentration of an antimicrobial that will inhibit the visible growth of a microorganism after incubation. MIC_{50} is the SDS concentration known to cause 50% decrease in the growth rate of suspended e.g. *E. coli* (MIC_{50} = 125 μg/ml as tested by Y. Lang). This means the release of SDS from nanoporous film should achieve a concentration (≥ MIC_{50}) at the interface sufficient to destroy bacteria attempting to adhere to the film surface. Using the SDS release profile in Fig. 8.10, we can estimate the interface concentration of SDS by mass transfer calculations and compare with MIC_{50}. In water, half of the SDS was released in approximately 25 h, therefore the average release flux J_{SDS} (= 0.1 mg/cm^2/h) can be calculated by the average release rate over the surface area of the film,

$$J_{SDS} = \frac{50\% \cdot \Gamma_{\max} \cdot m_{PB}}{A \cdot t} \qquad (8\text{-}11)$$

where $\Gamma_{\max} = 8.1 \cdot 10^{-4}$ mol/g, $m_{PB} = 20$ mg, $t = 25$ h, $A = 0.9$ cm^2

To justify that the J_{SDS} as calculated above was sufficient to kill bacteria in the near-surface zone, a boundary layer model was considered. The boundary layer thickness is a region over which the concentration drops from the maximum at the surface zone to zero at some distance way. Using Fick's law of diffusion where $J = -D_{SDS}(dC/dx) \approx -D_{SDS}(C_s - C_0)/\delta_m$ and substituting the values for $D_{SDS} = 7.8 \cdot 10^{-10}$ m^2/s, $J = J_{SDS}$, $C_s = MIC_{50}$ and $C_0 = 0$, the boundary layer δ_m was calculated to be 92 μm. This indicates within 5 μm away from the surface, the SDS concentration is still very close to MIC_{50}; while the size of a bacterium is usually 1~ 2 μm. In fact, the concentration needed to inhibit bacterial adhesion at dissolved concentrations is usually less than MIC_{50}. Thus the SDS release rates even lower than 0.1 mg/cm^2/h would be still effective in limiting bacterial adhesion in the case of *E. coli*.

8.4. Conclusions

Loading kinetics and equilibrium of SDS aqueous solutions into hydrophobic nanoporous 1,2-PB film of gyroid morphology was investigated. The values of SDS concentration studied covered two decades, from 16 times below to 6 times above CMC (8.1 mM). A typical loading experiment consisted of gravimetric measurements of a nanoporous sample at chosen time

intervals during a total time of up to 9500 min. No loading was observed for SDS concentrations up to 4 mM, while the final loading of the pore volume was almost complete for concentrations above 5 mM. Significant variations in kinetics were observed in the SDS concentration range 5 mM up to CMC. The initial loading data, for times of up to 360 min follow straight lines if plotted relative to the square root of loading time. This behavior can be described by a simple model in which diffusion of single SDS molecules towards the advancing and continuously depleted liquid front is the rate determining process. The depletion of the liquid-vapor interface from SDS molecules is due to adsorption of SDS onto the pore walls. The adsorption isotherm is consistent with the Langmuir adsorption model and therefore with the formation of a SDS monolayer on the pore walls. The thickness of the monolayer was estimated to be 1.0 nm and the occupied area per SDS molecule was 0.57 nm^2. The originally water repelling nanoporous polymer was transformed into hydrophilic after the physisorption of SDS; water spontaneously filled the pore volume of dry modified samples. The kinetics of water uptake into the nanoporous polymer modified with the surfactant was measured and compared to a prediction of the Lucas-Washburn model. At last, data on the kinetics of SDS release in the presence of excess water or methanol were also presented. The SDS release in methanol was quantitative within 40 min; it showed a characteristic time-scale similar to the characteristic time estimated for single SDS molecules to diffuse out of the pores by simple diffusion in methanol, solubility taken into account. In water the release of SDS was significantly slower, with 1/3 of the original SDS still unreleased after 72 h. A quantitative description of SDS release kinetics in water is missing. Physisorption of SDS is a simple and fast way of modifying the hydrophobic nanoporous polymer membranes. The presented work is the first systematic study of SDS adsorption into a hydrophobic nanoporous polymer with well-defined morphology.

SDS-loaded nanoporous films were tested in the biofilm assay. For *E.coli*, the SDS-loaded film had a good effect on limiting the formation of biofilm on the surface under a sustained release; however it could not completely exclude the inactive cells from the surface. For the *S. epidermidis*, the surface of SDS loaded film was able to inhibit the growth of cells but could not remove the inactive biofilm. We also justified the restriction of delivery of SDS at sufficient flux to the surface within a certain diffusion boundary layer. These tests preliminarily demonstrate the potential of the nanoporous films as a sustained-release carrier. They can be possibly in future used to release antibiotics minimizing systemic side effects, maximizing surface antibacterial

properties and prolonging the time over which a device contains sufficient antibiotics to be effective. A quality in controlled release is also expected to develop for nanoporous 1,2-PB polymers by rendering a stimuli sensitivity.

8.5. References and notes

[1] Lucas, R. *Kolloid Z.* **1918**, *23*, 15-22.

[2] Washburn, E. W. *Phys. Rev.* **1921**, *17*, 273-283.

[3] Tadros, T. F. *Applied Surfactants: principles and applications*, Wiley-VCH, **2005**.

[4] Hall-Stoodley, L.; Costerton, J. W. and Stoodley , P. Bacterial Biofilms: from the Natural Environment to Infectious Diseases. *Nature Reviews | Microbiology* **2004** , *2*, 95-108.

[5] Chen, X. and Stewart, P.S. Biofilm Removal Caused by Chemical Treatments. *Wat. Res.* **2000**, *34*, 4229–4233.

[6] Haagensen, J. A. J.; Klausen, M.; Ernst, R. K.; Miller, S. I. ; Folkesson, A.; Tolker-Nielsen, T.and Molin, S. Differentiation and Distribution of Colistin- and Sodium Dodecyl Sulfate-Tolerant Cells in *Pseudomonas aeruginosa* Biofilms. *J. Bacteriology* **2007**, *189*, 28–37.

[7] Pashley, R. M.; Karaman, M. E. *Applied Colloid and Surface Chemistry*, John Wiley & Sons, Ltd. **2004**; Chapter 2.

[8] Jakobsen, M. R.; Grydgaard, *A Characterization of Nano Cavities in Polymeric Materials*, *B.Sc. Thesis*, Technical University of Denmark, **2006**.

[9] Guo, X. F.; Andreasen, W.J.; Vigild, E.M.; Ndoni, S. *Macromolecules* **2007**, *40*, 3669-3675.

[10] Turner, S.F.; Clarke,S.M.; Rennie, A.R.; Thirtle, P.N.; Cooke, D.J.; Li, Z.X.; Thomas, R.K. *Langmuir* **1999**, *15*, 1017.

[11] Mark, J. E. *Polymer Data Handbook*, Oxford University Press, **1999**.

[12] Paria, S.; Khilar, K. C. *Advances in Colloid and Interface Science* **2004**, *110*, 75–95.

[13] Chen, J. H.; Ruckenstein, E. *J. Colloid and Interface Sci.* **1991**, *142*, 544–553.

[14] Casford, M. T. L.; Davies, P. B.; Neivandt, D. J. *Langmuir* **2006**, *22*, 3105–3111.

[15] Ndoni, S.; Vigild, M.E.; Berg, R.H. *J. Am. Chem. Soc.* **2003**, *125*, 13366-13367.

[16] The etching process generates one end-group $-\overset{|}{\underset{|}{Si}}-F$ per chain of 1,2-PB in the nanoporous 1,2-PB film,[16] which is expected to expose on the surface after removal of PDMS. The number average molecular weight of block copolymer 1,2-PB-b-PDMS is $\overline{M_n}$ = 14100 g/mol, and the mass fraction of

PDMS is w_{PDMS} = 0.41 (see the chapter 3.2). For 1 gram nanoporous 1,2-PB the number of -Si-F is: $N_{Av}/M_{n,PB} = 6.02 \cdot 10^{23}$ mol^{-1}/ 8300 g·mol^{-1} = $7.3 \cdot 10^{19}$ g^{-1}, which corresponds to 0.26 -Si-F per nm^2 of surface area (A_{spec} =278±40 m^2/g). The number of 1,2-PB repeating units per nm^2 surface area is [10^{-21} (g·nm^{-3}) · $6.02 \cdot 10^{23}$ (mol^{-1}) / 54 (g·mol^{-1})]$^{2/3}$ = 5 nm^{-2}. Therefore, the surface density of -Si-F is 5.2% relative to the surface repeating units of 1,2-PB.

[17] Zhmud, V.B.; Tiberg, F.; Hallstensson, K. *Journal of Colloid and Interface Science* **2000**, *228*, 263–269.

[18] Tiberg, F.; Zhmud, B. *Phys. Chem. Chem. Phys.* **2000**, *2*, 5189–5196.

[19] Kilau, H.W.; Pahlman, J. E. *Colloids Surf.* **1987**, *26*, 217-242.

[20] Churaev, N. V.; Zorin, Z. M. *Colloid Surf. A* **1995**, *100*, 131-138.

[21] Brielles, N.; Chantraine, F.; Viana, M.; Chulia, D.; Branlard, P.; Rubinstenn, G.; Lequeux, F.; Mondain-Monval, O. J. Colloid Interface Sci. 2008, 328, 344-352.

[22] Deng, Z.; Lu, H.; Leaist, D. G. *J. Chem. Eng. Data* **1996**, *41*, 214-217.

[23] Almgren, M.; Swarup, S. *J. Phys. Chem.* **1982**, *86*, 4212-4216.

[24] Bales, B. L.; Messina, L.; Vidal, A.; Peric, M.; Nascimento, O. R. *J. Phys. Chem. B* **1998**, *102*, 10347-10358.

[25] Turner, S.F.; Clarke, S. M.; Rennie, A. R.; Thirtle, P. N.; Cooke, D. J.; Li, Z. X.; Thomas, R. K. *Langmuir* **1999**, *15*, 1017-1023.

[26] Burgess, I.; Zamlynny, V.; Szymanski, G.; Lipkowski, J. *Langmuir* **2001**, *17*, 3355–3367

[27] Day, R.E.; Greenwood, F.G.; Parfitt, G.D. *Proc. 4th Int. Congr. Surf. Activity* **1967**, *2*, 1005.

[28] Luokkala, B.B.; Garoff, S.; Suter, R.M. Phys. Rev. E 2000, 62, 2405.

[29] Singh, K.; Tiwari, A.K. *Colloid Journal* **2008**, *70*, 101-104.

[30] Kronberg, B.; Costas, M.; Silveston, R. *Pure & Appl. Chem.* **1995**, *67*, 897-902.

[31] Liu, T. Q. *Journal of Dispersion Science and Technology* **2008**, *29*, 335–339.

[32] Zana, R. *Langmuir* **1996**, *12*, 1208–1211.

[33] Valente, A. J. M.; Burrows, H. D. *J. Colloid Interface Sci.* **2008**, *323*, 141–145.

[34] Szymczyk, K.; Janczuk, B. *Langmuir* **2009**, *25*, 4377–4383.

[35] The Lucas-Washburn equation[1,2] predicts a capillary uptake length $l(t) = [(r\,\gamma\cos\theta)\,t\,/\,(2\eta)]^{1/2}$, where r is the capillary radius, γ the liquid surface energy, θ the contact angle, t the time and η the viscosity of the liquid. By simplifying the capillaries to a bundle of cylinders of radius r, like we did relative to eq. (8-3) in the text, we can convert $l(t)$ into mass of water uptake relative to the mass of the nanoporous

polymer matrix, $w(t)$, which is the vertical axes in Fig.8.8: $w(t) = m_{H2O}(t) / m_{NP} = [A \cdot \varepsilon_A \cdot l(t) \cdot \rho_{H2O}] /[A \cdot h \cdot \tau \cdot \rho_{NP}]$ where A is the projected flat area of the sample, ε_A the surface porosity, h the height of the sample, ρ_{H2O} (ρ_{NP}) the density of water (dry nanoporous sample) and τ the tortuosity factor. The values of the parameters for the solid line in Fig. 8.8 are: $\varepsilon_A = 0.45$; $\rho_{H2O} = 10^3$ kg/m^3; $\rho_{NP} = 0.6 \cdot 10^3$ kg/m^3; $h = 5 \cdot 10^{-4}$ m; $\tau = 1.5$; $r = 6 \cdot 10^{-9}$ m; $\theta = 61°$ (see Fig. 8.3 (B)); $\mu = 10^{-3}$ Pa·s; $\gamma = 0.034$ N/m. The tortuosity factor of 1.5 is characteristic for the gyroid morphology.[33] The pore radius was assumed to be 1.5 nm smaller than that of the unmodified nanoporous polymer, due to the presence of 'wet' adsorbed SDS onto the pore walls. The values of the surface tension γ and the contact angle θ for the liquid were taken equal to the respective plateau values in Figs. 8.3 (A,B).

[36] Hamersky, M. W.; Hillmyer, M. A.; Tirrell, M.; Bates, F. S.; Lodge, T. P. *Macromolecules* **1998,** *31,* 5363-5370.

[37] Miyata, I.; Takada, A.; Yonese, M.; Kishimoto, H. *Bull. Chem. Soc. Jpn.* **1990**, *63*, 3502-3507.

Chapter 9 Summary and Suggestions for Future Work

The overall objective of this Ph.D. project is the development of block copolymer templated nanoporous polymers for use in membrane applications. Gyroid morphology of the membrane is designed from synthesis stage to show isotropic percolation with no need for structure pre-alignment. Narrow pore size distribution is intrinsically determined by microphase separation of block copolymers at molecular scale. Surface structure of the membrane has been successfully controlled by using different substrates in the process of membrane fabrication. The original hydrophobic pore surface has been tailored by UV photo-oxidation or UV-induced thiolene chemisty thus avoiding the use of pre-wetting solutions on one side and enabling the fouling minimization on other side. Studying the membrane property of the nanoporous polymers was thus facilitated by precise control over the (bulk and surface) morphology and pore size, and easy functionalization of the surface chemistry.

Three relevant membrane applications have been targeted in the project. The first effort aimed to develop semi-permeable dialysis membranes as diffusion-restricting outer membranes in amperometric glucose sensors. Chapter 6 consists of two parts. The first part reviewed the fundamental work on understanding the diffusive transport in nanoporous 1,2-PB membranes in dialysis in terms of permeability and selectivity. The solute permeation could be altered over a significant range by changing surface morphology, thickness, and active porosity. From non-skin membrane to double-skin membrane, the effective diffusion coefficient could be extended over 2 orders of magnitude from 10^{-6} cm^2/s to 10^{-8} cm^2/s. The selectivity of the nanoporous membranes was investigated relative to a series of antibiotics, proteins and other biomolecules. The solute transport could be described in terms of size exclusion and hydrodynamic interactions. The permselectivity can be achieved by size sieving for which size effect is the dominant factor or by adsorption which captures the passing solutes to give a separation.

The second part of chapter 6 reported the results from sensor tests which assembled the nanoporous 1,2-PB membrane in multi-layer membrane system for glucose electrode, in comparison with the standard commercial electrodes. Unfortunately, the reduction in pore size (10 nm) relative to the reference membrane PET (100 nm) did not cause an effective restriction

in glucose permeability (i.e. effective diffusion coefficient) while the 3 orders of magnitude increase in porosity led to undesired ultrahigh glucose permeation. Therefore the original nanoporous membrane does not satisfy this specific application. Actually, we have realized this confliction from the prediction by theory and experimental data during the fundamental study in the first part. The high glucose permeability was reflected by a series of glucose diffusion tests, which could be also predicted by the dependence of D_{eff} on r_p. Even for the double-skin membranes, glucose permeation is still higher than that required in sensors. Adjusting active porosity was thought to be a simple and effective approach to meet the demand. Unfortunately, as shown in the results from sensor tests, the hydrophobic membrane became fully permeable to sample solution after 20 h pre-conditioning so that no flux difference existed between hydrophobic and UV photo-oxidized membranes. Considering the need of a fast response for sensor performance, we would not suggest increasing the membrane thickness to reduce the glucose permeation. Using an additional coating layer on the membrane surface to diminish surface porosity or on pore wall to reduce both porosity and pore size might be one of possibility for the future work.

High porosity thus high flux and narrow pore size distribution thus high selectivity are the advantages of the nanoporous membranes derived from self-assembled block copolymers. Therefore we should pursue applications that fully take advantage of the merits of this membrane system rather than restricting or losing their advantageous quality. The hydrophilized non-skin membranes might be promising for hemodialysis applications where high flux and selectivity, and anti-fouling are desired.

Beyond diffusive transport property, characterizing the convective transport property is also of critical importance to understand membrane performance of well-defined nanoporous polymers.

Chapters 7 focused to evaluate the ability of the nanoporous 1,2-PB membranes to reject dissolved solutes. These rejection experiments are more practically interesting and allow the potential of the membranes to be evaluated. Membrane fouling was first investigated as a main problematic issue of affecting the rejection performance. Solutes PEG were used to measure the membrane-solute interaction and solute-solute interaction under static and dynamic conditions. A big water flux decline confirms a strong static adsorption of PEG from water solution onto the original hydrophobic membrane (including within the membrane structure). Changing the solvent property or tailoring the pore surface chemistry can significantly suppress the fouling in

ultrafiltration and allow understanding intrinsic characteristics of the membranes. Single solutes PEG and mixed solutes PEG were used to determine the molecular weight cut-off (MWCO) curves. Tunable rejection properties via distinct separation mechanisms have been realized by changing the solvent property and surface property. The experimental data collected for the single PEG solutes was compared with the theory for hindered diffusion without adjustable parameters. Totally different rejection profiles were observed for the three systems studied, M+W, M+EW, and HM+W. In M+EW, the presence of ethanol made it possible to behave as expected by theory. In M+W system, due to significant PEG adsorption onto huge interior hydrophobic surface, the rejection curve of the nanoporous membrane was unexpectedly extended from 100% to - 40% . This finding inspired the use of the nanoporous membrane as an selective absorber to abundantly remove small solutes by internal surface adsorption and on the other side effectively reject the large solutes by size exclusion. The surface hydrophilization via binding sulfonated groups on one side diminished the adsorptive fouling on the other side resulted in a reduction in effective pore size thus enabling a completely new rejection property. A molecular weight cut-off shifted to the low molecular weights, e.g. between 1 Kg/mol and 4 Kg/mol. The mixed PEG experiments showed similar results. Protein ultrafiltration would be next step to challenge the ability of nanoporous 1,2-PB membranes in a way close to real applications.

Demonstrating the ability to reject dissolved solutes is important for establishing the practical value of these membranes. Equally important to an ultrafiltration membrane is the ability to produce a high solute flux. At the present stage, 20 ~ 30 μm thick membranes were prepared for convenience of scientific research. From practical interests, such thickness range has undesired low hydraulic permeability. Compared to the literature flux values reported for typical commercial membranes, the membranes fabricated in this work are about 100 times lower. This is because the commercial phase inversion membranes commonly have a thin selective layer at nanometer scale. The resistance to flow is inversely proportional to the thickness. If we reduce the thickness of the nanoporous 1,2-PB membrane to hundreds nanometer scale and integrate it onto a mechanical support macroporous membrane, a hundreds time increase in flux would be expected. This increase would make the flux across the bicontinuous structure competitive with phase inversion membranes.

The last focus in the Ph.D. project has been discussed in chapter 8, which was based on our interests to develop the nanoporous membrane as a sustainable-release carrier. SDS has been used as a model molecule to investigate loading of the aqueous solution and the accompanying physisorption of SDS into the hydrophobic nanoporous films. The loading showed varying dependence on the SDS concentration. No loading was observed for SDS concentrations below 4.0 mM. At concentrations above 5.0 mM, the initial part of loading showed a linear dependence on the square root of time, which can be interpreted as diffusion-controlled dynamics. Both the specific equilibrium loading and the final SDS adsorption reached plateau values at concentrations above 6.8 mM. The SDS adsorption isotherm can be well described by the Langmuir model, consistent with a monolayer adsorption onto the pore walls. The SDS-infilled nanoporous films clearly showed water wettability, in contrast to the original hydrophobic nanoporous 1,2-PB. The release process of SDS from the nanopores in the presence of excess of water or methanol showed the very different time scales. The demonstration of anti-biofilm surface showed a promising result. In the future, different drug release could be studied. More interestingly, it is to make the nanoporous 1,2-PB polymer as a stimuli sensitive matrix thus showing a quality of control release response to specific environment.

The present nanoporous 1,2-PB membranes have a shortcoming which must be addressed, that is, poor mechanical strength. First, the cross-linked films very often split up during the etching process so that it is difficult to fabricate a large scale of flexible membrane which is more commercially interesting. Besides, the resulting nanoporous membrane is very fragile, which brings so much trouble in handling it in different operations. The mechanical strength of the nanoporous 1,2-PB matrix was so weak that could not withstand high pressure. Therefore more mechanically robust polymers which do not crack during membrane production and operation are needed.

One of possibility is to increase the molecular weight of the block copolymer. However, high molecular weight block copolymer samples do not quickly form a well ordered porous structure because the rearrangement of the polymer chains is slow. To avoid this, lower molecular weight samples are very often used during the fabrication of the block copolymers. This results in a low degree of entanglement which compromises the mechanical integrity of the membranes. PB block is gel-like at room temperature because its zero-below glass transition. Very often a high degree of cross-linking is necessarily required to achieve a mechanical stability against solvent;

however this step also leads to an internal stress remaining in the matrix. Finally, we may find a compromising point by appropriately increasing the molecular weight of precursors and moderately reducing the cross-linking degree. In addition, using mild UV cross-linking to replace thermal cross-linking may give a help to reduce internal stress. In addition, as suggested by Sokol Ndoni from our group, saturation of double bonds by catalytic hydrogenation thus creating somewhat crystallinity in matrix will be tried to increase the film toughness in near future. The detailed description is out of scope of this thesis and the principle can be found in Ref 1.

References

[1] Mahanthappa, M. K.; Lim, L. S.; Hillmyer, M. A. and Bates, F. S. Control of mechanical behavior in polyolefin composites: Integration of glassy, rubbery, and semicrystalline components. *Macromolecules* **2007,** *40,* 1585–1593.

Appendices

Appendix A Fabrication Methods

Mechanically robust polymers which do not crack during membrane production and operation are needed for our research work in practice. No doubt, it is of critical importance for any membrane applications in reality. We often fabricated nanoporous 1,2-PB films with a thickness of 500 μm – 1000 μm in previous work for investigating structure characteristics, surface modifications, etc. However, this Ph.D. project covers more application-oriented research, thus nanoporous 1,2-PB membranes with a thickness in a few micrometers would be preferred. Due to high brittleness of the nanoporous 1,2-PB membranes, it took a full year to find an appropriate method to fabricate thin membranes that can be handled. Here we summarize all the failure approaches that have been tried in the thesis work. It might be useful information for future work.

Solvent casting

We started to prepare 100 μm thick films with the conventional method, i.e. solvent casting the polymer solution (in THF) onto a glass petri-dish. After solvent evaporation, an empty zone was always formed in the center of solvent cast film, and polymer enriched at the edge of the film, thus having an uneven distribution in thickness along the radial direction. Different thicknesses were tried. This phenomenon became more serious in smaller thicknesses. It can be attributed to 'coffee-ring' effect as described in detail in Ref 1. The dissolved polymers transferred to the edge of the petri-dish as pulled by the evaporating flow of solvent. We tried to adjust the solvent casting formulation in order to minimize the 'coffee-ring' effect. For instance, we increased viscosity of casting solution by making a high ratio of polymer/solvent. We also selected solvents with low vapor pressure and low volatility, such as toluene, and cyclohexanone. Instead of glass petri-dish, teflon petri-dish, polyester or PDMS substrate were also used as a substrate for solvent casting. However, it did not give a significant help.

Regarding the cross-linked films, it is difficult to detach from the petri-dish as the thickness is less than 50 μm. In addition, as the film thickness reduced to tens of micrometer, the cross-linked films immediately split up or curled up in contact with the etching solution.

Mechanical cutting

Since it is difficult to make thin films by solvent casting, laser ablation and micro-milling and polishing were tried to make thin films from thick cross-linked polymer bulk. However, the samples got burn as irradiating with a laser beam even with cooling water. Micro-milling and polishing resulted in very rough surface with cracks.

Dispersing

We used a micropipette to dispense a droplet of polymer solution on glass plate. It was hardly to control the final thickness with an even thickness. An intact cross-linked film with a large area could not be removed from the glass plate without breaking. Therefore we tried to use water as a substrate, and dispense the polymer solution in toluene onto water surface as shown in Figure AA1. Because toluene and water are immiscible and the density of toluene is less than 1 g/cm^3, a piece of free polymer film could float on the water surface after evaporation of toluene. Thereafter the free film can be transfer to another solid substrate for cross-linking. Using this method, it is hardly to make a film with large area. In addition, due to the droplet contraction during the evaporation, most of the films had a larger thickness in central part.

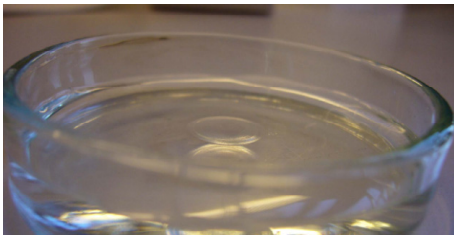

Figure AA1 A 1,2-PB-PDMS film floating on water surface in a petri-dish.

Spin coating

Spin coating is a very common approach for depositing a thin layer of material on a substrate. Again, it is difficult to remove such thin film from the substrate and the thin film could not be able to survive in the etching solution either. Therefore we considered to make a composite membrane instead of a free film. Different types of filter paper (Whatman or Millipore) were used as a support. One of examples is given in Figure AA2. We adjusted various parameters, e.g. solution viscosity, rotating speed, and substrate to optimize the coating layer; however it is not

easy to make a uniform flat surface. In addition, the block polymer used in the thesis work is not commercially available; it is prepared by a technician. Spin coating is not a cost-effective approach to make films in the present study, since it consumes a large amount of polymers during the process. So we shifted to the approach, applicator casting.

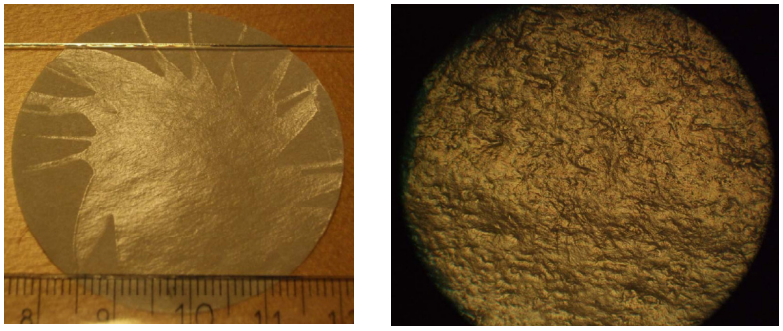

Figure AA2 a photograph of a Nylon filter paper spin coated with cross-linked 1, 2-PB-*b*-PDMS (left); surface of the spin coating layer (cross-linked 1, 2-PB-*b*-PDMS) at a magnification of 40 X (right).

Applicator casting

The polymer solution with high viscosity was prepared and casted onto a filter-paper substrate with different applicators as illustrated in Figure AA3. Finally, we developed a method called glass tube drawing by which the block copolymer layer with various thicknesses and area could be casted on the substrate as displayed in Figure AA4.

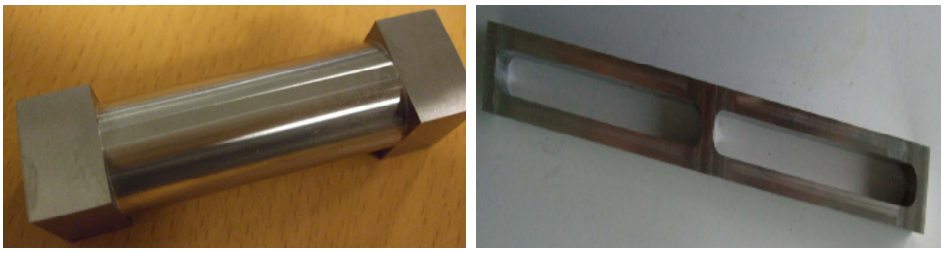

Figure AA3 Two applicators used in film preparation for different thickness: 50 µm (left) and 10 µm (right).

For both approaches, spin coating and applicator casting, we found somewhat penetration of block copolymer into the filter paper substrate. It was difficult to obtain smooth surface and

visible pinholes formed after cross-linking. We tried to pre-fill the porous substrate with PDMS, cross-link the PDMS, and then cast polymer solution with the glass tube. Significant difference between the filter paper and PDMS resulted in the film with very heterogeneous structure.

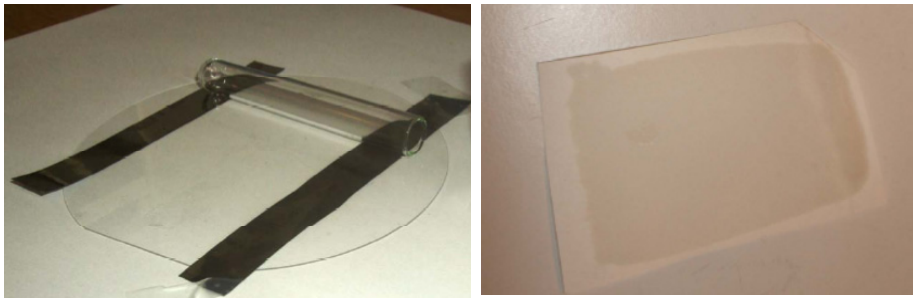

Figure AA4 Glass tube drawing with aluminum foil as spacers (left); a sample prepared by glass tube drawing method showing the cross-linked 1,2-PB-*b*-PDMS layer casted on a filter paper.

At the present stage, the main objective is to characterize the intrinsic property of nanoporous 1,2-PB, e.g. hydraulic permeability, gas permeation, etc. In order to accurately reveal the 1,2-PB membrane as it is and interpret the membrane behavior in relation to its structure, we finally decided to make free membranes without any support. At that moment, we still kept using glass tube drawing method. We cast the polymer solution onto teflon-coated glass plate. Therefore it was much easier to peel the cross-linked film off from the plate. But it was still a big challenge to protect the film intact during the etching step. As mentioned above, the thin film was always broken as in contact with the etching solution. Therefore we packed the cross-linked with filter paper and immersed the entire package into the etching solution as shown in Figure AA5. Finally we could be able to make some free films.

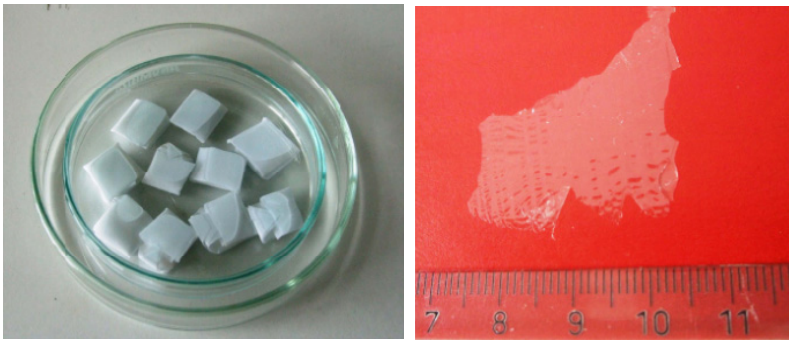

Figure AA5 cross-linked films were packed in filter paper before immersing in the etching solution (left); a free nanoporous 1,2-PB film prepared with glass tube drawing method (right).

A series of diffusion tests were performed with the samples prepared by glass tube drawing. Unfortunately, it was difficult to get reproducible data. The sample surface was checked by stylus scanning, showing a relatively high roughness (Figure AA6).

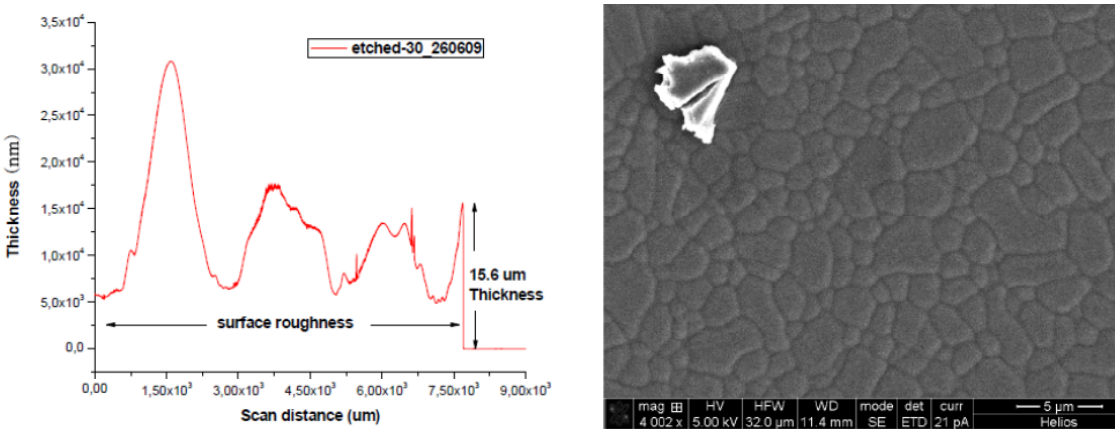

Figure AA6 a nanoporous 1,2-PB sample prepared by glass tube drawing on a teflon coated plate: (left) a surface roughness profile obtained by stylus scanning (Dektak 8); (right) a SEM image of top view surface.

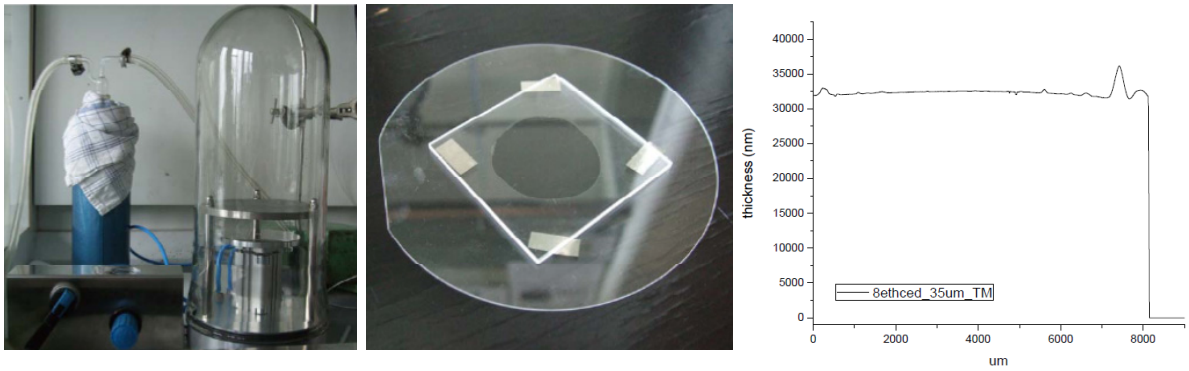

Figure AA7 A homemade pneumatic driven compressing set up (left); a sandwiched sample showing the cast polymer between two glass plates (mid); a surface roughness profile of an etched sample obtained from the sandwich method (right).

Sandwich

To better control the thickness and get a smooth surface, we finally used so-called sandwich method as described in chapter 3.2. A homemade pneumatic-driven compressing set up was used to squeeze the cast polymers to a flat sheet as shown in Figure AA7.

It is no problem to detach the cross-linked films from the FDTS-coated plate however it is rather difficult to remove it from glass plate (see chapter 3.2). All the cross-linked films were still packed in filter paper during the etching step.

The sandwich method provides a smooth surface with a well-defined surface structure (Fig. AA7). However there is still a lot of trouble in practice. We certainly need a flexible membrane with a sufficient mechanical strength. Cracks should be avoided during the membrane fabrication and operation. Fabrication methods can be diverse; however they will never sort out the problem which is caused by material itself. In order to thoroughly solve the problem, there may some opportunities in polymer synthesis, cross-linking step and etching steps which can be taken to improve the mechanical integrity of the membranes as described in chapter 9.

Appendix B Etching Process

In order to optimize the etching formulations, TBAF concentration $[TBAF]_0$, molar ratio of TBAF and $-\overset{|}{\underset{|}{\text{Si}}}-\text{O}-$ (m_{TBAF}/m_{Si-O}), and etching time t were varied between samples as listed in Table AB1. The maximum amount of PDMS is determined by mass fraction of PDMS in the block copolymer precursor, that is, 0.41 as shown in chapter 3.2, Table 3.1. The dry mass of each sample was compared before and after TBAF etching to give an indication of etching efficiency. The last column in Table AB1 shows the amount of etched PDMS (Δm_{PDMS}) normalized by the original mass of the sample m_0. While the work was aimed to develop a proper etching recipe, more importantly, we attempted to produce a series of nanoporous membranes with different intrinsic porosity by controlling the etching conditions. Therefore, after the preliminary work as presented in Table AB1, we kept $[TBAF]_0$ (= 0.005 M) and m_{TBAF}/m_{Si-O} (= 1) constant, and investigated the dependence of etching efficiency on time.

Table AB1 A preliminary study of etching solutions for the non-skin samples with 20 ± 5 μm thickness.

Sample	m_0 (mg)	$[TBAF]_0$ (M)	m_{TBAF}/m_{Si-O} (mol/mol)	t (min)	$\Delta m_{PDMS}/m_0$ (g/g)
BD36-X-1	24.3	0.010	1	20	0.35
BD36-X-2	22.6	0.005	1	20	0.32
BD36-X-3	21.1	0.0025	1	20	0.05
BD36-X-4	23.8	0.0010	1	20	0.04
BD36-X-5	18.6	0.005	1/2	120	0.42
BD36-X-6	18.3	0.005	1/3	120	0.41
BD36-X-7	21.9	0.005	1/4	120	0.41
BD36-X-8	22.1	0.005	1/5	120	0.32

In order to better interpret the etching results, here we first review the knowledge of reaction kinetics. For a generic reaction xA + yB → C with no intermediate steps in its reaction mechanism (that is, an elementary reaction), the rate is given by

$$rate = k(T)[A]^m[B]^n \qquad \text{(AB-1)}$$

where [A] and [B] express the concentration of the species A and B, respectively (usually in moles per liter); *m* and *n* are not the respective stoichiometric coefficients of the balanced equation; they must be determined experimentally. *k* is the rate constant of the reaction. The value of this coefficient *k* depends on conditions such as temperature, ionic strength, and surface area of the adsorbent or light irradiation. In our case, the species A and B are TBAF and the repeating unit of PDMS, $-\overset{|}{\underset{|}{\text{Si}}}-\text{O}-$. The reaction mechanism in detail was reported in Ref 2. However, the reaction process is complex and, m and n are unknown. Unlike the direct collision of two species dissolved in a liquid, in our case it is a contact between a dense block copolymer film and TBAF solution. Therefore, the apparent reaction rate is a result of (1) permeation of TBAF solution in the block polymer bulk, including the diffusivity *D* and solubility *S* of TBAF in the bulk; (2) etching reaction; (3) diffusion of the etching solution in the newly formed empty space during the etching process, as PDMS is partially cleaved and diffuses out. It is interesting to find out which action is the dominant step in determining the etching kinetics. The point (3) could be eliminated first since the liquid diffusion in an empty space is definitely faster than in a dense volume. So we will focus on a comparison between point 1 and point 2. If the reaction rate is the control step then a linear relationship of $[-\overset{|}{\underset{|}{\text{Si}}}-\text{O}-]$ *vs*. *t* (for zero reaction order) or $\frac{1}{[-\overset{|}{\underset{|}{\text{Si}}}-\text{O}-]^{n-1}}$ *vs*. *t* (for n-th order reaction) would be expected. If the permeation is the control step, then $[-\overset{|}{\underset{|}{\text{Si}}}-\text{O}-]$ *vs*. $t^{1/2}$ would occur as a consequent. As we know, the extension of the diffusion zone scales as $(Dt)^{1/2}$ with time. Hence the concentration gradient is approximately proportional to $[TBAF]_0/(Dt)^{1/2}$. Within certain time limits, the permeation represents a quasi-steady process, that is, the amount of reacted TBAF per unit time is equal to that brought to the solution/polymer interface by permeation.

Figures AB1 (a) and AB1 (b) show the amount of PDMS etched (Δm_{PDMS}) per unit surface area (*A*) of the precursor film as function of the etching time. We found a linear dependence happened to both skin samples and non-skin samples with different thickness. Each sample reached a plateau where all the PDMS have been reacted. For a better vision, we put all the data

from Figs. AB1 (a) and AB1 (b) in Fig. AB1 (c) and displayed in an expression of $\Delta m_{PDMS} / m_0$ *vs. t/l* where a transformation has been done as follows.

$$\frac{\Delta m_{PDMS}}{A} = rate \cdot \Delta t \qquad \text{(AB3-2)}$$

$$\Rightarrow \quad \frac{\Delta m_{PDMS}}{m_0 / (\rho_{PDMS} \cdot l)} = rate \cdot \Delta t \quad (\rho_{PDMS} \sim 1g / cm^3)$$

$$\Rightarrow \frac{\Delta m_{PDMS}}{m_0} = rate \cdot (\Delta t / l) \qquad \text{(AB3-3)}$$

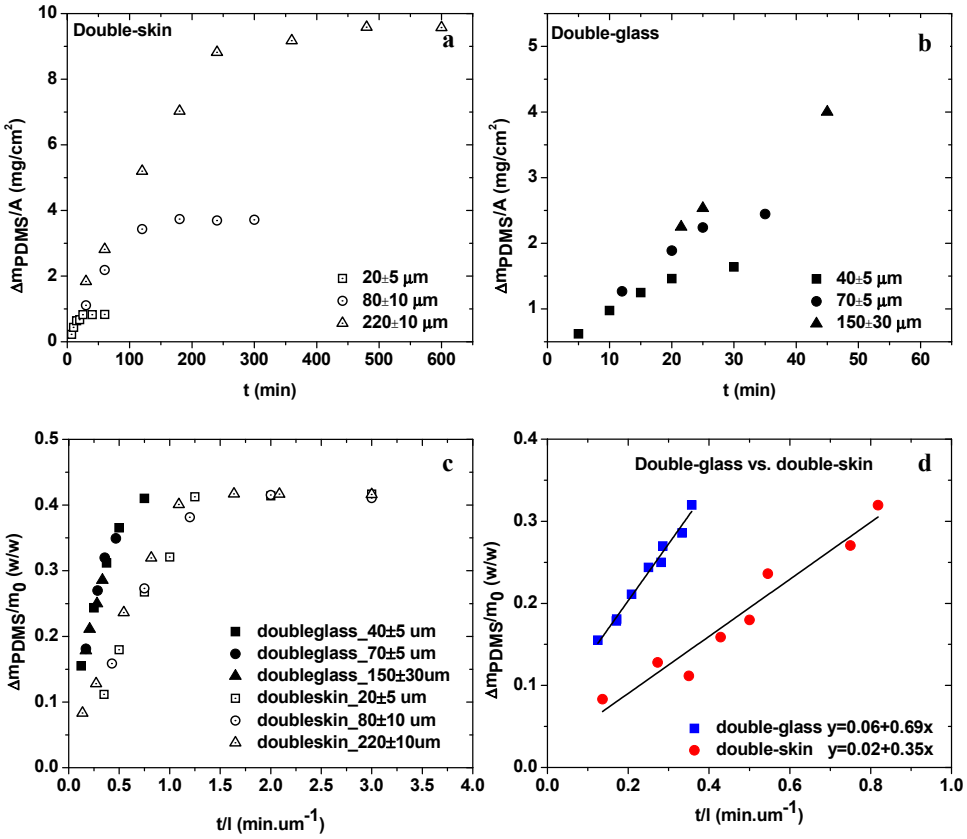

Figure AB 1 Etching degree as a function of time. (a) The etched amount of PDMS per unit surface area of double-skin sample vs. time; (b) The etched amount of PDMS per unit surface area of double-glass sample vs. time; (c) The data shown in Figs (a) and (b) were re-expressed by the etched amount of PDMS relative to the original mass m_0 of the precursor as function of time normalized by sample thickness *l*. (d) Linear fittings of the data presented in the linear region of Fig.(c).

Figure AB1 (d) shows linear fittings to the data at the linear region of Fig. AB1 (c). Two constant rate values were obtained for non-skin and skin samples. It seems that the reaction is a control step in the etching process and the reaction rate is the zero order and independent of reactant concentration. Figures AB2 (a) and AB2 (B) present plots of $\Delta m_e / A$ *vs.* $t^{1/2}$ for a comparison with Figure AB2. We could not observe a linear relationship $\Delta m_e / A$ *vs.* $t^{1/2}$. This confirms the permeation is not the control step for the etching process. However, the difference between the two profiles (Fig AB1 (c)) for the non-skin samples and double-skin samples hints to somewhat diffusion control. This indicates a higher resistance to TBAF diffusion caused by the existence of a dense skin layer. No certain conclusions can be given at the present study.

From now on, we used a formulation of $[TBAF]_0$ =0.005 M, m_{TBAF} / m_{Si-O} =1 (mol/mol) and the sufficient *t* is calculated from the linear fitting shown in Fig. AB (d). For most of the thesis work, a complete etching was performed to obtain samples with maximum porosity, while a batch of samples with different porosity was prepared for investigating the effect of intrinsic porosity on membrane diffusion performance as presented in Table AB2. Unfortunately, no clear dependence was observed between the effective diffusion coefficient and etching degree.

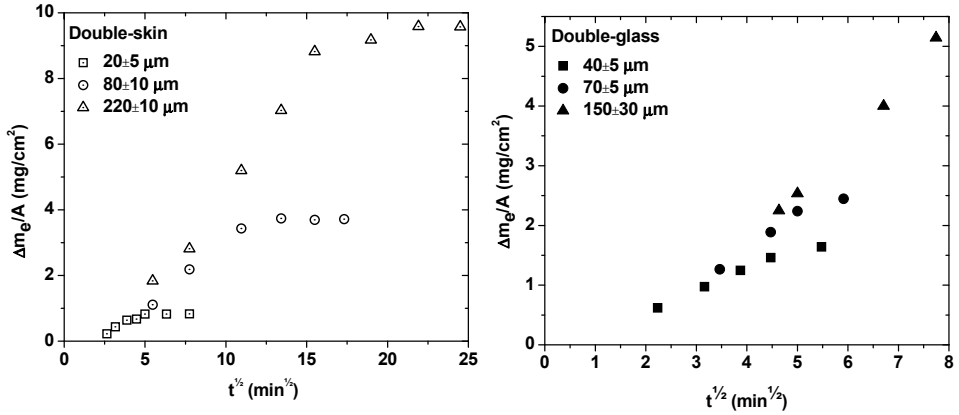

Figure AB2 The etched amount of PDMS per unit surface area as a function of the square root of time. (a) Double-skin samples; (b) Double-glass samples.

Table AB2 Effective diffusion coefficient of glucose through the double-skin and non-skin membranes with varying porosity.

Sample Double-skin	**Thickness (um)**	**Porosity (w/w)**	$D_{eff\_glucose}$ **(cm^2/s)**
6 samples	23	33%	2.83E-08 ± 1.27E-08
4 samples	20	31%	1.70E-08 ± 1.11E-08
2 samples	20	30%	3.51E-08 ± 6.79E-09
3 samples	30	28%	1N/A; 6.75E-09 ± 9.76E-10
3 samples	25	26%	3.87E-08 ± 3.36E-08
1 sample	20	22%	4.89E-09
3 samples	20	20%	N/A
3 samples	20	16%	2NA; 5.34 E-09
Sample Non-skin	**Thickness (um)**	**Porosity (w/w)**	D_{eff} **(cm^2/s)**
2 samples	45	38%	7.57E-07
2 samples	33	38%	7.02E-07; 1 N/A
2 samples	30	35%	1.13E-06; 1 N/A
2 samples	30	33%	N/A
2 samples	25	33%	7.54E-07±3.6E-07
2 samples	46	31%	N/A
4 samples	30	30%	N/A
2 samples	45	24%	N/A
2 samples	35	16%	N/A

Appendix C DSC Results

Water states in nanoporous membranes were checked by DSC measurements. Both hydrophilic membrane (HM) and hydrophobic membrane (M) were measured. We first give a short review on experimental conditions and procedures.

Differential Scanning Calorimetry (DSC) measurements were carried out using a TA instrument DSC 1000 equipped with a cooling unit. A sample was cut into small (2 mm in diameter) pieces. The original hydrophobic membrane was prewetted with ethanol and replaced with water; the hydrophilic membrane was only prewetted with water. Thereafter the pieces were placed in an aluminum pan and extra water was added to the pan. The pan was sealed and the excess water on the outside of the pan was wiped with a tissue. The experiment started by heating from -73 ºC to 25 ºC at a rate of 2.5 ºC /min and a number of heating-cooling cycles were conducted. Nitrogen gas was used as the carrier gas with a flow rate of 50 ml/min.

Procedures

1. Weigh an empty aluminum pan and lid; the aluminum pans and lids were pretreated with boiling water for 1 h to eliminate the reaction of water with aluminum surface during DSC.
2. Cut a membrane (pre-vacuumed) into tiny pieces (3 mm in diameter); measure the dry mass of samples to be tested;
3. For HM samples, add droplets of water (the amount of water should be larger the water content of the samples being tested) into the pan; wait for a few seconds until water sorbs into the samples. Add more water before sealing. For M samples, add droplets of ethanol to prewet the samples for 5 min and replace with water before sealing.
4. Seal the pan, use a tissue to dry the excess of water outside of the pan and measure the total mass (pan+lid+sample+water).
5. After DSC, measure the total mass again.
6. Prick a few holes on the lid and dry the samples in the vacuum oven at room temperature overnight. Weigh the total mass (pan+lid+sample) after drying.

The DSC data were summarized in the Figure AC1 for a comparison. Figure AC1 (a) shows the DSC data of the blank sample, i.e. M+W without pre-wetting. No water infiltration to the hydrophobic sample; bulk water outside the membrane shows phase transition temperature at around 0 ºC. In Figure AC1 (b) solid line shows the hydrophobic membrane with ethanol prewetting and there after replacing with water before DSC measurement as described above.

In the case, we expect that water infiltration to M. Besides the free water in M showing the same phase transition temperature as bulk water (0 ºC), we can also observe an additional peak around -12 ºC. This can possibly arise from the mixture of water with the remaining ethanol inside the pore. At the start, the infiltration of water into the ethanol prefilled nanopores is based on concentration potential. At equilibrium, most of ethanol will be washed out; however, some ethanol molecules would remain on pore wall to reduce the surface tension of the polymer thus keeping water inside. A precise ratio of ethanol and water inside the pores is difficult to estimate. However, it might be also argued that this is due to weak interaction between ethanol or water molecules and pore wall. It is also possibly due to capillary force that induced a phase transition shift. In order to get a qualitative indication, we run DSC for a 1:5 (v/v) mixture of ethanol and water. A phase transition occurred at around - 9 ºC for such liquid mixture. We further checked a phase diagram for solid-liquid equilibrium of the mixture of ethanol and water as shown in Figure AC2[3]. Our experimental observation is well consistent with the literature value in Fig. AC2. In addition, we also found a phase transition around -12 ºC roughly corresponds to a 9:25 (v/v) ethanol/water mixture.

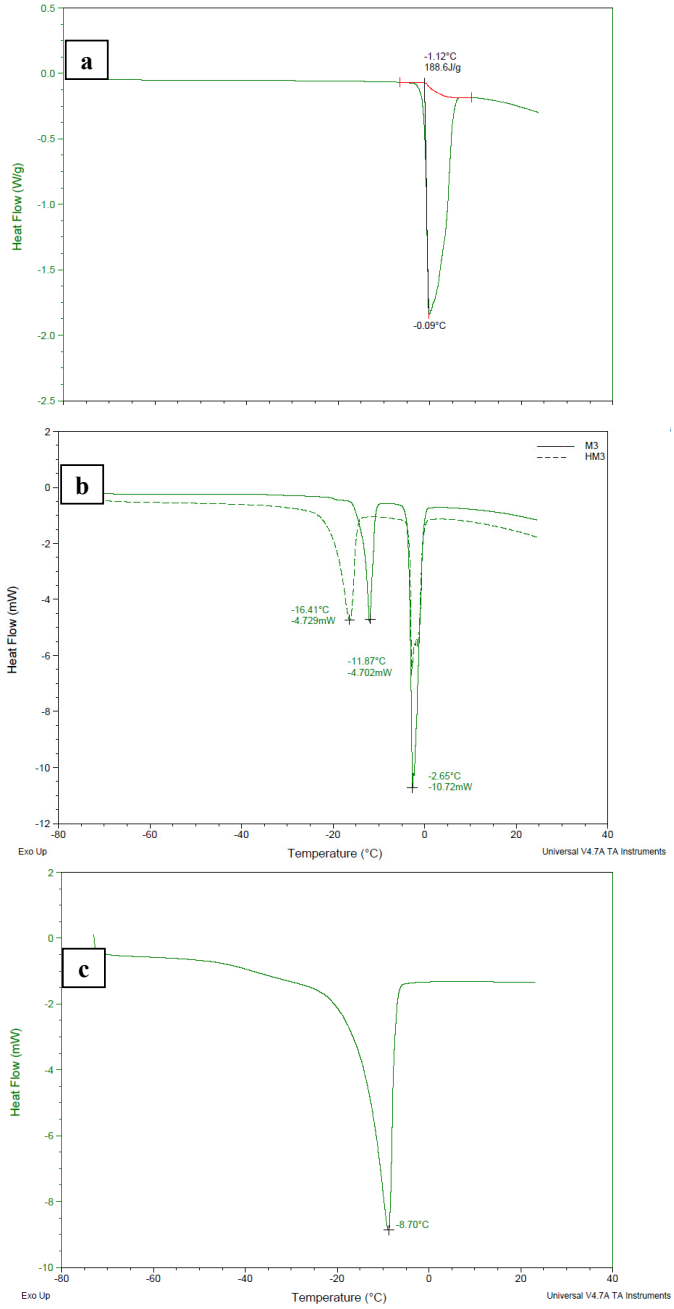

Figure AC1. DSC data of (a) a hydrophobic membrane in water without prewetting; (b) a hydrophobic membrane in water with ethanol prewetting and water replacement (solid line) and a hydrophilic membrane in water (dash line); (c) a 1:5 (v/v) mixture of ethanol and water.

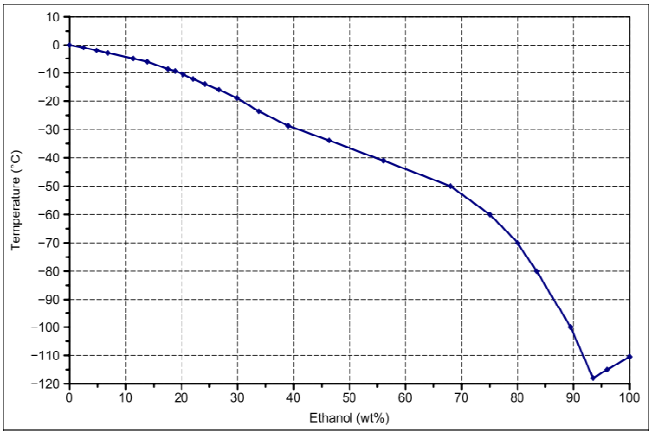

Figure AC2 A phase diagram for solid-liquid equilibrium of the mixture of ethanol and water.

Appendix D Diffusion of PEGs across Nanoporous 1,2-PB Membranes

Diffusion tests of single PEG solutions (1g/L) with different PEG molecular weight (1 kg/mol, 4 kg/mol and 8 kg/mol) were conducted for the original hydrophobic membranes (M) and the sulfonated hydrophilic membranes (HM) with 25 μm in thickness. The hydrophobic membranes were prewet with ethanol for half an hour before any measurements. Figure AD1 (a) shows the PEG concentration on the permeate side as function of time. For the hydrophobic membrane, PEG 1K permeation is much faster than PEG 4K and PEG 8K. The effective diffusion coefficient D_{eff} of PEG 1K was calculated from eq. 6-16 (chapter 6) and the lag equation 6-17 (chapter 6) was used to calculate D_{eff} for PEG 4K and PEG 8K. Therefore we obtained D_{eff_1k} = 8.48 e-08 cm^2/s; D_{eff_4k} = 1.28e-08 cm^2/s; D_{eff_8k} = 1.21e-10 cm^2/s. For the hydrophilic membranes, within the measurement time, only the permeation of PEG 1K could be detected; little or no permeation for PEG 4K and PEG 8K. This can be explained by the fact that the reduced effective pore size of HM gave rise to higher size exclusion. A high selectivity was thus shifted to lower molecular weight range, between PEG 1K and PEG 4K. This observation well supports the rejection profile obtained in PEG ultrafiltration of HM+W as shown in Figure 7.9 (chapter 7). For PEG 1K, both M and HM show very similar permeation rate.

As shown in Figure AD1 (b), the hindrance diffusivity calculated from experimental data based on eq. 6-15 (chapter 6) was compared with the theoretic prediction by Bungay & Brenner Model with the consideration of size effect alone for rigid globular molecules. PEG molecules exhibits the experimental values lower than the theoretic values (Fig AD (b)). There are two possible reasons: (1) the adsorption of PEG molecules onto the pore wall as confirmed in Figure xx (chapter 7); (2) The flexible linear molecules have random variations in molecular shape in free water without boundary. The limited configurations in a small pore are entropicly unfavorable for PEG molecules. If without additional energy applied, e.g. pressure-driven flow,

the entropic and hydrodynamic considerations for neutral, random coils lead to values of hindrance diffusivity lower than those for solid spheres.[4]

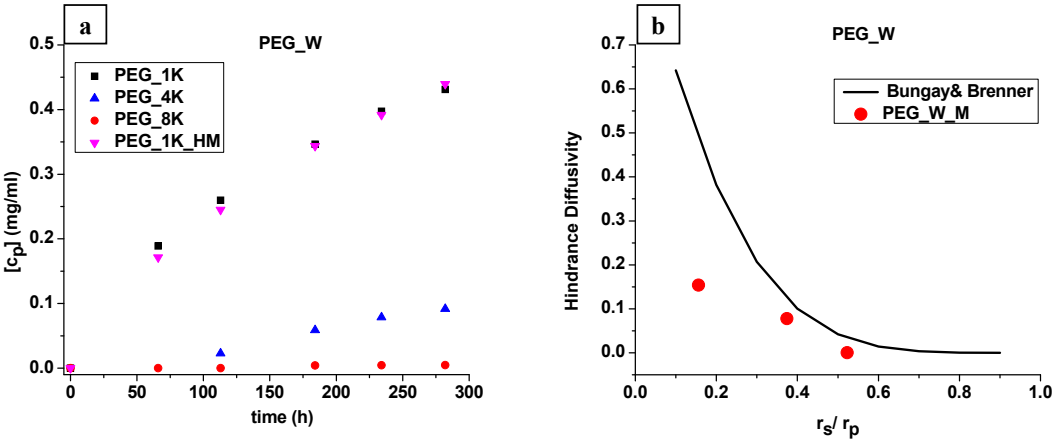

Figure AD1 (a) PEG concentration in permeate side as function of time for the M+W and HM+W systems; (b) Comparison of hindrance diffusivity between experimental data calculated from M+W system in Fig. (a) and theoretic prediction by Bungay & Brenner model with consideration of size effect alone for rigid globular molecules.

References

[1] Poulard, C. and Damman, P. Control of spreading and drying of a polymer solution from Marangoni flows. *EPL* **2007**, *80*, 64001.

[2] Schulte, L.; Grydgaard, A.; Jakobsen, M. R.; Szewczykowski, P. P.; Guo, F.; Vigild, M. E.; Berg, R. H.; Ndoni, S. Nanoporous Materials from Stable and Metastable Structures of 1,2-PB-*b*-PDMS Block Copolymers. *Polymer* **2011,** *52*, 422.

[3] http://en.wikipedia.org/wiki/File:Phase_diagram_ethanol_water_s_l_en.svg

[4] Higuchi, A. and Iijima, T. DSC investigation of the states of water in polyvinyl-alcohol membranes, *Polymer* **1985**, *26*, 1207.

List of Abbreviations

AAO	Anodized aluminum oxide
AFM	Atomic force microscopy
ATR	Attenuated total reflectance
BCC	Body centered cubic spherical structure
BCP	Block copolymer
CA	Contact angle measurements
Cal 1	Calibration solution 1
CLSM	Confocal Laser scanning Microscopy
CMC	Critical micelles concentration
D	Dialysis
DCP	Dicumyl peroxide
DI	Deionized
DMPA	2,2-Dimethoxy-2-phenylacetophenone
DMF	N,N-dimethylmethanamide
ds	Double-skin membrane
DSC	Differential Scanning Calorimetry
EW	A 80:20 (v/v) mixture of ethanol and water
EM	Enzyme layer
FDTS	$Cl_3Si(CH_2)_2(CF_2)_7CF_3$
FTIR	Fourier transform infrared spectroscopy
GYR	Bicontinuous gyroid structure
GOx	Glucose oxidase enzyme
HEX	Hexagonally packed cylindrical structure
HM	Hydrophilized membranes
HPL	Hexagonally perforated lamellae structure
IM	Inner membrane
LAM	Lamellar structure
LbL	Layer-by-layer
L-W	Lucas-Washburn equation
M	Originally hydrophobic membranes
MESNA	Sodium 2-sulfanylethanesulfonate
MW	Molecular weight
NMR	Nuclear magnetic resonance
NPM_E	sensor mounted with the nanoporous 1,2-PB membrane
NPM_UV_E	a sensor mounted with the UV-photooxidized nanoporous 1,2-PB membrane
NPMs	Nanoporous 1,2-PB membranes
ns	Non-skin membrane
ODT	Order-to-disorder transition
OM	Outer membrane
1,2-PB-*b*-PDMS	1,2-polybutadiene-b-polydimethylsiloxane

PCEMA	Poly(2-cinnamoylethyl methacrylate)
PB	Polybutadiene
PDI	Polydispersity index
PDMS	Polydimethylsiloxane
PEG	Polyethylene glycol
PET	Polyethylene terephthalate
PI	Polyisoprene
PMMA	poly(methyl methacrylate)
PPQ	Poly (phenylquinoxaline)
PPS	Poly(4-vinylphenyl-dimethyl-2-propoxysilane)
PS	Polystyrene
P*t*BA	Poly(*tert*-butyl acrylate)
PVC	Polyvinyl chloride
QC	Quality control solutions
Ref_E	Reference sensor
SAXS	Small angle X-ray scattering
SDS	Sodium dodecyl sulfate
SEM	Scanning electron microscopy
SEC	Size exclusion chromatography
ss	Single-skin membrane
Std_E	Commercial glucose sensor
TBAF	Tetrabutylamonium fluoride
TEM	Transmission electron microscopy
THF	Tetrahydrofuran
UF	Ultrafiltration
upd	Updating
W	Water
TM	Transmission mode
XPS	X-ray photoelectron spectroscopy

List of Symbols

A or A_0	surface area
A_{spec}	specific interior surface area
c_s	radially average concentration in a pore
c_b	concentration in bulk solution
c_f	concentration in the feed solution
c_p	concentration in the permeate solution
c_m	concentration near the membrane surface
d_p	pore diameter
D_{eff}	effective diffusion coefficient
D_∞	diffusion coefficient of solutes in free solution
D_{Kn}	knudsen diffusion coefficient
ΔF_i	driving force
G	the enhanced drag
ΔG_{ads}	Gibbs free energy of adsorption
$f_{A\ orB}$	surface fraction of component A or B
J_w	water flux across a fresh membrane
J_v	filtration flux
J_r	relative flux reduction
J_{wa}	water flux across a membrane after static adsorption
J_{wf}	water flux across a membrane after pressure-forced adsorption
J_{rv}	relative filtrate flux reduction during ultrafiltration
J_{ra}	relative flux reduction after static adsorption
J_{rf}	relative flux reduction after pressure-forced adsorption
J_{ro}	osmotic pressure-induced flux reduction
k	mass transfer coefficient
k_B	Boltzmann constant
K	hydrodynamic coefficients
K_C	hindrance factors for convective transport
K_D	hindrance factors for diffusive transport
K_s , K_t	hydrodynamic functions
K_c	hindrance factor for convection transport
K_d	hindrance factor for diffusion transport
K_{eq}	the Langmuir equilibrium constant
l	membrane thickness
l_{SDS}	thickness of the adsorbed SDS layer
L_P	hydraulic permeability
$<M_n>$	number-average molecular weight
$<M_w>$	weight-average molecular weight
m_{dry}	dry mass
m_{wet}	wet mass

m_o	original dry mass of membrane
m_a	dry mass of membrane after static adsorption
Δm	dry mass difference before and after static adsorption relative the original dry mass
N_A	Avogadro constant
N_s	solute flux across membrane
Pe	peclet number
ΔP	the applied pressure difference across the membrane
r_p *or* R_h	pore radius
R	gas constant
R_m	membrane resistance
R_a	static adsorption resistance
R_f	fouling resistance
R'_a	relative static adsorption resistance
R'_f	relative fouling resistance
r_s or R_h	hydrodynamic radius
Rej_{obs}	observed rejection coefficient
Rej_{actual}	actual rejection coefficient
T	temperature
S_∞	asymptotic value of the sieving coefficient at large Peclet number
U	solute molecule velocity
$V_{1or\ 2}$	volume
v	the radially average velocity in a pore
w_{PDMS}	mass fraction of PDMS
v_{spec}	specific volume of nanoporous membrane

Greek Symbols

α	selectivity or separation factor
δ_m	thickness of boundary layer
δ	pore constrictivity
ε	membrane porosity
η	gas viscosity
μ	liquid viscosity
θ	contact angle
λ	the ratio of hydrodynamic radius of solute to pore radius
$\Delta\pi$	osmotic pressure
π'	relative osmotic pressure resistance
σ	reflection coefficient
ρ	density
τ	tortuosity
τ_0, τ_1, τ_2	characteristic time
ϕ	equilibrium partition coefficient
γ	surface tension
γ_{ls}, γ_{lv}, γ_{sv}	interface tension between solid/liquid, liquid/vapor or solid/vapor

Γ	surface adsorption capacity

The Danish Polymer Centre
Department of Chemical and Biochemical Engineering
Technical University of Denmark
Søltofts Plads
DK-2800 Kgs. Lyngby
Denmark

Phone: +45 4525 2800
Web: www.dpc.kt.dtu.dk

ISBN: 978-87-92481-61-0